

Rheinische Friedrich-Wilhelms Universität Bonn
Institut für Physikalische und Theoretische Chemie

**Fuel Cells, Metal/Air Batteries:
characterization of dual thin-layer flow through cell and
determination of solubility and diffusion coefficient of
oxygen in aqueous and non-aqueous electrolytes**

Dissertation

zur

Erlangung des Doktorgrades (Dr. rer. nat.)

der

Mathematisch-Naturwissenschaftlichen Fakultät

der

Rheinischen Friedrich-Wilhelms-Universität Bonn

vorgelegt von

Mehdi Khodayari

aus

Teheran - Iran

Bonn, 2015

Angefertigt mit Genehmigung der Mathematisch-Naturwissenschaftlichen Fakultät der
Rheinischen Friedrich-Wilhelms-Universität Bonn

Promotionskommission:

Erstgutachter (Betreuer):

Prof. Dr. Helmut Baltruschat

Zweitgutachter:

Prof. Dr. Thomas Bredow

Fachnahes Mitglied:

Prof. Dr. Werner Mader

Fachangrenzendes Mitglied:

Prof. Dr. Karl Maier

Erscheinungsjahr:

2015

Tag der mündlichen Prüfung:

03.07.2015

Diese Arbeit wurde als Dissertation im Fachbereich Physikalische Chemie an der Mathematisch-Naturwissenschaftlichen Fakultät der Rheinischen Friedrich Wilhelms-Universität in Bonn, zur Erlangung des Doktorgrades, im Arbeitskreis von Herrn Prof. Dr. H. Baltruschat, angefertigt.

Der Autor versichert, dass die vorliegende Arbeit eigenständig verfasst und keine weiteren Hilfsmittel als die angegebenen verwendet zu haben. Alle verwendete Literatur und Informationsquellen sowie weitere Hilfsmittel sind in den Zitaten und Fußnoten gekennzeichnet.

Bonn, 03.05.2015

Mehdi Khodayari

To my country, my parents and my family

The fuel in the earth will be exhausted in a thousand or more years, and its mineral wealth,
but man will find substitutes for these in the winds, the waves, the sun's heat, and so forth.

— John Burroughs

Under the Apple-Trees (1916), 308

Contents

1	Introduction	19
1.1	Motivation	20
1.2	Basics.....	22
1.2.1	Fuel Cells.....	22
1.2.2	Metal-air batteries	27
1.3	Differential Electrochemical Mass Spectrometry (DEMS).....	29
1.4	Steady-state mass transfer	33
2	Experimental	35
2.1	Electrochemical and mass spectrometric methods	36
2.1.1	Cyclic Voltammetry (CV).....	36
2.1.2	Differential Electrochemical Mass Spectrometry (DEMS)	40
2.2	Vacuum system.....	42
2.3	Calibration of system.....	43
2.4	Chemicals	46
2.5	Electrodes	48
2.6	Data acquisition	49
3	Characterization of dual thin-layer flow through cell	51
3.1	Theoretical aspects	52
3.1.1	Collection efficiency	52
3.1.2	Transfer efficiency	54
3.1.3	Shielding factor	56

3.2	Hydroquinone / Quinone	58
3.3	Fe ²⁺ / Fe ³⁺	61
3.4	Dissolved hydrogen measurements	64
3.5	Correlation of limiting current and flow rate.....	68
3.6	Correlation of collection efficiency and flow rate.....	79
3.7	Correlation of transfer efficiency and flow rate	81
3.8	Correlation of shielding factor and flow rate.....	86
3.9	Effect of thin layer thickness	88
3.10	¹³ CO bulk oxidation.....	93
3.11	Mass spectrometric characterization	100
3.12	Literature review.....	104
3.13	Conclusion	107
4	Oxygen solubility and diffusion coefficient.....	109
4.1	Theoretical aspects	112
4.2	Flow rate dependence of the ionic current.....	114
4.3	O ₂ solubility and diffusion coefficient in aqueous and non-aqueous electrolytes...	122
4.4	Conclusion	129
5	Summary / Conclusion	131

Notation

a	Diameter of the inlet capillary
A_{geom}	Geometric surface area
A_{real}	Real surface area
b	Channel height of dual thin-layer flow through cell
c	Concentration
C^*	Concentration in the bulk of the solution
C_{dl}	Double layer capacitance
D	Diffusion coefficient
E	Potential
F	Faraday constant, 96500 C mol^{-1}
f_F	Collection efficiency of the electrochemical compartment of the dual thin layer cell
f_i	Collection efficiency of the detection compartment of the dual thin layer cell
g	geometric factor
I_F	Faradaic current
I_x	Ionic current of species (x)
j	Current density
K	Calibration constant of species (x)
K°	Calibration constant of DEMS
K_H	Henry constant
k_p	Rate constant for the transport through the membrane capillaries
m	Number of reacting species in the second working electrode
N	Transfer efficiency
n	Number of reacting species in the first working electrode
Q_F	Faradaic charge
Q_H	Charge of H_{ad} at Pt surface
Q_i	Ionic charge
R	Universal gas constant, $8.314 \text{ Jk}^{-1}\text{mol}^{-1}$
R	Roughness factor
S	Shielding factor
t	Time
u	Electrolyte flow rate
v	Sweep rate
X	Starting material (educt)

Y	Reaction product of the upper compartment of dual thin-layer flow through cell
z	Number of electrons in reaction
Z	Reaction product of the lower compartment of dual thin-layer flow through cell
ν	Kinematic viscosity

Abbreviation

AC	Alternating current
AFC	Alkaline fuel cell
CE	Counter electrode
CV	Cyclic Voltammogram
DAFC	Direct alcohol fuel cell
DC	Direct current
DEMS	Differential Electrochemical Mass Spectrometry
DMFC	Direct Methanol Fuel Cell
DMFC	Direct methanol fuel cell
EMS	Electrochemical Mass Spectroscopy
GC	Glassy Carbon
LEED	Low Energy Electron Diffraction
LEIS	Low Energy Ion Spectroscopy
MCFC	Molten carbonate fuel cell
MSCV	Mass Spectrometrical Cyclic Voltammogram
MSCV	Mass spectrometric cyclic voltammogram
PAFC	Phosphoric acid fuel cell
PEMFC	Proton Exchange Membrane Fuel Cell
ppm	Part per million
Pt(Poly)	Polycrystalline platinum
PTFE	Polytetrafluorethylen (Teflon)
REF	Reference electrode
RHE	Reversible Hydrogen Electrode
SE	Supporting electrolyte
SEM	Secondary Electron Multiplier
SOFC	Solid oxide fuel cell
STM	Scanning Tunneling Microscopy
UHV	Ultra-High Vacuum
WE	Working electrode
XPS	X-ray Photoelectron Spectroscopy

Chapter 1

1 Introduction

1.1 Motivation

Until now the energy demand is substantially met by fossil fuels such as natural gas, oil and coal. The available resources are finite. Forecasts assume that at constant consumption the availability of oil reserves in 2050 will decrease rapidly [1]. The amounts of energy required must be replaced by alternative techniques (e.g. solar or wind energy, fuel cells, metal/air batteries). In the combustion of fossil fuels, there are various environmental pollutant emissions such as nitrogen oxides, sulfur dioxide and carbon monoxide. Although carbon dioxide (CO₂) as one of the main emissions is not an environmental poison, but it is a greenhouse gas that contributes to global warming. With the adoption of the Kyoto Protocol on 11th of December 1997, an international agreement to reduce emissions was decided [2]. In order to achieve this ambitious goal, it is necessary applying alternatives to develop the burning of fossil fuels [3]. The fossil or alternatively recovered energy can be saved by obtained electrolytic hydrogen, which can be later used for energy in fuel cells. Fuel cells, including the methanol fuel cell (DMFC) can compete with batteries and generators for mobile use. They provide services from a few watts for the power supply of mobile phones or laptops to a few kilowatts to supply of an entire household.

Since 2003, the first small series of various automobile manufacturers are developed, in which the energy is produced with fuel cells. Nevertheless, research and development potential still exists [4].

One of the main challenges in the metal-air batteries is the selection of a suitable electrolyte that is characterized with high oxygen solubility, low viscosity, liquid state and low vapour pressure in a wide temperature range and stable in a wide potential window.

In this work, we present a new technique to determine the solubility and diffusivity of oxygen in aqueous and non-aqueous electrolytes by on-line differential electrochemical mass spectrometry (DEMS), using a dual thin-layer flow through cell.

Two methods are applied to characterize the dual thin-layer flow through cell. The first method considers the hydrodynamic electrochemical behavior of the cell which is composed of two working electrodes and can be considered as the analogue of a rotating ring-disk system. The hydrodynamic electrochemical characteristics such as correlation of the electrolyte flow rate with the faradaic current, transfer efficiency, shielding factor and collection efficiency are studied for Fe^{3+} , Hydroquinone and dissolved H_2 solutions.

The second method represents the mass spectrometric behavior of the cell for different gaseous and volatile substances. In this method the dual thin-layer flow through cell is connected to the mass spectrometer via a permeable Teflon membrane. The correlation of mass spectrometric current with solution flow rate is studied by this method.

1.2 Basics

1.2.1 Fuel Cells

1.2.1.1 History

Fuel cells are not new scientific discovery. The operating principle is based on the controlled electrochemical reaction of hydrogen with oxygen to form water by using the electric power given off. The principle of the fuel cell was discovered in 1838 by Christian Friedrich Schönbein in an electrolyte solution (probably sulfuric acid) lapped two platinum wires with hydrogen and oxygen, and found a voltage between the wires. Schönbein published these results in 1839 [5]. In the same year Sir William Grove wrote a note on the battery-based oxyhydrogen and applied these concepts in cooperation with Schönbein in several experiments [5].

Later on, the fuel cell technology could conquer niche places in high price applications such as energy systems of submarines and space shuttles [6].

Both Siemens and Varta built alkaline fuel cell converter stations in the late sixties for television stations in the power range of 25 to 100 W. But significant restrictions on the applicability of these fuel cells were the fact that only pure hydrogen as fuel and pure oxygen could be used as the oxidant. There were the high cost of used materials and manufacturing processes [6].

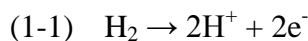
With the technical implementation of the core technology and an apparently adequate supply of fossil fuels, fuel cell research was reduced in 1970. However, after the energy crisis of 1973, this situation changed quickly. A response was the MOONLIGHT program in Japan. Herein, particularly the Phosphoric acid fuel cells (PAFC) and the molten carbonate fuel cell (MCFC) were promoted. Both the MCFC and SOFC (solid oxide fuel cell) are still regarded in Japan as a technology of the second generation that will follow the PAFC [7].

1.2.1.2 Relevant reactions in the fuel cells

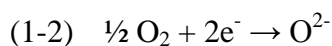
The conventional conversion of the chemical energy of a fuel into electricity is currently based on the application of heat engines. These machines operate on the principle of indirect energy conversion: it must first produce heat (steam generation), which is then converted into mechanical (turbine) and ultimately to electric energy (generator) [8].

The fuel cell is in competition with the usual thermo-mechanical energy conversion. The fuel cell is an electrochemical apparatus for the direct conversion of chemical energy of a fuel into electricity.

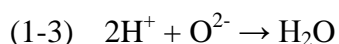
In the construction of a fuel cell, there are two electrodes and a gas-permeable, separating the gases, and ion-conductive electrolyte layer which is shown schematically in Figure 1-1. The supply of the reaction gases in each case are integrated into the electrodes. On the anode side, the fuel gas hydrogen is catalytically oxidized in accordance with:



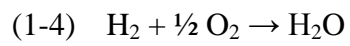
The resulting electrons pass through the external load circuit to the cathode where the oxidant oxygen is catalytically reduced according to:



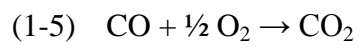
Depending on the electrolyte, the hydrogen protons wander from the anode to the cathode (PEFC, PAFC) or the anions in the opposite direction (AFC, MCFC, SOFC), where the reactants meet and lead to water:



The gross reaction then results in the following equation:



In addition to the use of pure hydrogen, the energetic utilization of carbon monoxide in the high temperature cells also reacts to carbon dioxide analogously to the reaction of hydrogen:



1.2.1.3 Structure of the fuel cell

Basically, the fuel cell consists of two electrodes, the anode and the cathode, and an electrolyte separating the two electrodes. The electrochemical process is basically in reverse order as the electrolysis. The fuel, hydrogen, is continuously supplied to the anode where it is decomposed in the presence of a catalyst into electrons and ions. At low temperatures, this can be protons in acidic electrolyte; and in alkaline electrolytes primarily hydroxyl ions. Ions are transported through the electrolyte to the cathode [9].

Due to the potential difference between Butane gas and oxygen electrode, the electrons flow through the external circuit (electrical load) to the cathode and perform electrical work. The ions and electrons combine at the cathode with the supplied oxygen, which is discharged as water vapor.

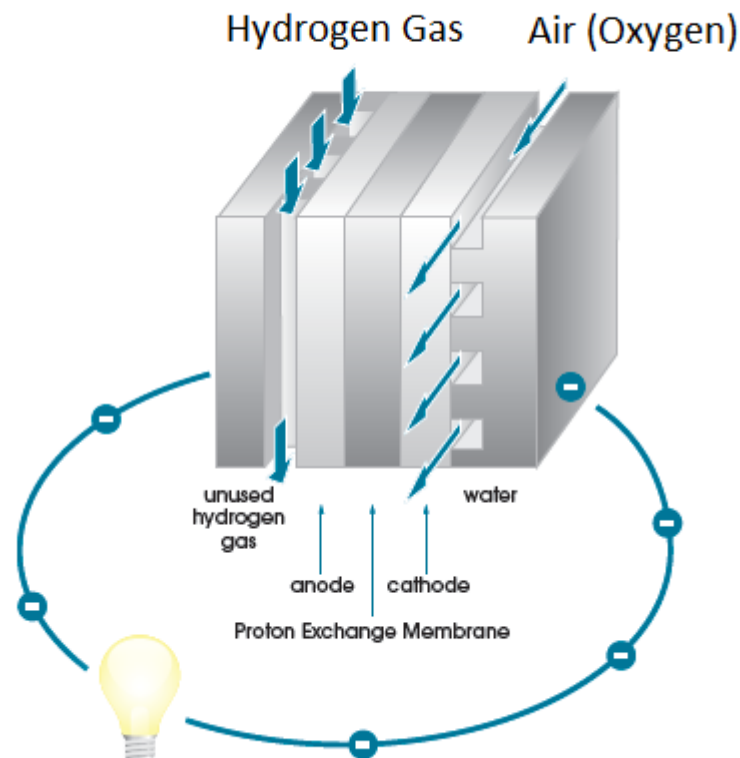


Figure 1-1 Diagram of a PEM Fuel Cell (source: <http://www.fuelcellsystems.co.uk>)

1.2.1.4 Fuel Cell Types

Different types of fuel cells are shown in Figure 1-2 as they are classified depending on the operating temperatures and the electrolyte. The distinction between operating temperatures leads to further definition of low temperature and high temperature fuel cells.

The developments of the PAFC, MCFC and SOFC aim to the stationary energy supply. The PEFC is designed primarily for mobile but also for stationary applications. The DMFC is designed to drive; but it also has a particularly high potential for small portable applications [10].

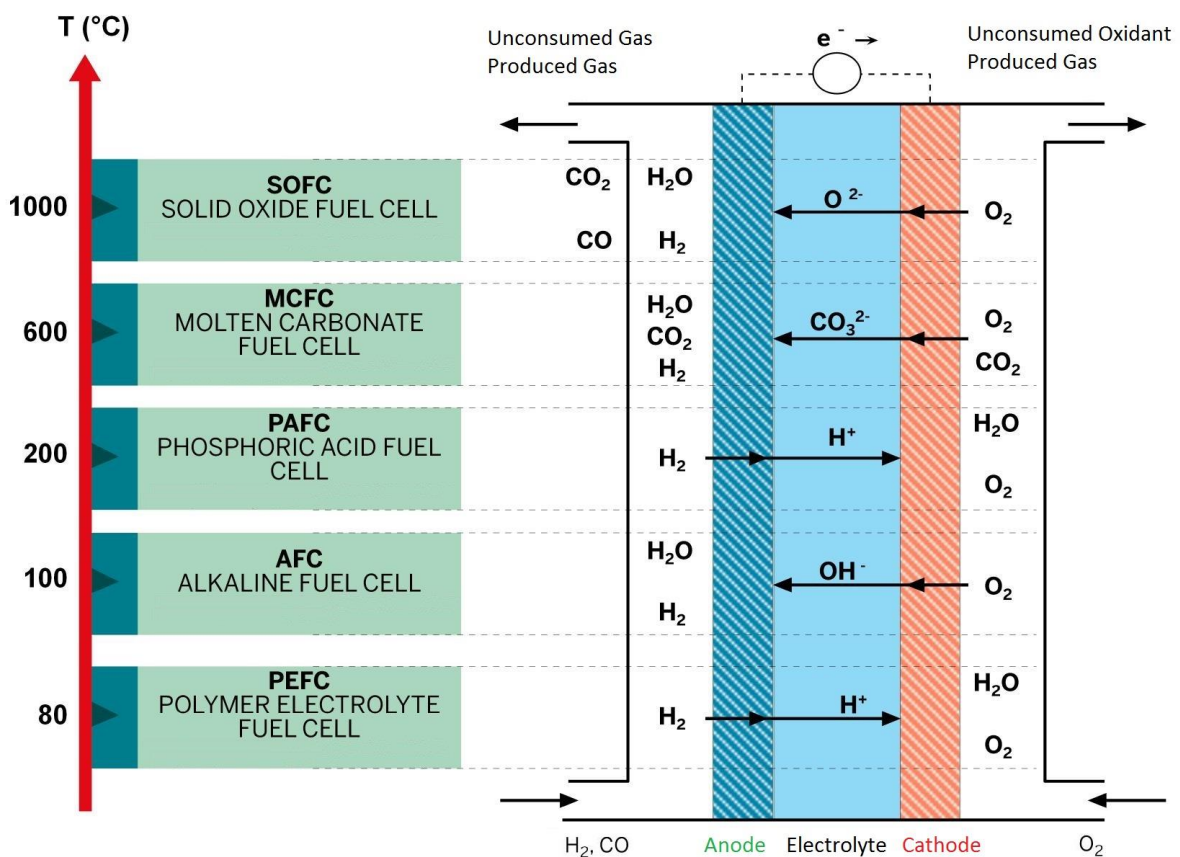


Figure 1-2 Different types of Fuel Cells, classified depending on the operating temperature and the electrolytes (source: EnergieAgentur.NRW; <http://www.energieagentur.nrw.de/>)

1.2.2 Metal-air batteries

The metal-air battery is functionally similar to the fuel cells due to consisting of an air cathode which is constantly utilizing air [11]. One of the most promising metal-air batteries and known as a future technology for high-performance batteries is lithium-air battery, which is still in development [12]. With such a metal-air batteries energy densities are obtained that exceed the energy density of lithium-ion batteries several times [13].

Lithium-air batteries consist of two electrodes between which the electrolyte exists (Figure 1-3). The anode is made of metallic lithium; the cathode is an air-permeable grating in carbon nanostructure, incorporated into the oxygen. The oxygen required for the reaction is obtained from the air.

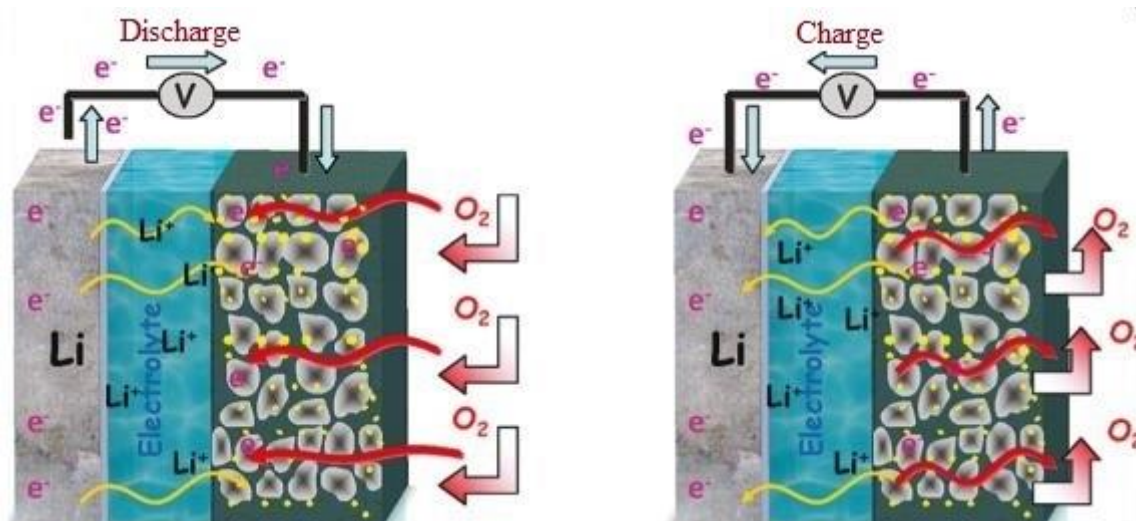
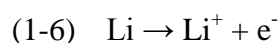


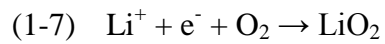
Figure 1-3 Schematic of lithium-air battery charge and discharge cycles [11]

The electrically conductive electrolyte is a solid electrolyte or an organic solvent. While charging, the lithium ions move from the cathode through the electrolyte to the anode and release oxygen into the air [11].

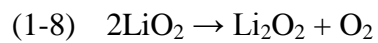
During discharge, the lithium atoms at the anode release electrons through the connected circuit:



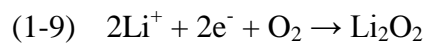
The lithium ions migrate from the anode through the electrolyte to the cathode where they react with oxygen from the air:



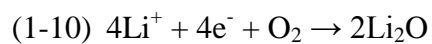
And then probably decomposes to lithium peroxide:



Or make it directly superoxide anions which with lithium ion form lithium peroxide:



Besides the formation of lithium peroxide and Lithium superoxide, the formation of lithium oxide is also possible:



1.3 Differential Electrochemical Mass Spectrometry (DEMS)

Differential Electrochemical Mass Spectrometer (DEMS) is an in-situ method, which is suitable for the study of electrochemical processes at the metal/electrolyte phase boundary. This method was developed by Wolter and Heitbaum [14]. With DEMS volatile products of an electrochemical reaction can be detected on-line both qualitatively and quantitatively. Parallel to the current-voltage curves (CV), a so-called mass spectrometric cyclic voltammogram (MSCV) is usually added. By this means, it is possible to determine the dependence of the potential of the formation of electrochemical reaction products.

In comparison to other in-situ methods (such as scanning tunneling microscopy and IR spectroscopy), DEMS offers the advantage of ease of handling and a low measurement time.

The first DEMS measurements were performed with a polycrystalline porous platinum electrode. Hartung et al. optimized DEMS for the use of solid electrodes (polycrystalline or monocrystalline) [15] and developed a special thin-layer cell for this purpose.

Another type of thin-layer cell has been designed by Jusys et al. [16]. The design principle of this coupled cell is based on the spatial separation of the electrode and the region of the cell that includes the transition of the detected species across the membrane into the mass spectrometer.

The main goals of this work are initially to characterize this coupled thin-layer cell and then to determine the solubility and diffusion coefficient of oxygen in various aqueous and non-aqueous solvents by use of achieved equations. For that, a detailed investigation of the hydrodynamic conditions in this flow cell is required and the main interest is investigation of flow rate dependence of faradaic and ionic current for different substances.

Data presented in the following study refer to the flow rate dependence of faradaic current, and also the ion current. At this point, the hydrodynamic behaviour of a "laminar flow channel", and the "wall jet" behaviour is discussed. In the case of "laminar channel flow" the flow is parallel to a plate (electrode), which is built in a rectangular channel (Figure 1-4). It is characteristic of this type of flow that only diffusion causes perpendicular mass transport to direction of the electrode or membrane. At "wall jet", the electrolyte is flown normal to the electrode surface and then guided away, after contact with the electrode from its environment (Figure 1-5) [17].

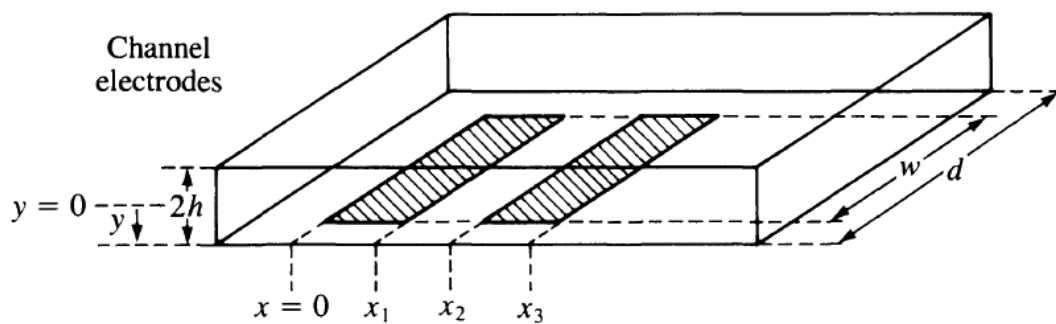


Figure 1-4 Channel electrodes: Coordinates used for common hydrodynamic electrode geometries [18]

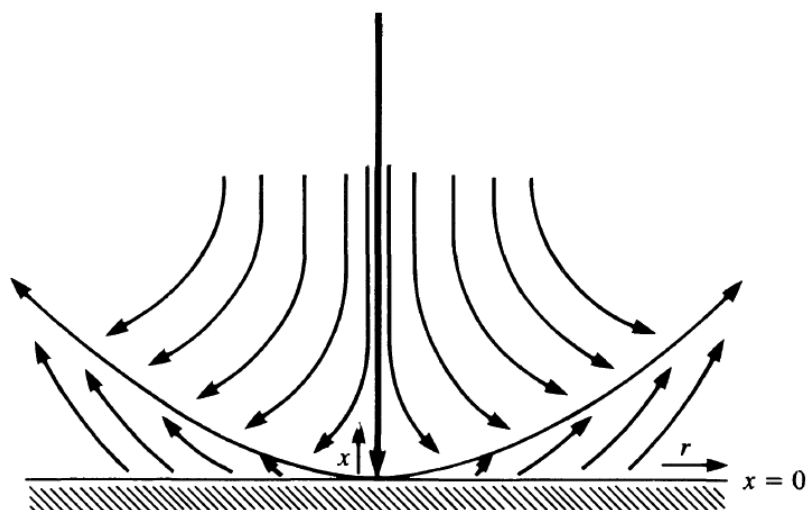


Figure 1-5 The wall-jet electrode: schematic streamlines [18]

Matsuda [17] developed a relationship between diffusion limited current and the flow rate for channel electrodes, based on the fundamental considerations of Levich (eq. 1-11) [19].

$$(1-11) \quad I_F = 1.47 \cdot z \cdot F \cdot c \cdot (D \cdot A / b)^{2/3} \cdot u^{1/3}$$

I_F : diffusion limited current (A)

z : number of electron transfer

F : Faraday constant (C/mol)

c : concentration (mol/ cm³)

D : diffusion coefficient (cm² .s⁻¹)

A : electrode area (cm²)

b : channel height (cm)

u : flow rate (cm³ .s⁻¹)

The expression for I_F at the channel electrode is obtained by putting b instead of $2h$, A instead of $d \cdot x$, and assuming $w=d$ in figure 1-4.

Yamada and Matsuda have described the hydrodynamic conditions of the "wall-jet electrode" theoretically [20]. At "wall jet", there is a different relationship between current and the flow rate (eq. 1-12).

$$(1-12) \quad I_F = 0.898 \cdot z \cdot F \cdot c \cdot D^{2/3} \cdot \nu^{-5/12} \cdot a^{-1/2} \cdot A^{3/8} \cdot u^{3/4}$$

ν : kinematic viscosity (cm².s⁻¹)

a : diameter of the inlet capillary (cm)

The equations (1-11) and (1-12) are used in this study as guidelines for the hydrodynamic studies of the dual thin-layer flow through cell.

The characterization of the cell is done in two different ways: Cyclic Voltammetry (CV) and differential electrochemical mass spectrometry (DEMS). Cyclic Voltammetry permits the investigation of transfer efficiency and shielding factor for different flow rates by oxidation or reduction of an electrochemical species flowing through the cell. This allows determining the maximum output depending on the flow rate of electrolyte. On the other hand, differential electrochemical mass spectrometry permits the relation between electrolyte flow rate and the ionic current of detected species. Both methods facilitate the investigation of electrolyte behavior in dependency of flow rate (For more references demonstrating this dependency see [21-26]).

1.4 Steady-state mass transfer

Consider in a three-electrode cell consisting of a platinum working electrode, platinum counter electrode and a reference electrode, the reduction of a species O takes place at working electrode ($O + ne \rightarrow R$). In an actual case, the oxidized form, O, might be $\text{Fe}_2(\text{SO}_4)^{3+}$ and the reduced form, R, might be $\text{Fe}_2(\text{SO}_4)^{2+}$, with only $\text{Fe}_2(\text{SO}_4)^{3+}$ initially present at the millimolar level in a solution of 0.5 M H_2SO_4 . Once electrolysis of species $\text{Fe}_2(\text{SO}_4)^{3+}$ begins, its concentration at the electrode surface, $C(x=0)$ becomes smaller than its concentration in bulk solution (C^*) which is far from the upper working electrode surface (Figure 1-6). There exists Nernst diffusion layer (δ) at the electrode surface maintaining the concentration of $\text{Fe}_2(\text{SO}_4)^{3+}$ at C^* beyond $x = \delta$. Nernst diffusion layer refers to a virtual layer, within which the gradient of the ion concentration is constant and equal to the true gradient at the electrode-electrolyte interface [27].

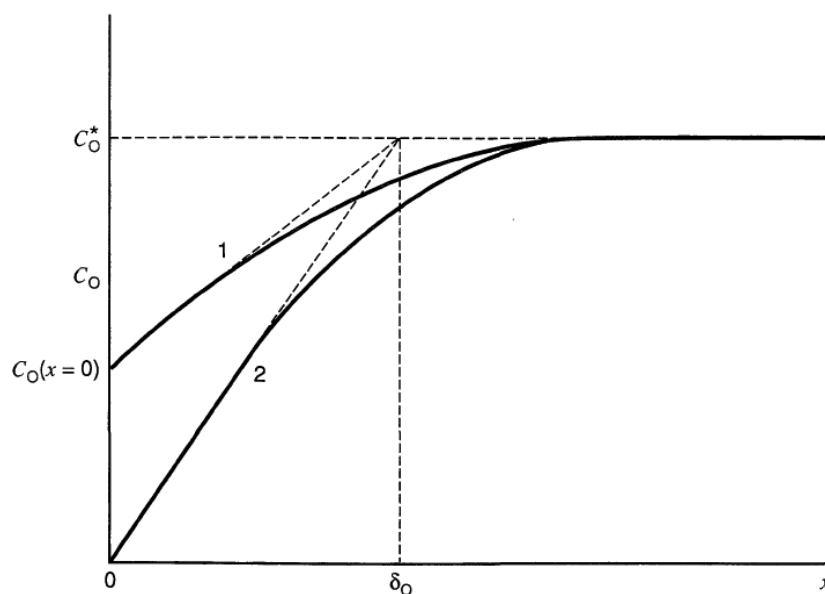


Figure 1-6 Change in concentration profiles (solid lines) and diffusion layer (dashed lines) at different electrode potentials: (1) $C(x=0) = C^*/2$, (2) $C(x=0) \approx 0$ and $i = i_{lim}$ (diffusion limited current); oxidized form, O, represents $\text{Fe}_2(\text{SO}_4)^{3+}$, electrode surface is shown with $x=0$ and δ_O is the diffusion layer thickness [27]

Chapter 2

2 Experimental

2.1 Electrochemical and mass spectrometric methods

The measurements performed in this work are carried out either through electrochemical method (cyclic voltammetry) or by mass spectrometry, and some are performed by both methods. The electrochemical method is mainly applied to characterize the cell through finding the values such as transfer efficiency, shielding factor and collection efficiency. The mass spectrometry method is used beside the characterization of the cell also to determine the solubility and diffusion coefficient of oxygen in various aqueous and non-aqueous electrolytes.

2.1.1 Cyclic Voltammetry (CV)

A typical cyclic voltammetry (CV) is based on a three-electrode setup to allow the measurement of current flowing through two working electrodes at variable potentials. The three-electrode setup consists of a working electrode, a reference electrode and a counter electrode.

By establishing a potential between working electrode and counter electrode, the current is induced and the potential of working electrode is measured against the reference electrode. To change the potential with a constant sweep rate, an external function generator is used which controls the potential change dependent on time. Cyclic voltammetry contains the specification of a triangular potential-time curve at the working electrode (Figure 2-1) and the registration of the resulting current-potential graph. The temporal change in potential is given by ν as potential scan rate (eq. 2-1).

$$(2-1) \quad \nu = dE/dt$$

ν : potential sweep rate ($\text{V}\cdot\text{s}^{-1}$)

E : applied potential (V)

t : time (s)

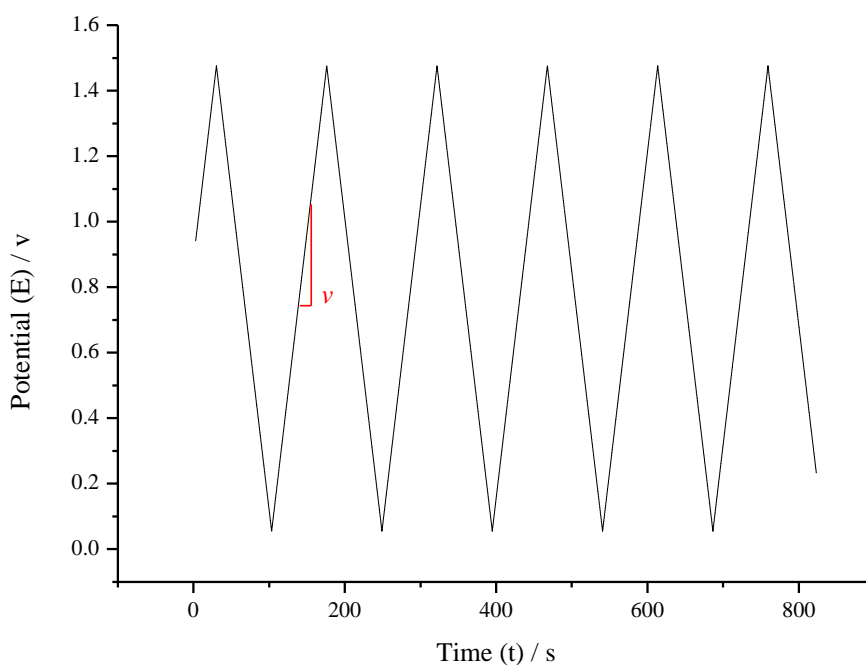


Figure 2-1 Typical potential-time curve at the working electrode

While applying a variable potential to the working electrodes, different redox-processes take place. Each process is connected to a different current flow, which can be measured in dependency on the applied potential. The resulting current-voltage-curve is called a cyclic voltammogram (CV).

Figure 2-2 shows a typical current-voltage curve recorded in dual thin-layer flow through cell for the poly crystalline platinum (poly-Pt) electrode during the adsorption in 0.5 M H₂SO₄.

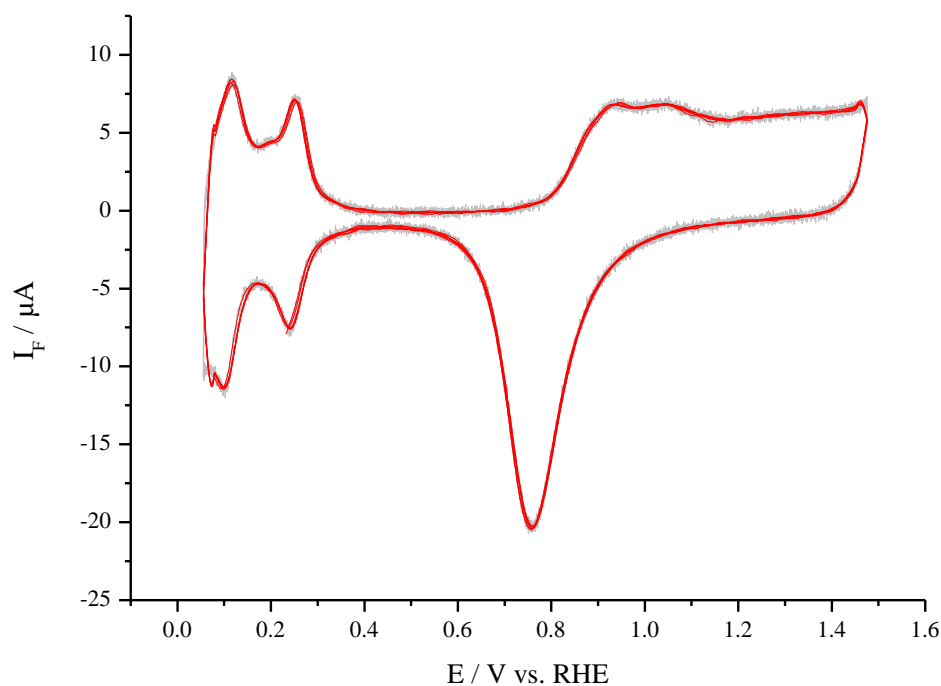


Figure 2-2 Typical CV recorded in the dual thin-layer flow through cell for Pt(Poly) during the adsorption in 0.5 M H₂SO₄; Sweep rate = 50 mVs⁻¹; electrolyte flow rate = 5 $\mu\text{l.s}^{-1}$

The experimental setup of the dual thin-layer flow through cell is shown in Figure 2-3. The main principle of this cell is the separation of both electrodes by a larger distance compared to the rotating ring disc electrode to allow kinetic studies of continuous electrochemical reactions under realistic conditions.

The cell body is made of Kel-F (Polychlorinated Trifluoroethylene). Electrolyte inlet and electrolyte outlet face each other.

The electrolyte passes through a 1 mm thick capillary first in the upper working electrode chamber where it meets perpendicularly from the bottom, flows along the surface to the outside, and leaves via six centro-symmetric capillaries (radius = 0.25 mm). These capillaries in turn flow centro-symmetrically to the surface of the lower working/detection electrode chamber. Through fine holes on the side of the cell body, Argon flushes to the ingress of atmospheric oxygen, to avoid disturbances of the measurements.

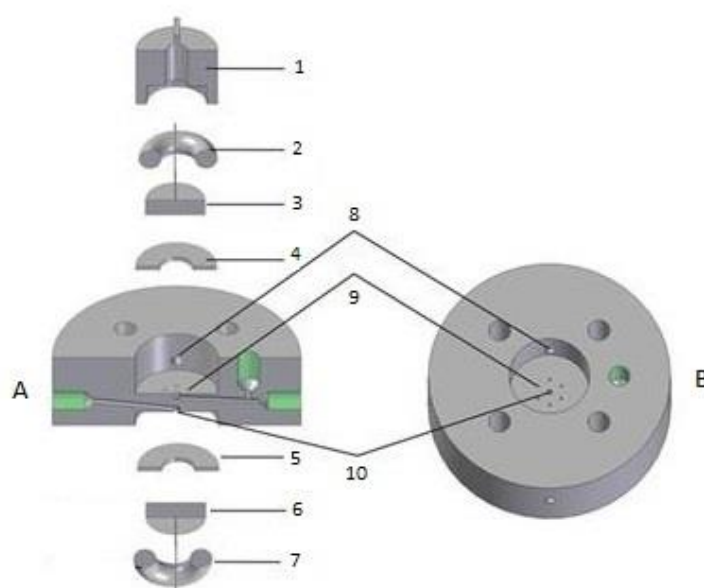


Figure 2-3 A drawing of the dual thin-layer flow through cell, (1) Kel-F support, (2,7) Kalrez O-ring, (3) upper working electrode, (4,5) Teflon spacers, (6) lower working electrode, (8) capillaries for flushing with Ar, (9) connecting capillaries, (10) inlet-outlet capillaries. (A) cross-section and (B) top-view of Kel-F cell body [28]

The upper and the lower working electrodes are made of polycrystalline platinum. The inlet of the cell contains a reference electrode with a counter electrode and the outlet contains another counter electrode for all cyclic voltammetry measurements. Both working electrodes are covered by Teflon spacers (Gortex) which allow changing the volume of the reaction area. A Teflon spacer has an inner diameter of 6 mm and a thickness of 75 μm .

2.1.2 Differential Electrochemical Mass Spectrometry (DEMS)

The structure of a DEMS system can be divided into two parts: the vacuum system with mass spectrometer and the electrochemical unit consisting of a cell with the transition to the mass spectrometer.

For this method, a quadrupole mass spectrometer (Balzers QMG-I12) was used for differential electrochemical mass spectrometry. In order to detect volatile species in solution by mass spectrometry, it has to be transferred from the electrolyte phase to vacuum. The essential part for DEMS in this study is, therefore, a dual thin-layer flow cell holding a volatile-permeable membrane to separate the electrolyte from the vacuum. The experimental setup of this cell for mass spectrometric measurements is the same as Figure 2-3, except that, the upper working electrode is replaced by a Kel-F dummy, a volatile-permeable membrane sits instead of the lower working electrode on the stainless steel frit, and the cell is mounted on the mass spectrometer by a stainless steel connection (Figure 2-4).

To get the volatile species into the mass spectrometric compartment, a constant flow is necessary. In addition, a uniform and well-reproducible flow rate must be adjusted for both methods. For this, an Aladdin programmable syringe pump is used in the outlet.

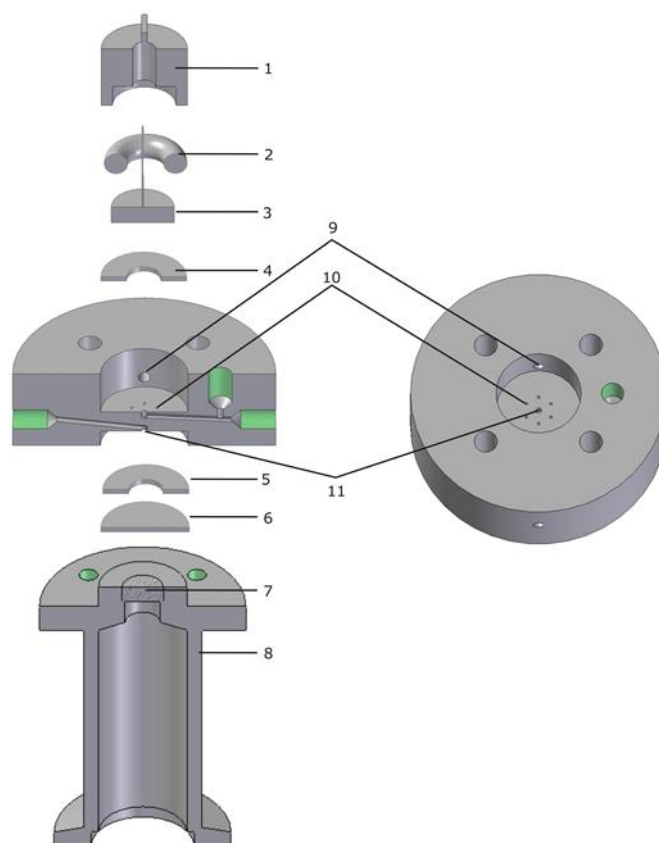


Figure 2-4 A drawing of the dual thin-layer flow through cell, (1) Kel-F support, (2) Kalrez O-ring, (3) Kel-F dummy, (4,5) Teflon spacers, (6) volatile-permeable membrane, (7) stainless steel frit, (8) stainless steel connection, (9) capillaries for flushing with Ar, (10) connecting capillaries, (11) inlet-outlet capillaries [28]

2.2 Vacuum system

For this work, DEMS facility was available. The basic structure of DEMS IV is described in the thesis of Tegtmeyer [29] in detail. DEMS IV has a Quadrupole mas-spectrometer QMG 112 from BALZERS. The schematic representation of a typical vacuum system is shown in Figure 2-5.

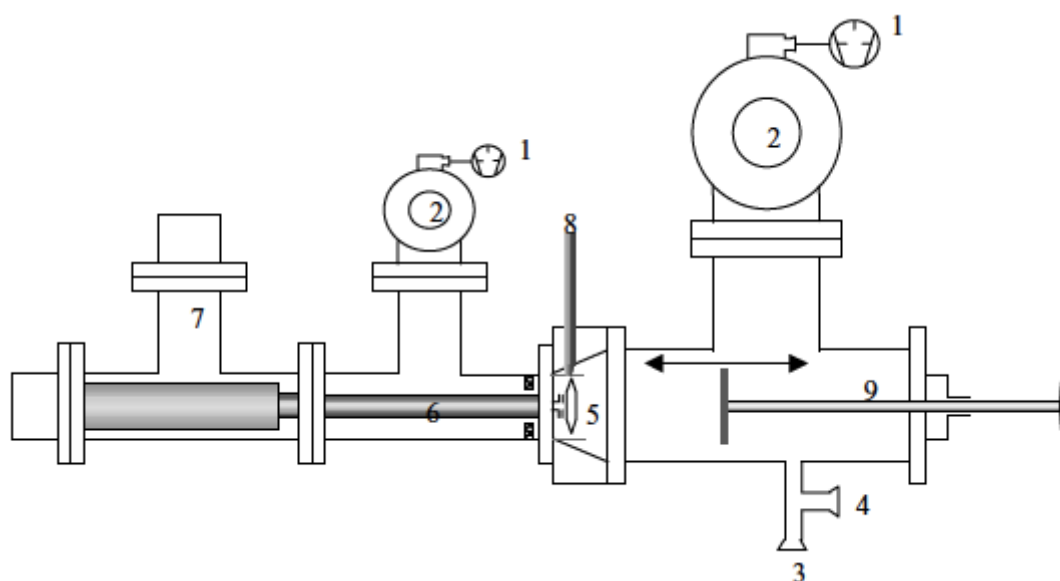


Figure 2-5 The schematic of a vacuum system: rotary pumps (1); turbomolecular pumps (2); connection to the electrochemical cell (3); connection to the calibration leak (4); ion source (5); quadrupole rods (6); secondary electron multiplier (7); direct inlet (8); linear drive (9) [30]

2.3 Calibration of system

The mass spectrometer was calibrated for O₂ through determination of calibration constant K° . The ion current I_i is proportional to the rate of amount of substance which is transferred into the vacuum system (eq. 2-2).

$$(2-2) \quad I_i = K^\circ \cdot \frac{dn}{dt}$$

I_i : ion current for the corresponding species (O₂ in this study)

K° : calibration constant of system

dn_i/dt : the flow rate of the species entering the mass spectrometer

The calibration constant contains all the properties of a mass spectrometer, such as dependence on emission current, state of the filament, etc. Thus, to keep the calibration leak measurement as close as possible to the condition of experiments, the calibration volume is attached through a dosing valve to a T-flange which is tied to both the cell and the vacuum system (Figure 2-6). This valve is also connected to a rotary pump, with which the calibration leak can be evacuated to ca. 0.02 mbar. There exists a second dosing valve which is connected to an oxygen cylinder. When one opens this valve, a certain amount of oxygen can be introduced into the evacuated leak volume.

The pressure gauge (Pressure Transducer Type 122A from MKS instruments Inc.) is directly bound to the leak volume, which can be separated from the rest part of the calibration leak through the dosing valve. By opening this valve carefully, a flow rate incoming into the vacuum system can be adjusted. So the pressure in the leak volume and ion current as function of time will be obtained. According to the ideal gas law, the amount of substance n_i can be calculated with pressure, temperature and the volume of calibration leak ($V=54.5$ mL). Figure 2-7 shows the correlation of ion current (I_i) and the flow rate of O₂ (dn_i/dt) entering the mass spectrometer. As shown in equation (2-2), the slope of this plot will be the calibration constant K° ($=0.015$ C.mo1⁻¹).

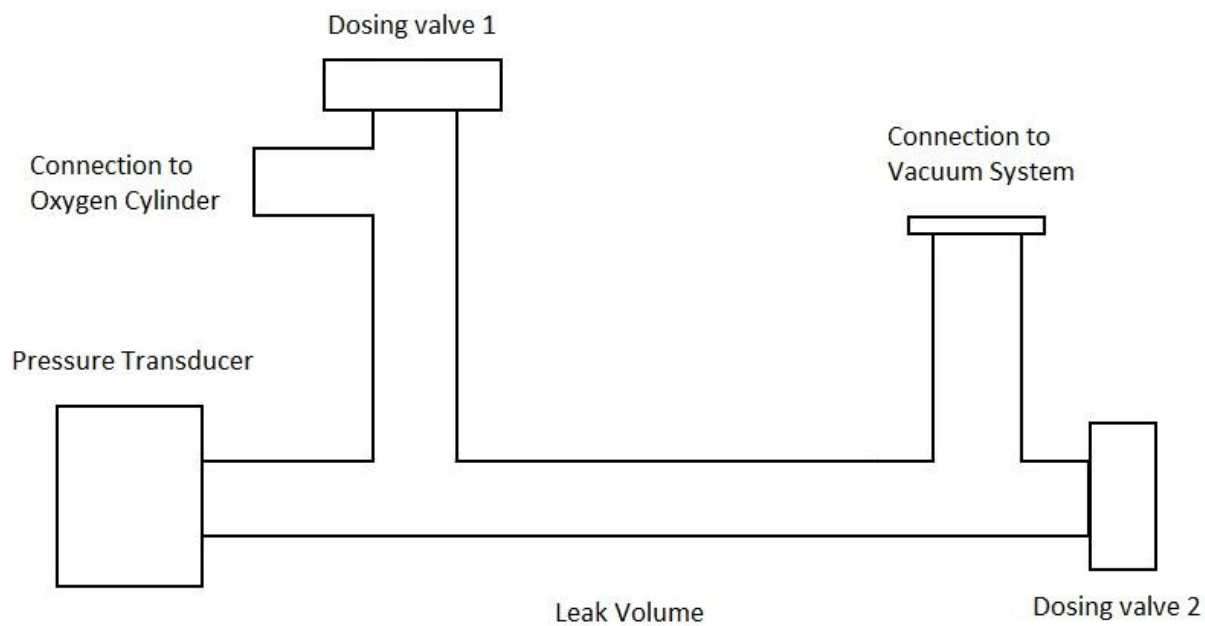


Figure 2-6 A drawing of calibration volume

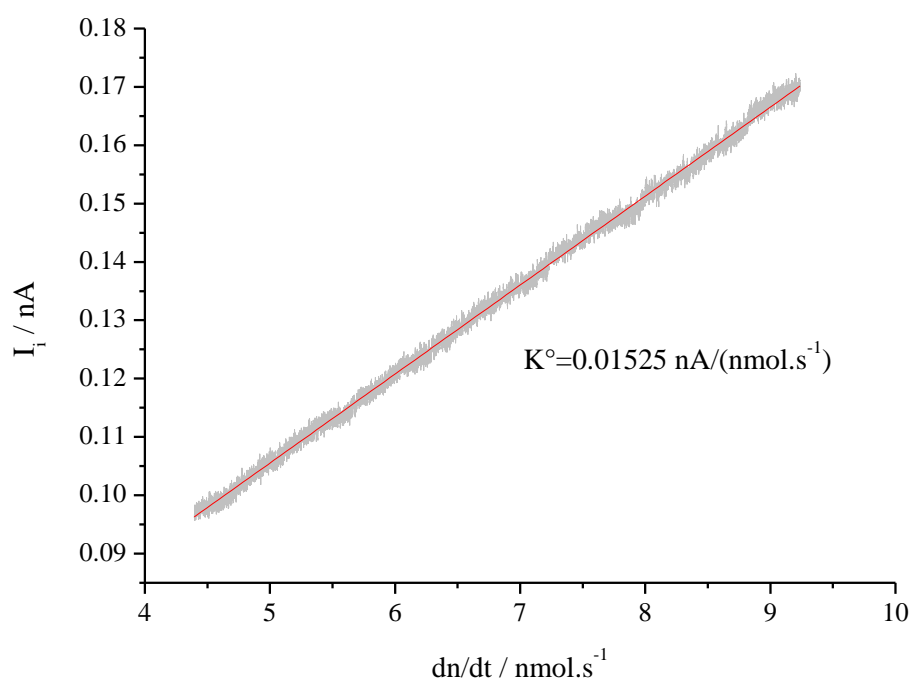


Figure 2-7 Correlation of ion current ($m/z=32$) with the flow rate of O_2 entering from the calibration leak volume into the mass spectrometer

The sensitivity of the mass spectrometer is changing, mainly due to the wear of the filament, especially when organic substances are used. Therefore, the calibration measurements must be done every day at least twice, preferably before and after the work.

2.4 Chemicals

The gases and chemicals used in this work are summarized in table 2-1.

Table 2-1 List of chemical and gases

Name	Molecular Formula	Company	Purity
Sulphuric acid	H ₂ SO ₄	EMSURE	95-97 %
Hydroquinone	C ₆ H ₆ O ₂	FLUKA	≥ 99 %
Iron(III) sulphate	Fe ₂ (SO ₄) ₃ .H ₂ O	KMF	99 %
Methyl formate	C ₂ H ₄ O ₂	SIGMA-ALDRICH	99 %
Methanol	CH ₄ O	MERCK	99.9 %
Ethanol	C ₂ H ₆ O	MERCK	≥ 99.9 %
Acetone	C ₃ H ₆ O	SIGMA-ALDRICH	≥ 99.5 %
Lithium hydroxide monohydrate	LiOH.H ₂ O	SIGMA	≥ 99 %
Potassium hydroxide	KOH	ACROS	99.98 %
Propylene carbonate	C ₄ H ₆ O ₃	SIGMA-ALDRICH	99.7 %
Dimethyl sulfoxide	C ₂ H ₆ OS	ACROS	99.8 %
Tetraethylene glycol dimethyl ether	C ₁₀ H ₂₂ O ₅	ACROS	99 %
N-Methyl-2-pyrrolidone	C ₅ H ₉ NO	SIGMA-ALDRICH	99.5 %
Lithium perchlorate	LiClO ₄	SIGMA-ALDRICH	≥ 98 %
Magnesium perchlorate	Mg(ClO ₄) ₂	SIGMA-ALDRICH	≥ 98 %
Hydrogen	H ₂	AIR LIQUIDE	99.9999 %
Argon	Ar	AIR LIQUIDE	99.999 %
Oxygen	O ₂	AIR LIQUIDE	99.9995 %

Highly pure argon (99.999%, AIR LIQUIDE) is used to prepare deaerated solutions and highly pure oxygen gas (99.9995%, AIR LIQUIDE) at atmospheric pressure and room temperature (25 ± 2 °C) for approximately 1 h prior to analysis is used. The aqueous electrolytes were prepared in 18.2 M Ω Milli-Q water.

The required glasses, Teflon and Kel-F parts are cleaned by 5 M potassium hydroxide to remove organic contamination. In addition, inorganic impurities are removed by immersion in a chromic acid bath.

2.5 Electrodes

As a reference electrode a reversible hydrogen electrode is used (RHE). The RHE consists of a platinum wire, which is surrounded by a downwardly open glass jacket. Hydrogen is previously developed in this glass jacket. All potentials in this work refer to the reversible hydrogen electrode. As a counter electrode platinum wires are used with 0.7 mm diameter. The working electrode is a polycrystalline platinum cylinder with an end surface of about 1 cm². However, the usable working electrode area is 0.28 cm² due to the Teflon spacer (Figures 2-3 and 2-4).

For the determination of the surface concentration of the adsorbate, it is necessary to determine the real surface area (A_{real}). The current flows are all caused by the adsorption and desorption of hydrogen and oxygen as well as the charging of the Helmholtz double layer.

Considering a perfectly flat polycrystalline platinum surface and assuming that one hydrogen atom adsorbs on every available platinum atom on the surface, the adsorption charge has a value of 210 $\mu\text{C}/\text{cm}^2$. The true surface of the electrode is larger due to edges and dislocations and can be determined by integrating the area of hydrogen adsorption in the CV between 0.08 and 0.4 V and dividing the resulting value Q_H through the value of a perfectly flat surface layer.

$$(2-3) \quad A_{real} = \frac{Q_H}{210 \mu\text{C} \cdot \text{cm}^{-2}}$$

The ratio between the perfectly flat surface and the true surface is called roughness factor R and is defined by the value for the real surface area divided by the value for the geometrically calculated flat surface.

$$(2-4) \quad R = \frac{A_{real}}{A_{geom}}$$

The potential limits of the CV in aqueous solution must be set between 0 and 1.6 V; otherwise the solvent decomposes into hydrogen and oxygen. Both evolving gases can block the surface thus disturb the measurement.

2.6 Data acquisition

The control during the measurements and data acquisition is performed with LabVIEW 8.5 program installed on a Personal Computer (e-chem31 - DEMS IV). One molecular fragment can be detected. As an interface to the computer an A/D converter board is used (PCI-6221: 68-pin).

Cyclic voltammograms were smoothed using the evaluation program OriginLab 8.0. For this purpose, a mathematical calculation is carried out. In OriginLab, this is referred to as FFT filter Smoothing. This smoothing is carried out over 10 or more measurement points. With this method, it is possible to almost completely suppress the background noise of the electrochemical and ion currents.

Chapter 3

Results and discussion

3 Characterization of dual thin-layer flow through cell

3.1 Theoretical aspects

3.1.1 Collection efficiency

The collection efficiency of a thin-layer cell is the ratio of the number of reacting species \dot{n} to the number of species entering the cell which is given by $c \cdot u$.

The collection efficiency for the upper compartment is calculated through the following equation:

$$(3-1) \quad f_{F1} = \frac{\dot{n}}{c \cdot u} = \frac{I_{F1} / zF}{c \cdot u}$$

I_{F1} : the amount of diffusion limited faradaic current of the first working electrode

z : number of electrons in reaction,

F : Faraday constant

c : concentration

u : electrolyte flow rate

And the collection efficiency for the lower compartment is the ratio of the number of reacting species on the second electrode \dot{m} , when no reaction takes place in the upper compartment (open potential), to the number of species entering the cell ($c \cdot u$). I_{F2} is the amount of diffusion limited current of the second working electrode.

$$(3-2) \quad f_{F2} = \frac{\dot{m}}{c \cdot u} = \frac{I_{F2} / zF}{c \cdot u}$$

Similarly, in case of having mass spectrometric part, the collection efficiency f_i is given by:

$$(3-3) \quad f_i = \frac{I_i}{K^\circ \cdot c \cdot u}$$

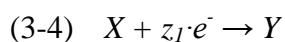
I_i : the ionic current of species detected in mass spectrometer

K° : the leak calibration constant

c : the concentration of the product in the fluid leaving the electrochemical part of the cell

3.1.2 Transfer efficiency

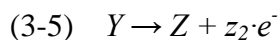
The transfer efficiency in a dual thin-layer flow through cell with two working electrodes is based on an electrochemical reaction which takes place on both electrodes. The first electrode forms an electrochemical species in solution by oxidation or reduction which then is transferred to the second electrode.



X : the starting material (educt) and

z_1 : the number of electrons reacted in upper compartment (first working electrode)

The stable reaction product of the first reaction step (Y) diffuses to the second electrode where the opposite reaction (oxidation or reduction) or any further oxidation or reduction takes place.



Z : the reaction product of lower compartment (second working electrode)

z_2 : the number of electrons reacted in the lower compartment

The second electrode has a different applied potential than the first electrode thus controlling the single reaction steps. In both cases, a current flow can be measured allowing calculation of the amount of charge transfer. The proportionality constant of both flowing diffusion limited currents on both electrodes is called transfer efficiency N .

$$(3-6) \quad N = \frac{\dot{m}}{\dot{n}}$$

\dot{m} : reaction rate in the lower compartment ($\dot{m} = \frac{dm}{dt}$)

\dot{n} : reaction rate in the upper compartment ($\dot{n} = \frac{dn}{dt}$)

In case of a reversible reaction where in both upper and lower electrodes the amount of electron flow per reaction step is the same, the equation can be simplified to:

$$(3-7) \quad N = \left| \frac{I_{F2}^P}{I_{F1}} \right|$$

I_{F2}^P : the diffusion limited current (product) in the lower compartment ($I_{F2} = z_2 \cdot \dot{m}$)

I_{F1} : the diffusion limited current in the upper compartment ($I_{F1} = z_1 \cdot \dot{n}$)

The transfer efficiency takes a value between 0 and 1 since it is not possible to convert more particles in the second reaction step than have been formed in the first reaction step.

At the low flow rate, since the gases or volatile species electrochemically produced on the electrode have enough time to mix in the solution (complete mixing) the transfer efficiency N is identical to the collection efficiency of the mass spectrometric part of the cell f_i and therefore:

$$(3-8) \quad I_i = f_i \cdot K^\circ \cdot I_F / (z \cdot F) = N \cdot K^\circ \cdot I_F / (z \cdot F)$$

And at the high flow rates, due to having less time to mix in the solution (incomplete mixing of the products), consequently, near the Teflon membrane the concentration of these species is higher, thus the transfer efficiency is higher than collection efficiency [28].

3.1.3 Shielding factor

One of the most common experiments at Rotating Ring-Disk Electrode (RRDE) is shielding experiment, where the flow of bulk electroactive species to the ring (second working electrode in these measurements) is perturbed because of the disk (first working electrode in this work) reaction [27].

To determine the shielding factor S , a potential is applied to both electrodes to form the same electrochemical species.

A part of the starting material X flows to the lower compartment and continues the same reaction that had in the upper compartment. Since the current flow is decreased on the second electrode and it is impossible to form more electrochemical species on the second electrode at the same electrode potentials, the shielding factor must have a value between 0 and 1.

There exist two different measurements for comparison: the first measurement with the same potential on both electrodes to form the same electrochemical species in solution and the second measurement with an open potential on the first electrode to determine the possible current flow without decreasing by the first electrode. The current flow is lowered by the lower concentration of electrochemical species in solution by the lowering factor N .

$$(3-9) \quad I_{F_2}(E_1 = E_2, E_2) = I_{F_2}(open, E_2) - N \cdot I_{F_1}$$

$I_{F_2}(E_1=E_2, E_2)$: the diffusion limited current of second working electrode while the first electrode (E_1) and the second electrode (E_2) have the same applied potential

$I_{F_2}^0(open, E_2)$: the diffusion limited current of the second working electrode when no potential is applied on the first working electrode (no reaction) and potential of E_2 is applied on the second working electrode

I_{F_1} : the diffusion limited current of first working electrode while potential of E_1 is applied

The ratio between both current flows $I_{F2}(E_1, E_2)$ and $I_{F2}(open, E_2)$ on the second electrode gives the shielding factor S .

$$(3-10) \quad S = \frac{I_{F2}(E_1 = E_2, E_2)}{I_{F2}(open, E_2)} = \frac{I_{F2}}{I_{F2}^0}$$

Thus, the relation between transfer efficiency, N , and shielding factor, S , will be:

$$(3-11) \quad S = 1 - N \cdot \frac{I_{F1}}{I_{F2}^0}$$

3.2 Hydroquinone / Quinone

All hydroquinone measurements were done with a 10^{-3} M hydroquinone solution in 0.5 M sulphuric acid. The redox-system of hydroquinone is shown in Figure 3-1; hydroquinone can be oxidized to quinone by the release of two electrons and two protons.

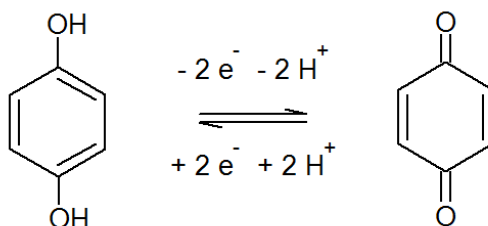


Figure 3-1 Redox-system of hydroquinone and quinone

Hydroquinone was oxidized to quinone at the upper working electrode during potential sweeps between 0.4 and 1.1 V while two different potentials were applied to the lower working electrode: 0.5 V to reduce quinone back to hydroquinone and 1.0 V to oxidize the remaining hydroquinone to quinone. All measurements were done for 10 different electrolyte flow rates in the range of 0.1 - $80 \mu\text{l}\cdot\text{s}^{-1}$. The spectra of the measurements at electrolyte flow rate of $5 \mu\text{l}\cdot\text{s}^{-1}$ is shown in Figure 3-2, and the measurements for different flow rates (0.1 to $80 \mu\text{l}\cdot\text{s}^{-1}$) are shown in Figures 3-3 and 3-4.

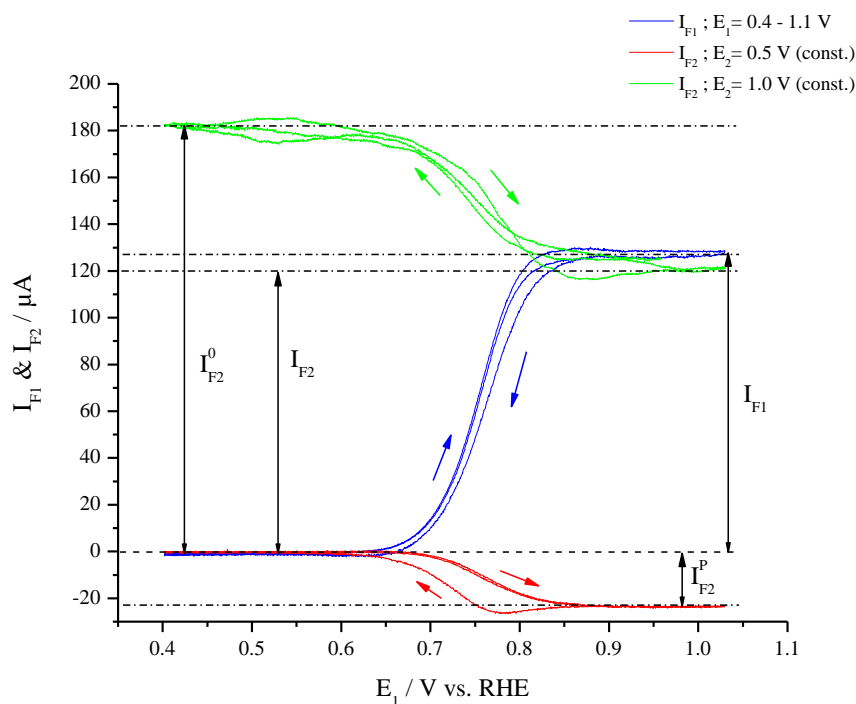


Figure 3-2 10^{-3} M hydroquinone in 0.5 M H_2SO_4 ; sweep rate: 5 mV/s; $E_1 = 0.4 - 1.1$ V, $E_2 = 0.5$ V (const.) (red curve); $E_2 = 1.0$ V (const.) (green curve); electrolyte flow rate: $5 \mu\text{l}\cdot\text{s}^{-1}$

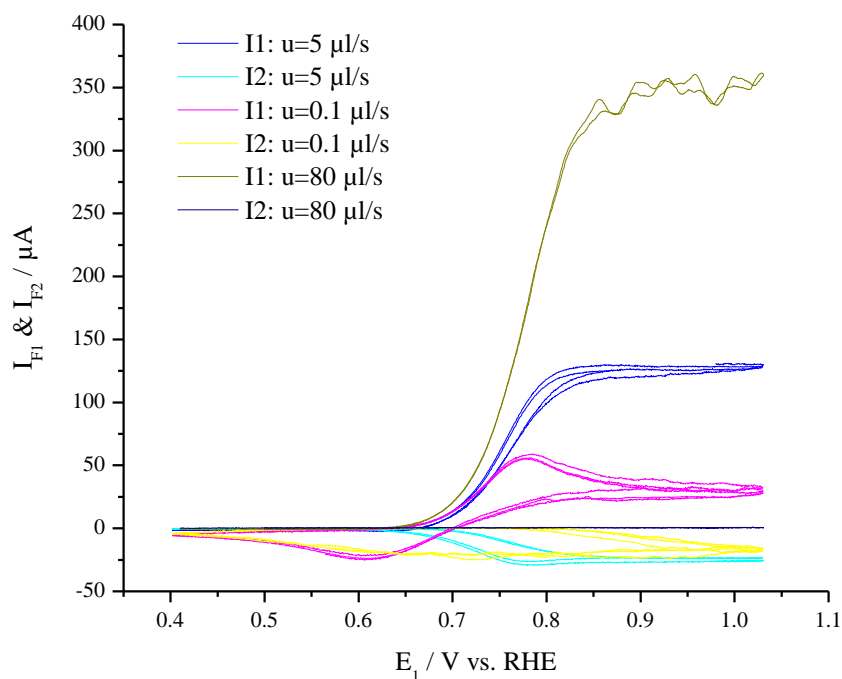


Figure 3-3 10^{-3} M hydroquinone in 0.5 M H_2SO_4 ; sweep rate: 5 mV/s; $E_1 = 0.4 - 1.1$ V, $E_2 = 0.5$ V (const.); electrolyte flow rates: $0.1, 5, 80 \mu\text{l}\cdot\text{s}^{-1}$

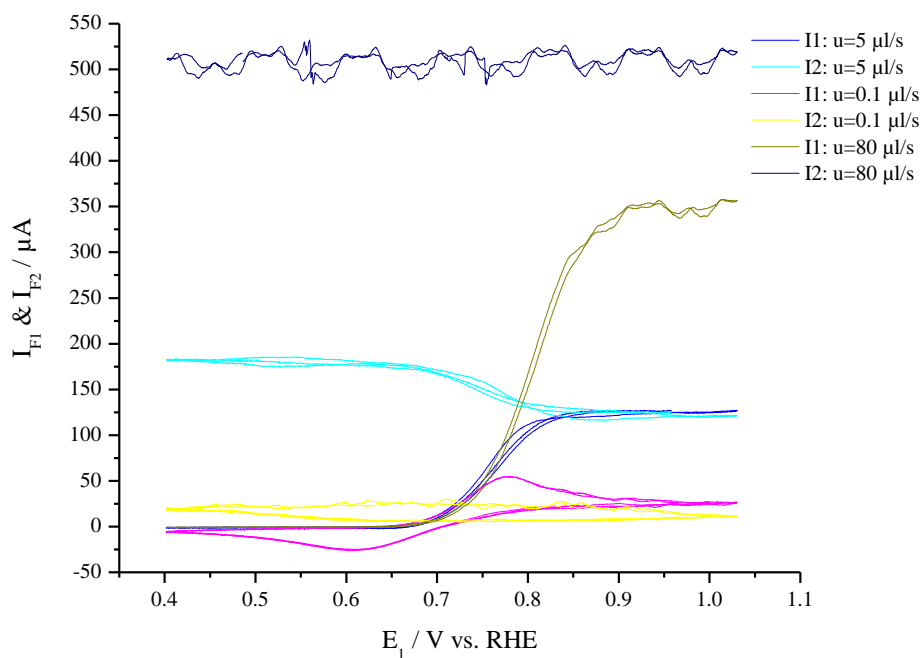


Figure 3-4 10⁻³ M hydroquinone in 0.5 M H₂SO₄; sweep rate: 5 mV/s; $E_1 = 0.4 - 1.1$ V, $E_2 = 1.0$ V (const.); electrolyte flow rates: 0.1, 5, 80 $\mu\text{l}\cdot\text{s}^{-1}$

As seen in Figures 3-3 and 3-4, for low flow rates of electrolyte, there still remains some quinone which is reduced to hydroquinone.

3.3 $\text{Fe}^{2+} / \text{Fe}^{3+}$

For all iron measurements, electrolyte of 10^{-3} M $\text{Fe}_2(\text{SO}_4)_3$ in 0.5 M H_2SO_4 was used. The redox-system in solution to be investigated is the reduction of Fe^{3+} to Fe^{2+} (Figure 3-5).

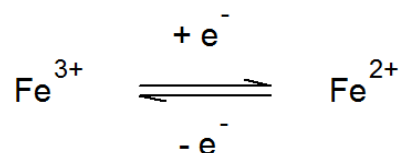


Figure 3-5 Redox-system of Iron (III) and Iron (II)

The reduction of Fe^{3+} to Fe^{2+} takes place while sweeping the potential between 0.3 and 1.0 V on the upper electrode with a constant potential of $E_2=0.5$ V on the lower electrode (Figure 3-6 – red curve) (reduction of remaining Fe^{3+} to Fe^{2+}) and a higher electrode potential of 1.0 V (oxidation of Fe^{2+} to Fe^{3+}) (Figure 3-6 – green curve). The measurements were done at 10 different electrolyte flow rates range between 0.1 - 80 $\mu\text{l}\cdot\text{s}^{-1}$ (Figures 3-7 and 3-8)

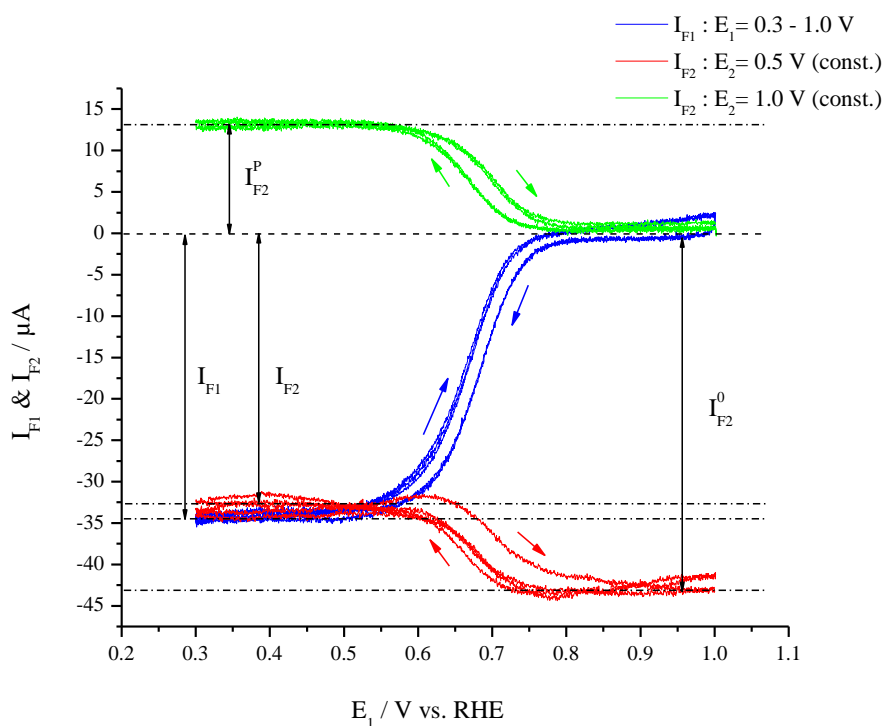


Figure 3-6 10^{-3} M $\text{Fe}_2(\text{SO}_4)_3$ in 0.5 M H_2SO_4 ; sweep rate: 5 mV/s; $E_1 = 0.3 - 1.0$ V, $E_2 = 0.5$ V (const.) (red curve) ; $E_2 = 1.0$ V (const.) (green curve); electrolyte flow rate: 5 $\mu\text{l}\cdot\text{s}^{-1}$

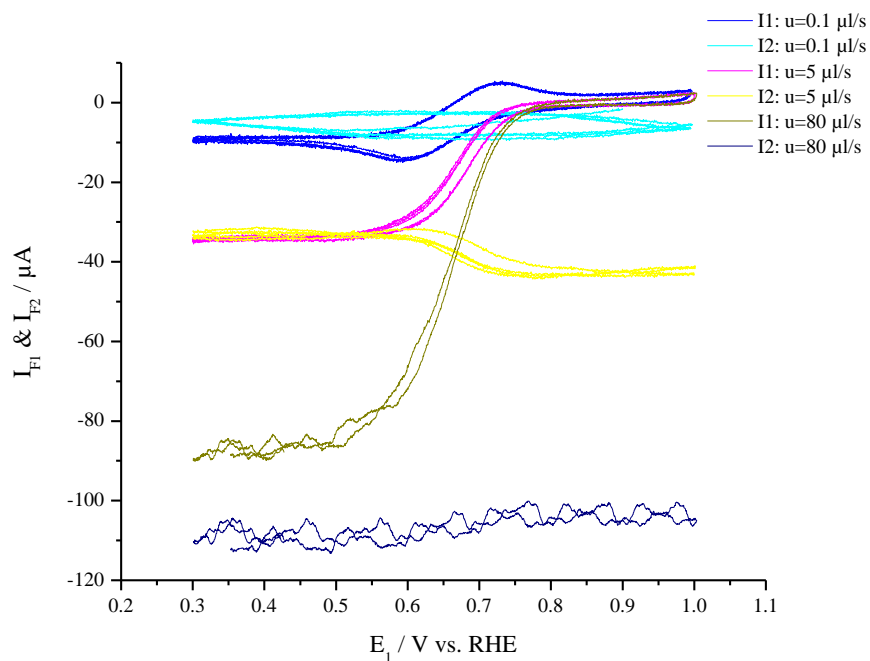


Figure 3-7 10^{-3} M $\text{Fe}_2(\text{SO}_4)_3$ in 0.5 M H_2SO_4 ; sweep rate: 5 mV/s; $E_1 = 0.3 - 1.0$ V, $E_2 = 0.5$ V (const.); electrolyte flow rates: 0.1, 5, 80 $\mu\text{l}\cdot\text{s}^{-1}$

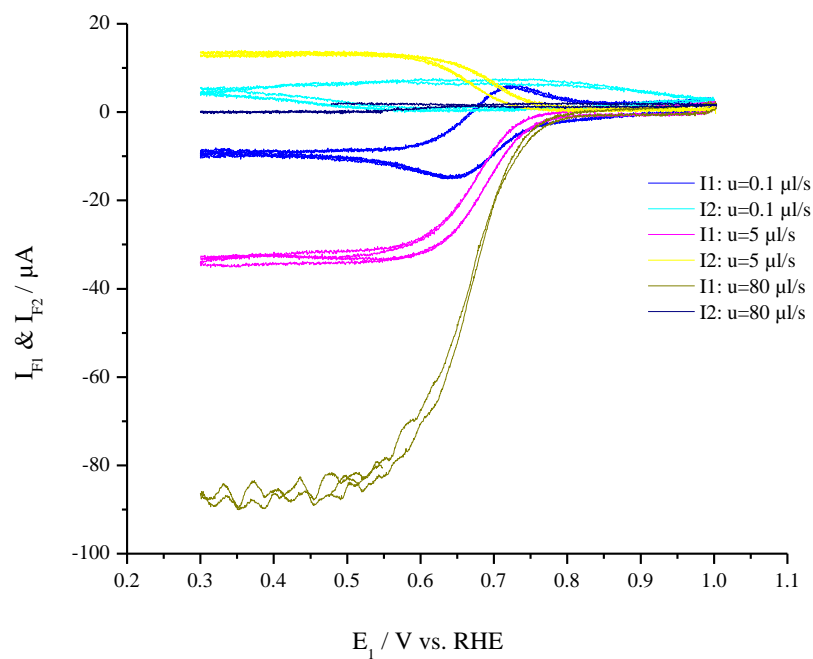


Figure 3-8 10^{-3} M $\text{Fe}_2(\text{SO}_4)_3$ in 0.5 M H_2SO_4 ; sweep rate: 5 mV/s; $E_1 = 0.3 - 1.0$ V, $E_2 = 1.0$ V (const.); electrolyte flow rate: 0.1, 5, 80 $\mu\text{l}\cdot\text{s}^{-1}$

In Figures 3-7 and 3-8 ($\text{Fe}^{2+}/\text{Fe}^{3+}$ measurements), for low flow rates of electrolytes, there exist peaks due to due to the reduction of PtO.

3.4 Dissolved hydrogen measurements

As another electrolyte, a saturated solution of H₂ in 0.5 M H₂SO₄ was prepared by bubbling H₂ through the electrolyte for 30 minutes. The following measurements were all done with this solution at flow rates range between 5 - 40 μl.s⁻¹. The redox-system in solution is the oxidation of hydrogen to protons and electrons and vice versa as seen in Figure 3-9.

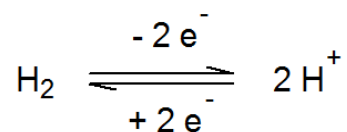


Figure 3-9. Redox-system of hydrogen and H⁺

The cyclic voltammograms of Hydrogen oxidation are shown in Figure 3-10 where the cycling potential of E₁=0.45-1.5 V is applied to the upper working electrode (solid platinum) and a constant potential of E₂=0.4 V is applied to the lower working electrode (sputtered Teflon membrane), Figure 3-12 where open circuit (E₁=0) is applied to the upper working electrode and sweeping potential of E₂=0.45-1.5 V is applied to the lower working electrode, and Figure 3-13 where sweeping potential is applied on both working electrodes (E₁=E₂=0.45-1.5 V).

Figures 3-11 and 3-14 show the same measurements with a comparison for the lowest flow rate (5 μl.s⁻¹) and the highest flow rate (40 μl.s⁻¹).

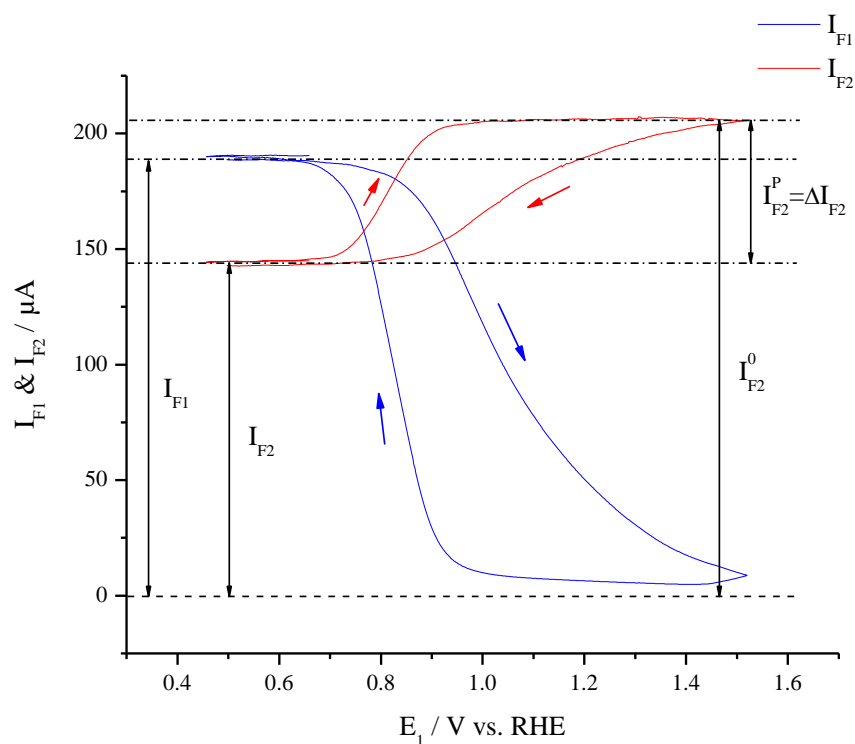


Figure 3-10 H_2 saturated 0.5 M H_2SO_4 ; sweep rate: 5 mV s^{-1} ; $E_1 = 0.45 - 1.5 \text{ V}$ (solid Pt electrode), $E_2 = 0.4 \text{ V}$ (const.) (Pt sputtered Teflon membrane); electrolyte flow rate: $10 \mu\text{l}\cdot\text{s}^{-1}$

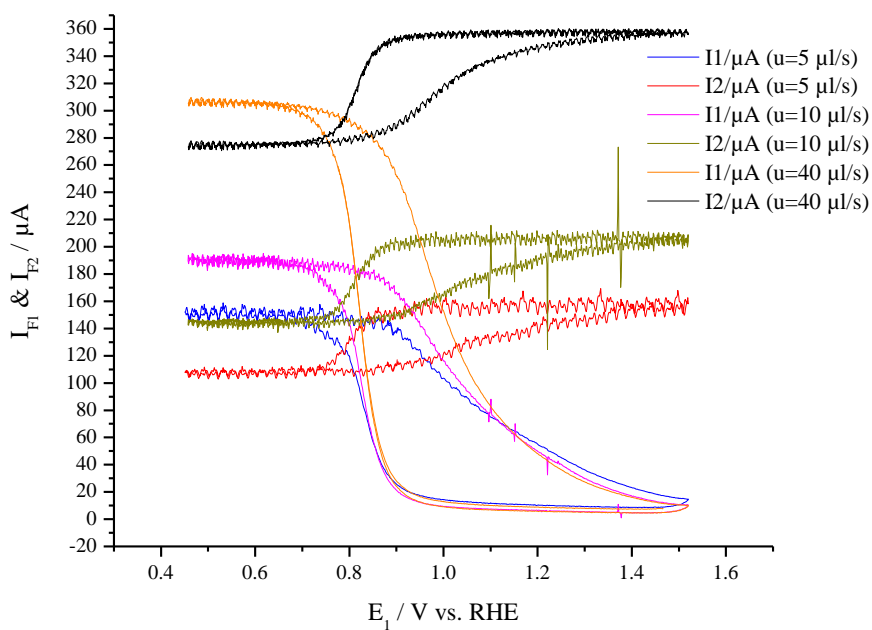


Figure 3-11 H_2 saturated 0.5 M H_2SO_4 ; sweep rate: 5 mV s^{-1} ; $E_1 = 0.45 - 1.5 \text{ V}$ (solid Pt electrode), $E_2 = 0.4 \text{ V}$ (const.) (Pt sputtered Teflon membrane); electrolyte flow rate: 5, 10, $40 \mu\text{l}\cdot\text{s}^{-1}$

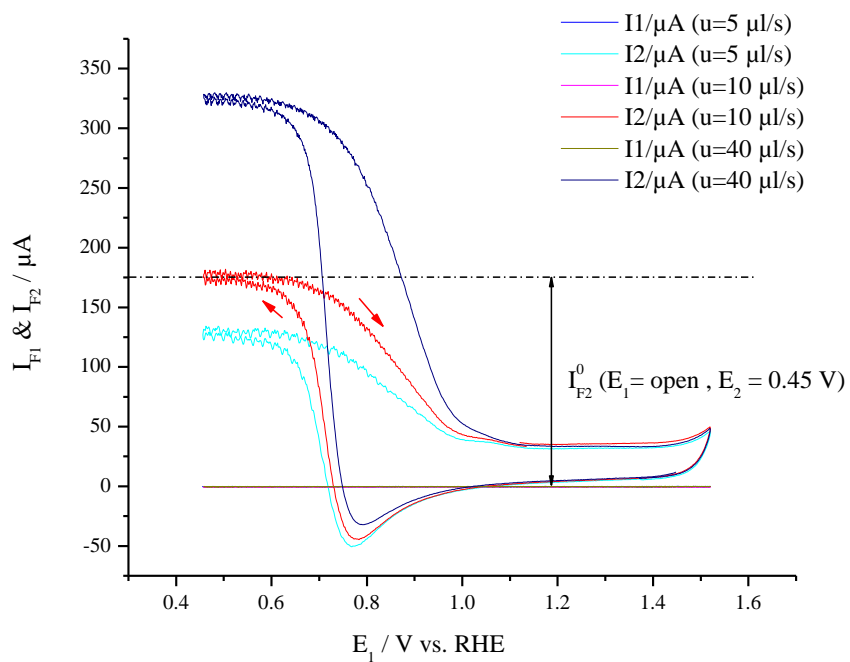


Figure 3-12 H_2 saturated $0.5 \text{ M H}_2\text{SO}_4$; sweep rate: 5 mV s^{-1} ; $E_1 = \text{open circuit}$, $E_2 = 0.45 - 1.5 \text{ V}$ (Pt sputtered Teflon membrane); electrolyte flow rate: $5, 10, 40 \mu\text{l.s}^{-1}$

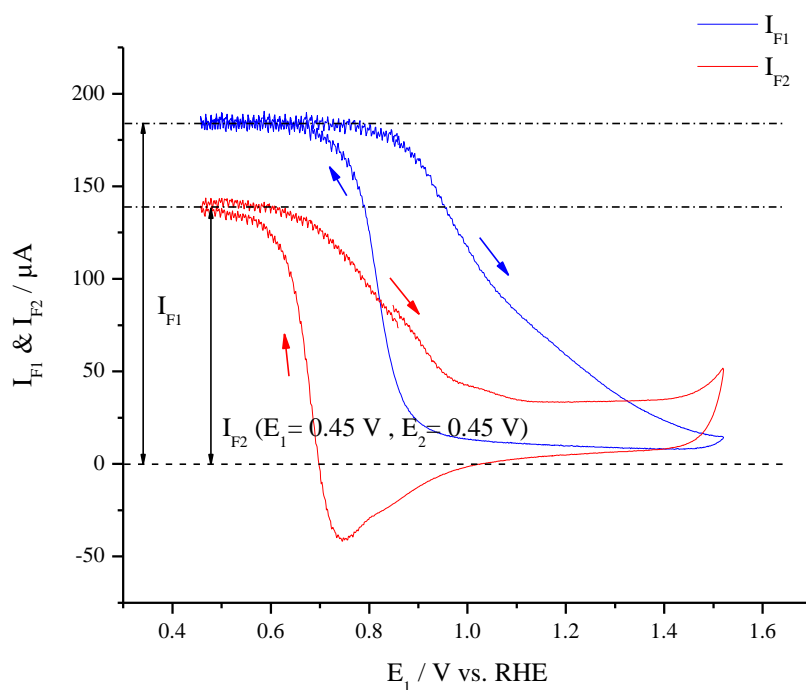


Figure 3-13 H_2 saturated $0.5 \text{ M H}_2\text{SO}_4$; sweep rate: 5 mV s^{-1} ; $E_1 = 0.45 - 1.5 \text{ V}$ (solid Pt electrode), $E_2 = 0.45 - 1.5 \text{ V}$ (Pt sputtered Teflon membrane); electrolyte flow rate: $10 \mu\text{l.s}^{-1}$

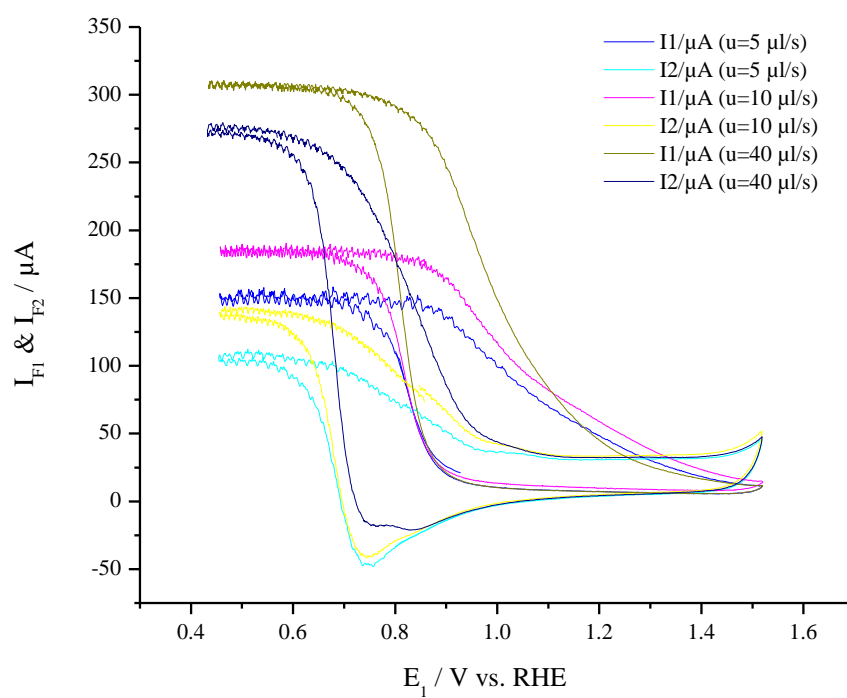


Figure 3-14 H_2 saturated 0.5 M H_2SO_4 ; sweep rate: 5 mV s^{-1} ; $E_1 = 0.45 - 1.5 \text{ V}$ (solid Pt electrode), $E_2 = 0.45 - 1.5 \text{ V}$ (Pt sputtered Teflon membrane); electrolyte flow rate: 5, 10, $40 \mu\text{l}\cdot\text{s}^{-1}$

As seen in Figures 3-12 and 3-13, in the case of $E_1 = \text{open circuit}$ and $E_1 = 0.46 - 1.5 \text{ V}$, within the negative-going scan, reduction of PtO takes place in the lower compartment.

3.5 Correlation of limiting current and flow rate

The correlation between the diffusion limited faradaic currents of the upper working electrode and lower one with the flow rates can be obtained by plotting the logarithm of currents against the logarithm of flow rates. The resulting plot should be a straight line in which the slope of the line gives the exponent of the correlation between the current and flow rates.

The correlation of diffusion limited current of the upper working electrode with flow rate is shown in Figure 3-15 and the correlation of diffusion limited current of the lower working electrode with the flow rate of electrolyte is shown in Figure 3-16. The diffusion limiting currents are obtained from a varying potential on the upper electrode. The diffusion limited currents for the lower working electrode are obtained when no reaction or open circuit exists on the upper working electrode.

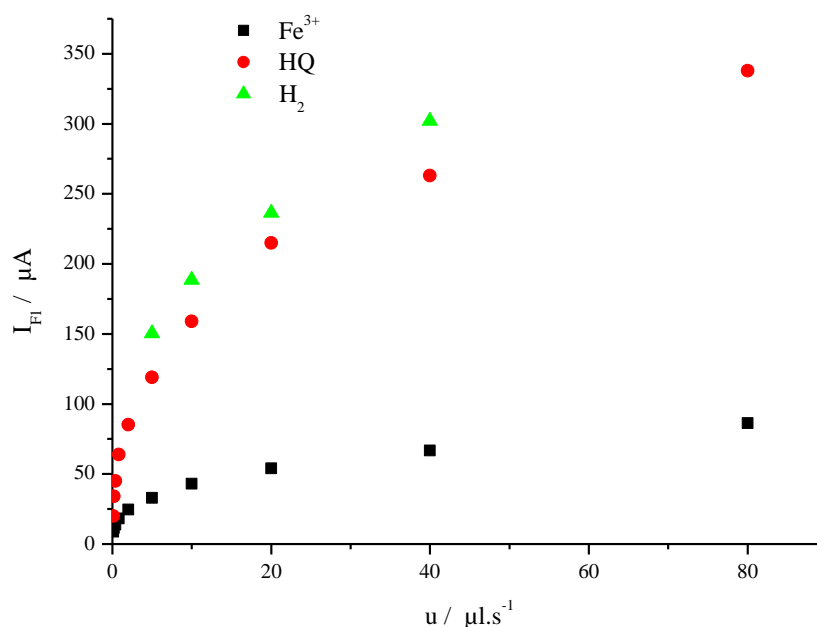


Figure 3-15 Correlation of limiting current of upper working electrode with flow rate for 10^{-3} M hydroquinone in 0.5 M H_2SO_4 (solid Pt), 10^{-3} M $\text{Fe}_2(\text{SO}_4)_3$ in 0.5 M H_2SO_4 (solid Pt) and H_2 saturated 0.5 M H_2SO_4 (solid Pt) measurements; sweep rate: 5 mV/s

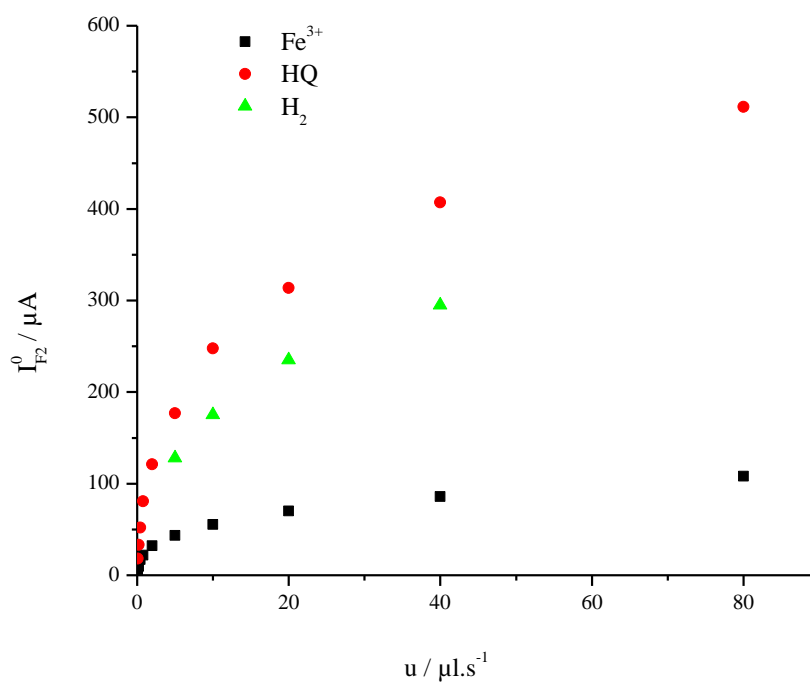


Figure 3-16 Correlation of limiting current of lower working electrode with flow rate for 10^{-3} M hydroquinone in 0.5 M H_2SO_4 (solid Pt), 10^{-3} M $\text{Fe}_2(\text{SO}_4)_3$ in 0.5 M H_2SO_4 (solid Pt) and H_2 saturated 0.5 M H_2SO_4 (porous Pt) measurements; sweep rate: 5 mV/s

As seen in Figure 3-16, the currents for H_2 oxidation in the lower compartment are lower than expected because H_2 is also consumed by transport through the porous electrode into the vacuum.

Figures 3-17 and 3-18 respectively represent expanded plots of the correlation of limiting current of the upper and lower working electrodes for low flow rate region ($u \leq 5 \mu\text{L}\cdot\text{s}^{-1}$).

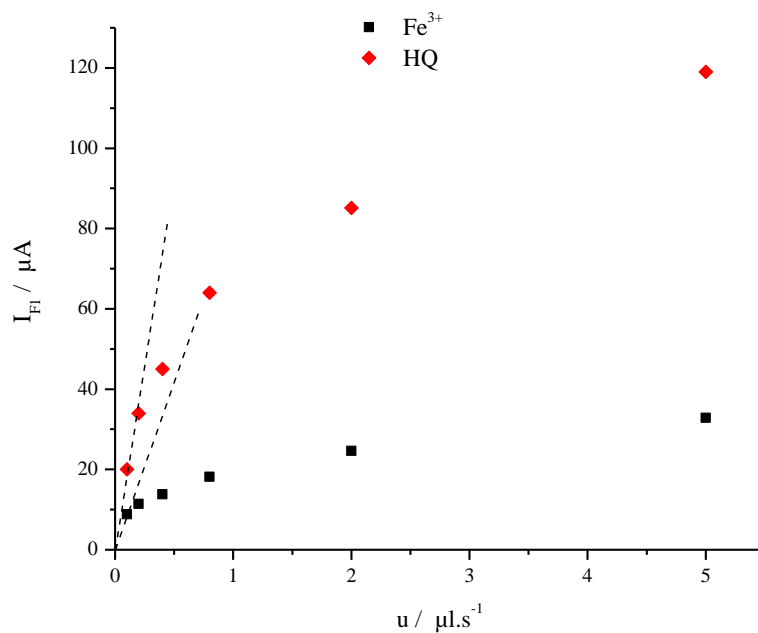


Figure 3-17 Correlation of limiting current of the upper working electrode with low flow rate ($0.1 - 5 \mu\text{L}\cdot\text{s}^{-1}$) for 10^{-3} M hydroquinone in 0.5 M H_2SO_4 (solid Pt) and 10^{-3} M $\text{Fe}_2(\text{SO}_4)_3$ in 0.5 M H_2SO_4 (solid Pt); sweep rate: 5 mV/s

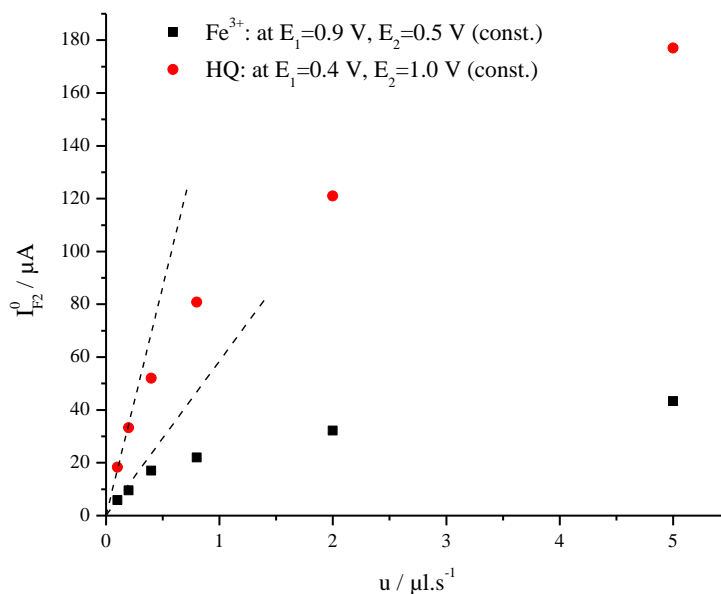


Figure 3-18 Correlation of limiting current of the lower working electrode with low flow rate ($0.1 - 5 \mu\text{L}\cdot\text{s}^{-1}$) for 10^{-3} M hydroquinone in 0.5 M H_2SO_4 (solid Pt) and 10^{-3} M $\text{Fe}_2(\text{SO}_4)_3$ in 0.5 M H_2SO_4 (solid Pt); sweep rate: 5 mV/s

The logarithmic plots of diffusion limited current of the upper working electrode and lower working electrode versus flow rate are shown in Figure 3-19 and 3-20 respectively. The obtained slopes at high flow rates for upper working electrode are 0.34, 0.33, and 0.34 for Hydroquinone/Quinone, $\text{Fe}^{2+}/\text{Fe}^{3+}$ and dissolved H_2 measurements respectively. The slope obtained for lower working electrode in all measurements is 0.33. Considering the correlation to be a linear equation in the form of $y = u^x$ with x as the exponent of the correlation, the slope x of all logarithmic plots should show the exponential behavior of limiting current depending on the flow rates. The total average of the three slopes leads to an average value of about 0.34 for the upper working electrode and 0.33 for the lower working electrode as proportionality of the logarithm of diffusion limited faradaic current to the logarithm of flow rates which represent the hydrodynamic behaviour of a "laminar flow channel" (eq. 1.11).

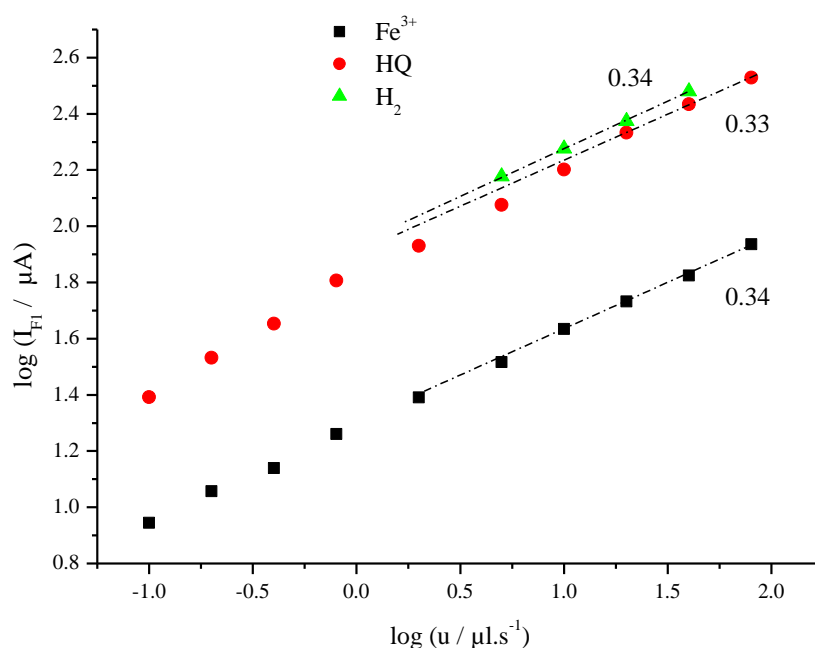


Figure 3-19 Logarithmic diagrams of limiting current of the upper working electrode with flow rate for 10^{-3} M hydroquinone in 0.5 M H_2SO_4 (solid Pt), 10^{-3} M $\text{Fe}_2(\text{SO}_4)_3$ in 0.5 M H_2SO_4 (solid Pt) and H_2 saturated 0.5 M H_2SO_4 (solid Pt) measurements; sweep rate: 5 mV/s

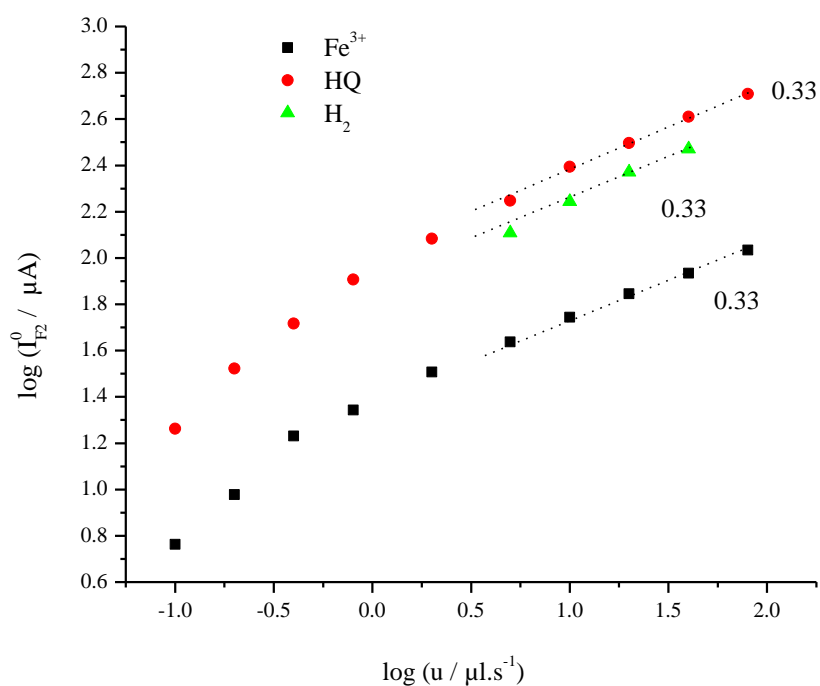


Figure 3-20 Logarithmic diagrams of limiting current of the lower working electrode with flow rate for 10^{-3} M hydroquinone in 0.5 M H_2SO_4 (solid Pt), 10^{-3} M $Fe_2(SO_4)_3$ in 0.5 M H_2SO_4 (solid Pt) and H_2 saturated 0.5 M H_2SO_4 (porous Pt) measurements; sweep rate: 5 mV/s

Figures 3-21 and 3-22 represent respectively a better correlation of diffusion limited current of the upper working electrode and lower working electrode with cubic root of the electrolyte flow rate ($u^{1/3}$) for 10^{-3} M hydroquinone in 0.5 M H_2SO_4 , 10^{-3} M $Fe_2(SO_4)_3$ in 0.5 M H_2SO_4 and H_2 saturated 0.5 M electrolytes.

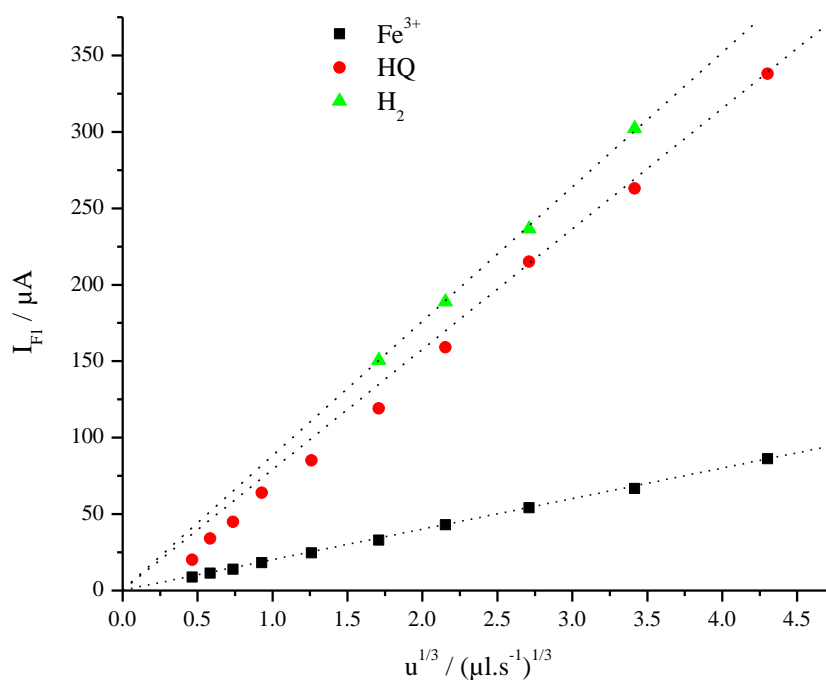


Figure 3-21 Correlation of diffusion limited current of the upper working electrode with cubic root of electrolyte flow rate ($u^{1/3}$) for 10^{-3} M hydroquinone in 0.5 M H_2SO_4 (solid Pt), 10^{-3} M $Fe_2(SO_4)_3$ in 0.5 M H_2SO_4 (solid Pt) and H_2 saturated 0.5 M H_2SO_4 (solid Pt) measurements; sweep rate: 5 mV/s

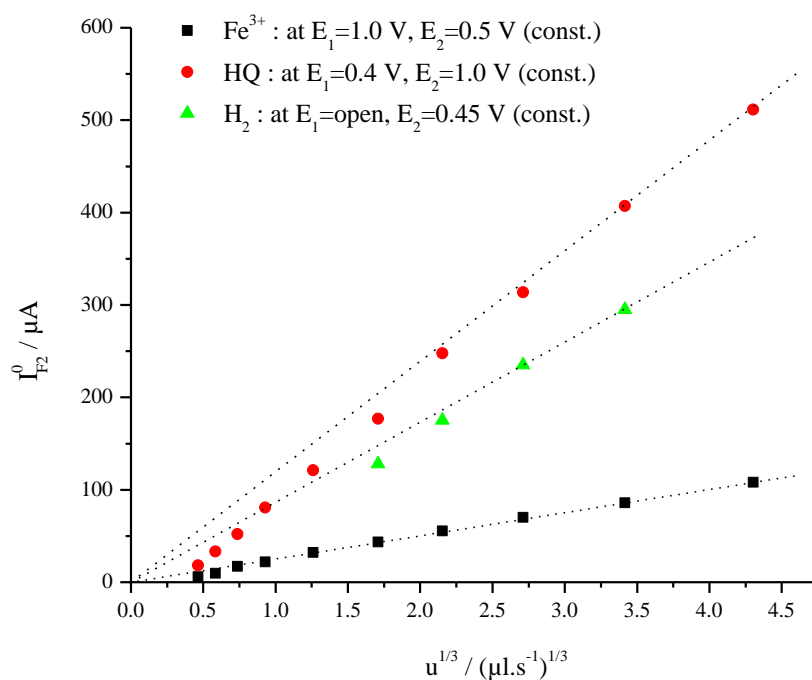


Figure 3-22 Correlation of diffusion limited current of the lower working electrode with cubic root of electrolyte flow rate ($u^{1/3}$) for 10^{-3} M hydroquinone in 0.5 M H_2SO_4 (solid Pt), 10^{-3} M $Fe_2(SO_4)_3$ in 0.5 M H_2SO_4 (solid Pt) and H_2 saturated 0.5 M H_2SO_4 (porous Pt) measurements; sweep rate: 5 mV/s

With obtaining the proportionality of the limiting current with cubic root of electrolyte flow rate ($u^{1/3}$), “the laminar channel flow” condition for our cell will be recognized. A more simplified form of eq. 1-11 will be obtained with using g as the geometric factor containing all the geometric constants of the cell:

$$(3-12) \quad I_{lim} = g \cdot z \cdot F \cdot c \cdot D^{2/3} \cdot u^{1/3}$$

I_{lim} : diffusion limited current (A)

z : number of electron transfer

F : Faraday constant (C/mol)

c : concentration (mol/cm³)

D : diffusion coefficient (cm² .s⁻¹)

u : flow rate (cm³ .s⁻¹)

g : the cell constant

With plotting the normalized limited currents of the upper and lower compartments $I_F / (zFcD^{2/3})$ versus the cubic root of the flow rate ($u^{1/3}$), the slopes give the geometry factors g . Figure 3-23 and 3-24 clearly show the obtained geometry factors of the upper and lower compartments for Fe³⁺, HQ and H₂ measurements. The numbers of spacers used in Fe³⁺ and HQ measurements are 2 for both upper and lower compartments, and for dissolved H₂ measurement this number is 4 for both upper and lower compartments. As seen, increasing the number of spacers (channel height b in eq.1-11), the value of g decreases. Theoretical values calculated for $g (=1.47 \times (A/b)^{2/3})$ are 10.5 cm^{2/3} for 2 spacers and 6.5 cm^{2/3} for 4 spacers which are very close to the experimental values.

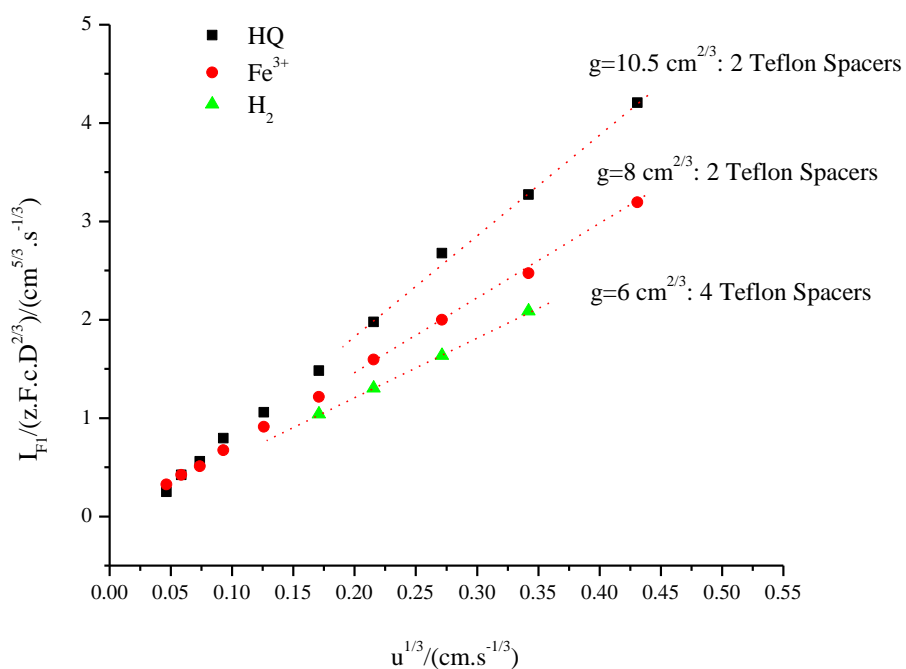


Figure 3-23 Correlation of normalized diffusion limited current of the upper working electrode with cubic root of electrolyte flow rate ($u^{1/3}$) for 10^{-3} M hydroquinone in 0.5 M H_2SO_4 ($D_{\text{HQ}}=8.5 \times 10^{-6} \text{ cm}^2 \cdot \text{s}^{-1}$), 10^{-3} M $\text{Fe}_2(\text{SO}_4)_3$ in 0.5 M H_2SO_4 ($D_{\text{Fe}^{3+}}=4.7 \times 10^{-6} \text{ cm}^2 \cdot \text{s}^{-1}$), and H_2 saturated 0.5 M H_2SO_4 ($D_{\text{H}_2}=3.7 \times 10^{-5} \text{ cm}^2 \cdot \text{s}^{-1}$, $C_{\text{H}_2}=0.75 \times 10^{-6} \text{ mol} \cdot \text{cm}^{-3}$) measurements; sweep rate: 5 mV/s. Slopes correspond to the geometry factor g . The upper working electrode in all measurements are solid Pt

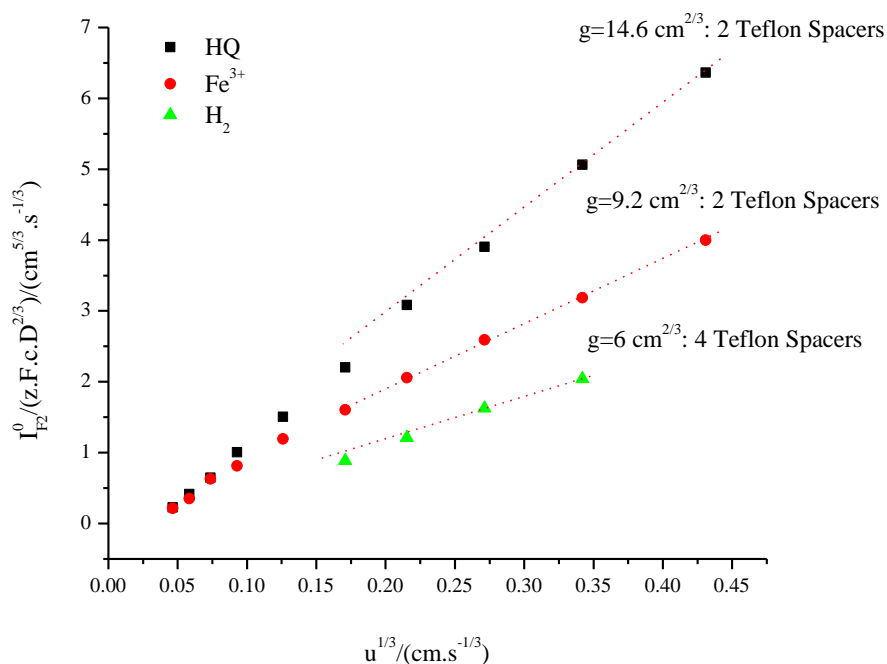


Figure 3-24 Correlation of normalized diffusion limited current of the lower working electrode with cubic root of electrolyte flow rate ($u^{1/3}$) for 10^{-3} M hydroquinone in 0.5 M H_2SO_4 ($D_{\text{HQ}}=8.5 \times 10^{-6}$ $\text{cm}^2 \cdot \text{s}^{-1}$), 10^{-3} M $\text{Fe}_2(\text{SO}_4)_3$ in 0.5 M H_2SO_4 ($D_{\text{Fe}^{3+}}=4.7 \times 10^{-6}$ $\text{cm}^2 \cdot \text{s}^{-1}$), and H_2 saturated 0.5 M H_2SO_4 ($D_{\text{H}_2}=3.7 \times 10^{-5}$ $\text{cm}^2 \cdot \text{s}^{-1}$, $C_{\text{H}_2}=0.75 \times 10^{-6}$ $\text{mol} \cdot \text{cm}^{-3}$) measurements; sweep rate: 5 mV/s. Slopes correspond to the geometry factor g . The lower working electrode for Fe^{3+} and HQ measurements is solid Pt and for H_2 measurement porous Pt

Figures 3-25, 3-26, 3-25 and 3-28 show the correlation of faradaic currents with electrolyte flow rates not in the potential region of diffusion limitation, but at lower overpotentials, i.e. $E_1=0.65$ V for Fe^{3+} measurement and $E_1=0.8$ V for HQ measurement.

Logarithmic plots (Figure 3-26) show that faradaic current for upper compartment (I_{F1}) at $E_1=0.65$ V is proportional to $u^{0.28}$ and the faradaic current of the lower compartment (I_{F2}) at $E_1=0.65$ V is proportional to $u^{0.33}$.

Logarithmic plots (Figure 3-28) show that faradaic current for upper compartment (I_{F1}) at $E_1=0.8$ V is proportional to $u^{0.28}$ (not completely diffusion controlled) and the faradaic current of the lower compartment (I_{F2}) at $E_1=0.8$ V is proportional to $u^{0.36}$.

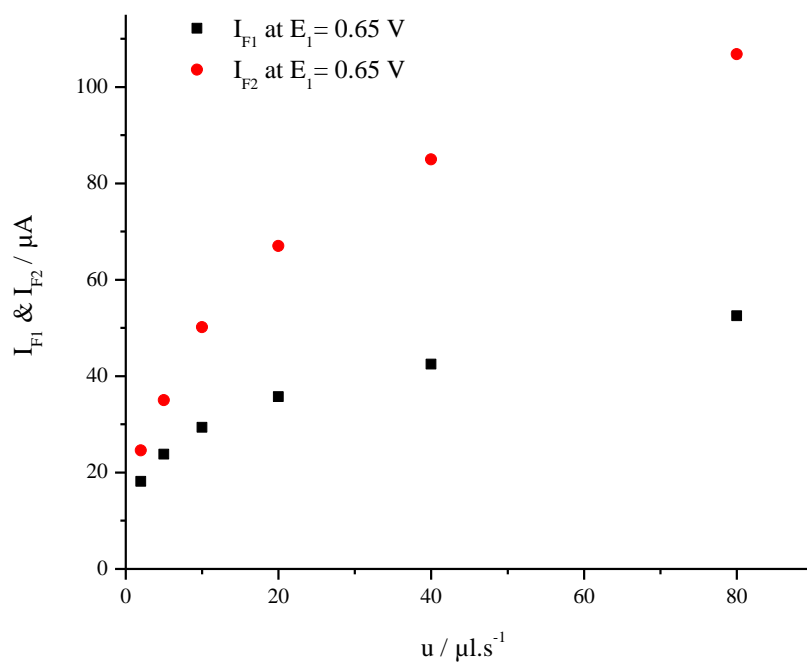


Figure 3-25 Correlation of the kinetically controlled faradaic currents of the upper and the corresponding lower working electrode (I_{F1} & I_{F2}) with flow rate for 10^{-3} M $\text{Fe}_2(\text{SO}_4)_3$ in 0.5 M H_2SO_4 measurement; at $E_1=0.65$ V and $E_2=0.5$ V (const.); sweep rate: 5 mV/s

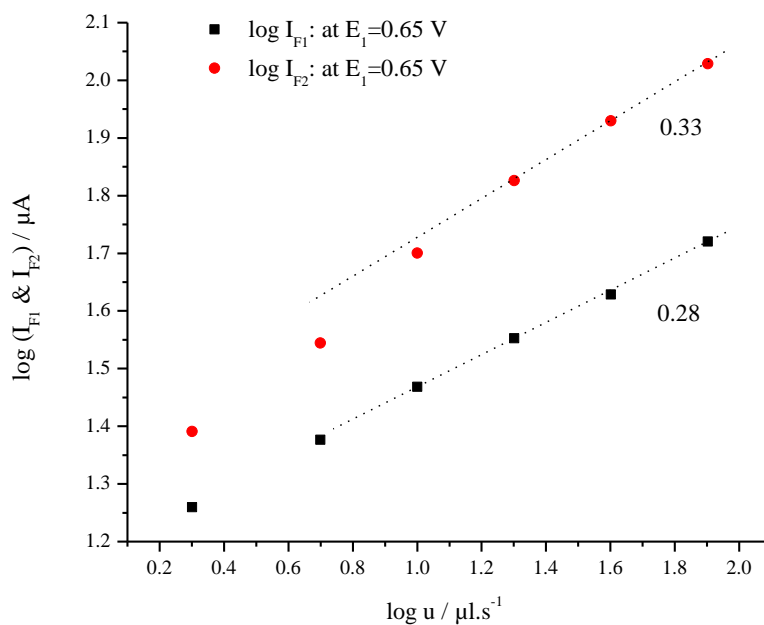


Figure 3-26 Logarithmic diagrams of faradaic currents of upper and lower working electrodes with flow rate for 10^{-3} M $\text{Fe}_2(\text{SO}_4)_3$ in 0.5 M H_2SO_4 measurement; at $E_1=0.65$ V and $E_2=0.5$ V (const.); sweep rate: 5 mV/s

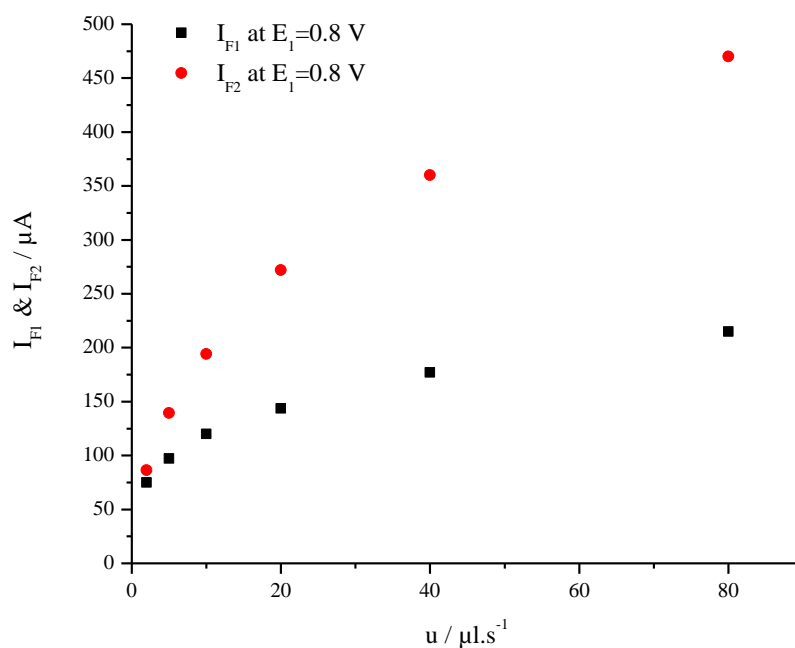


Figure 3-27 Correlation of faradaic currents of upper and lower working electrodes (I_{F1} & I_{F2}) with flow rate for 10^{-3} M hydroquinone in 0.5 M H_2SO_4 measurement; at $E_1=0.8$ V and $E_2=1.0$ V (const.); sweep rate: 5 mV/s

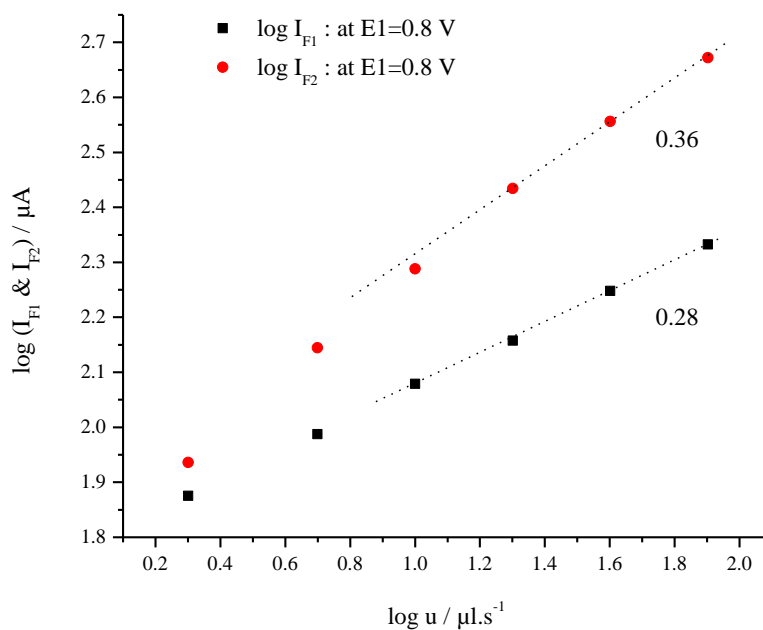


Figure 3-28 Logarithmic diagrams of faradaic currents of upper and lower working electrodes with flow rate for 10^{-3} M hydroquinone in 0.5 M H_2SO_4 measurement; at $E_1=0.8$ V and $E_2=1.0$ V (const.); sweep rate: 5 mV/s

3.6 Correlation of collection efficiency and flow rate

The collection efficiencies for the upper and the lower compartment at different flow rates of electrolyte are calculated through dividing the amount of species reacting on the upper or lower working electrode by the amount of species entering the cell. Figures 3-29 and 3-31 show the dependency of the collection efficiency on the electrolyte flow rate for the upper and lower working electrode, respectively. A hyperbolic decay appears while increasing the flow rate. The highest value for collection efficiency happens in the lowest electrolyte flow rate.

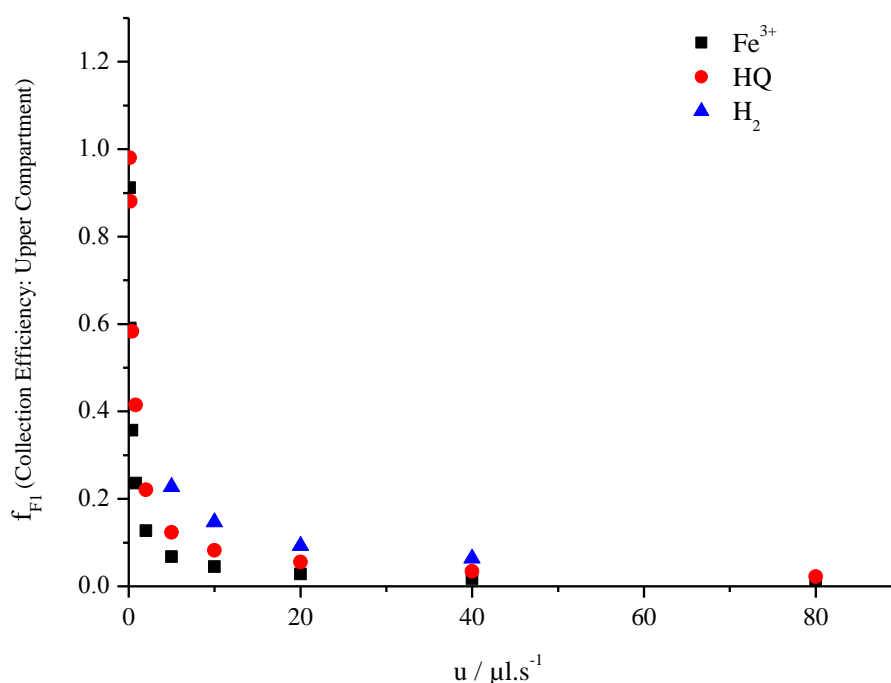


Figure 3-29 Collection efficiency of the upper electrode depending on the flow rate for 10^{-3} M hydroquinone in 0.5 M H_2SO_4 , 10^{-3} M $\text{Fe}_2(\text{SO}_4)_3$ in 0.5 M H_2SO_4 and H_2 saturated 0.5 M H_2SO_4 measurements; sweep rate: 5 mV/s

As seen in eq. 3-1, $f_{\text{F1}} \propto I_{\text{F1}}/u$ and from eq. 3-12, $I_{\text{F1}} \propto u^{1/3}$; thus, the theoretical behavior for high u is: $f_{\text{F1}} \propto u^{1/3}/u = u^{-2/3}$. Figure 3-30 shows a linear correlation of the collection efficiency of the upper working electrode with $u^{-2/3}$ at high flow rates. Interestingly, the data for high flow rates fit the straight line through the origin.

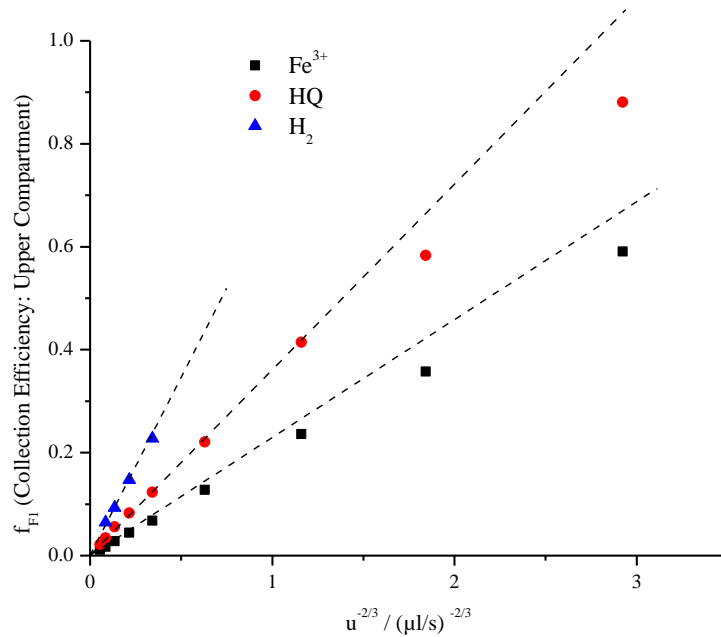


Figure 3-30 Collection efficiency of the upper electrode depending on $u^{-2/3}$ for 10^{-3} M hydroquinone in 0.5 M H_2SO_4 , 10^{-3} M $\text{Fe}_2(\text{SO}_4)_3$ in 0.5 M H_2SO_4 and H_2 saturated 0.5 M H_2SO_4 measurements; sweep rate: 5 mV/s

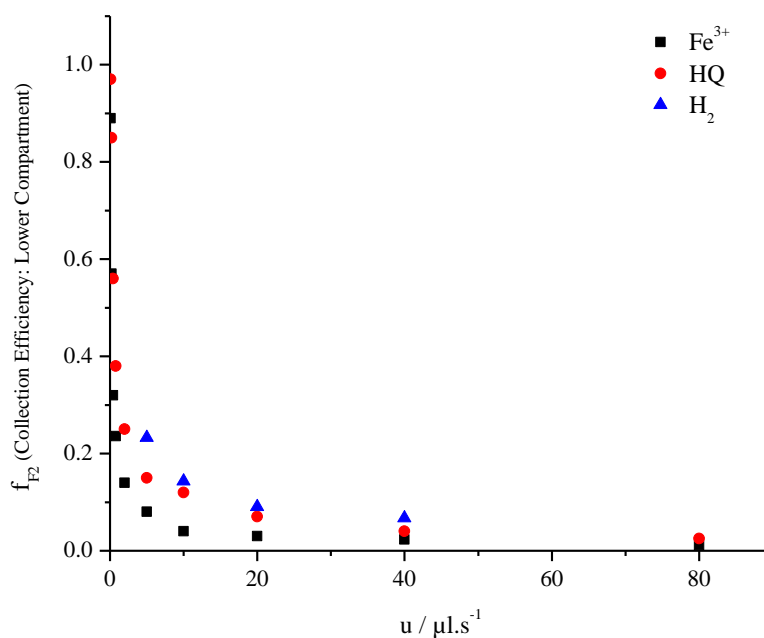


Figure 3-31 Collection efficiency of the lower electrode depending on the flow rate for 10^{-3} M hydroquinone in 0.5 M H_2SO_4 , 10^{-3} M $\text{Fe}_2(\text{SO}_4)_3$ in 0.5 M H_2SO_4 and H_2 saturated 0.5 M H_2SO_4 measurements; sweep rate: 5 mV/s

3.7 Correlation of transfer efficiency and flow rate

The transfer efficiencies N for hydroquinone measurements are all calculated from the limiting current values of the measurements ($E_1=1.0$ V) with a constant potential of $E_2 = 0.5$ V (const.) on the lower electrode, i.e. the formed quinone on the upper electrode was reduced back to hydroquinone on the lower electrode (Figure 3-2 : $\frac{I_{F2}^P}{I_{F1}}$); in case of $\text{Fe}^{2+} / \text{Fe}^{3+}$

measurements the values for transfer efficiency are calculated from the spectra ($E_1=0.5$ V) with a constant potential of $E_2 = 1.0$ V (const.) on the lower electrode, that means Fe^{3+} is reduced on the upper electrode and the formed Fe^{2+} is oxidized back on the lower electrode (Figure 3-6 : $\frac{I_{F2}^P}{I_{F1}}$).

For hydrogen measurements, the transfer efficiencies are calculated from the measurements with the potential of the upper electrode sweeping and a constant potential of $E_2 = 0.4$ V (const.) applied to the lower electrode, so on the lower electrode the oxidation of hydrogen takes place (Figure 3-10 : $\frac{I_{F2}^P}{I_{F1}} = \frac{\Delta I_{F2}}{I_{F1}}$).

A comparison of the different transfer efficiencies in dependence on the flow rate is shown in Figure 3-32. The values show an exponential decay of the transfer efficiency with the increasing flow rate, which can be explained by the fact that a higher flow rate means a lower time for the electrolyte to adsorb on the surface and thus a lower amount of molecules that can react back. The maximum value is reached at the lowest flow rates.

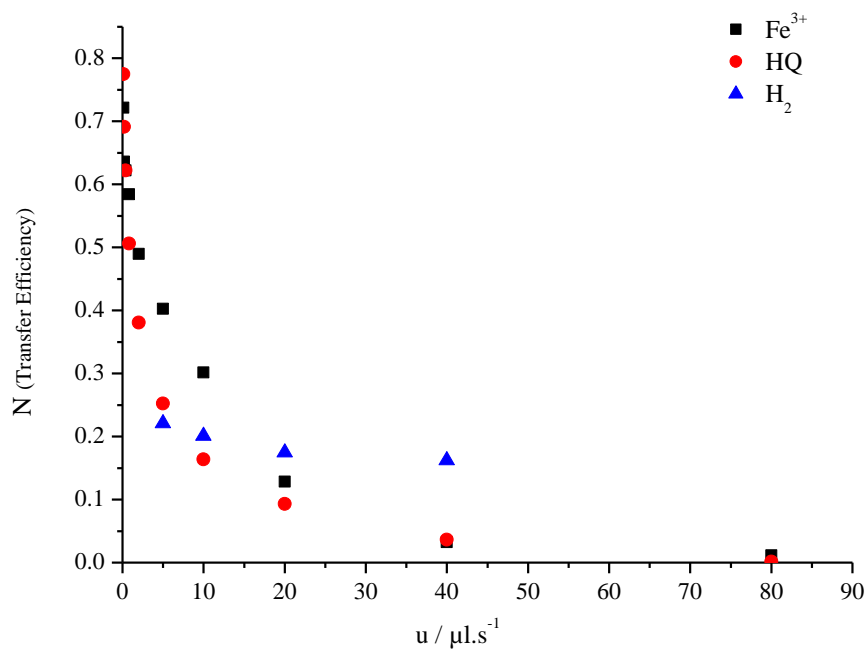


Figure 3-32 Transfer efficiencies depending on the flow rate for 10^{-3} M hydroquinone in 0.5 M H_2SO_4 , 10^{-3} M $\text{Fe}_2(\text{SO}_4)_3$ in 0.5 M H_2SO_4 and H_2 saturated 0.5 M H_2SO_4 measurements; sweep rate: 5 mV/s

Figure 3-33 represents the comparison of the collection efficiency of the lower compartment (f_2) and transfer efficiency (N) versus electrolyte flow rate. For Fe^{3+} measurement, at very low flow rate, the collection efficiency of the lower compartment is higher than transfer efficiency and at higher flow rates, the transfer efficiency will be higher. For HQ measurement, at low flow rate, the transfer efficiency is lower and at high flow rates, it is slightly higher than collection efficiency. For dissolved H_2 measurement, the transfer efficiency is slightly higher than collection efficiency of the lower compartment.

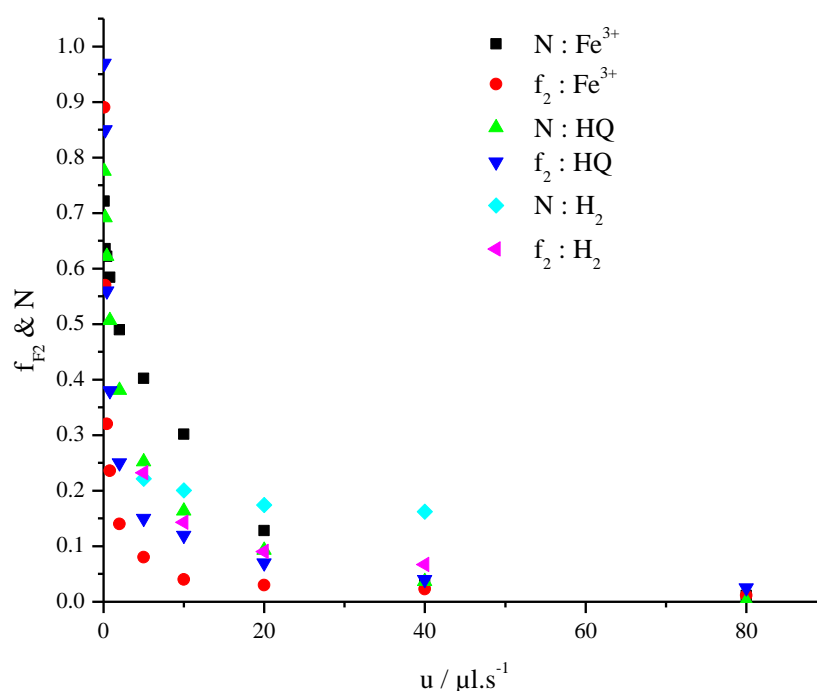


Figure 3-33 Comparison of collection efficiency of the lower compartment and transfer efficiency versus electrolyte flow rate for 10^{-3} M hydroquinone in 0.5 M H_2SO_4 , 10^{-3} M $\text{Fe}_2(\text{SO}_4)_3$ in 0.5 M H_2SO_4 and H_2 saturated 0.5 M H_2SO_4 measurements; sweep rate: 5 mV/s

Figure 3-34 shows the correlation of transfer efficiency divided by collection efficiency of the lower compartment (N/f_{F2}) with electrolyte flow rate. What we expect is that the value of N/f_{F2} must be 1 for low flow rates of electrolyte because of complete mixing and for higher u this value is higher than 1 due to incomplete mixing of species. But for unknown reason, in Fe^{3+} and HQ measurements, for flow rates higher than $10 \mu\text{l.s}^{-1}$, N/f_{F2} starts decreasing.

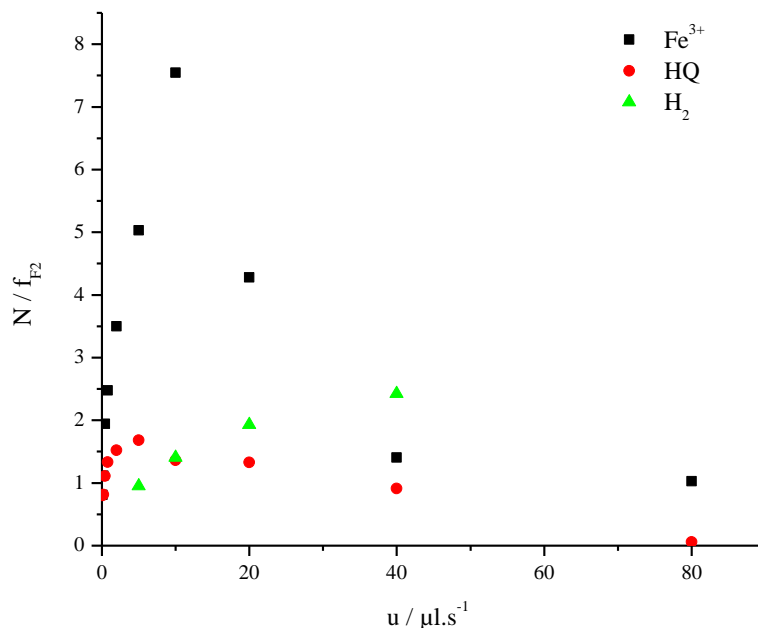


Figure 3-34 Correlation of transfer efficiency divided by collection efficiency of the lower compartment (N/f_{F_2}) with electrolyte flow rate for 10^{-3} M hydroquinone in 0.5 M H_2SO_4 , 10^{-3} M $\text{Fe}_2(\text{SO}_4)_3$ in 0.5 M H_2SO_4 and H_2 saturated 0.5 M H_2SO_4 measurements; sweep rate: 5 mV/s

As seen in Figure 3-34, because of high diffusion coefficient of H_2 , we have complete mixing at $5 \mu\text{l.s}^{-1}$ while due to lower diffusion coefficient of HQ and Fe^{3+} mixing is mostly incomplete at the same flow rate.

Figures 3-35 and 3-36 show the correlation of transfer efficiencies with electrolyte flow rates for Fe^{3+} and HQ measurements not in the potential region of diffusion limitation, but at lower overpotentials, e.g. for 0.6 V, 0.65 V and 0.7 V (for Fe^{3+}), and 0.7 V, 0.75 V and 0.8 V (for HQ measurements).

The transfer efficiencies are not considered for low flow rates because of high time residence of the species which leads to the large hysteresis.

The values show an exponential decay of the transfer efficiency with the increasing flow rate. The maximum value is reached at the lowest flow rates.

As seen in Figure 3-35, the transfer efficiency for Fe^{3+} is independent of potentials and from Figure 3-36 we find the dependency of transfer efficiency on the potentials in HQ measurement.

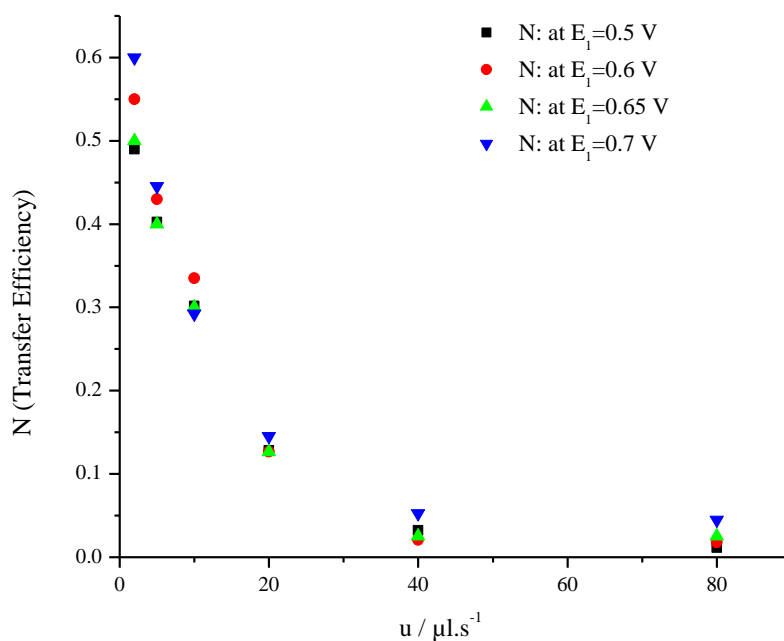


Figure 3-35 Transfer efficiencies depending on the flow rate for 10^{-3} $\text{Fe}_2(\text{SO}_4)_3$ in 0.5 M H_2SO_4 measurement at 0.5 V, 0.6 V, 0.65 V and 0.7 V; $E_2=1.0$ V (const.); sweep rate: 5 mV/s

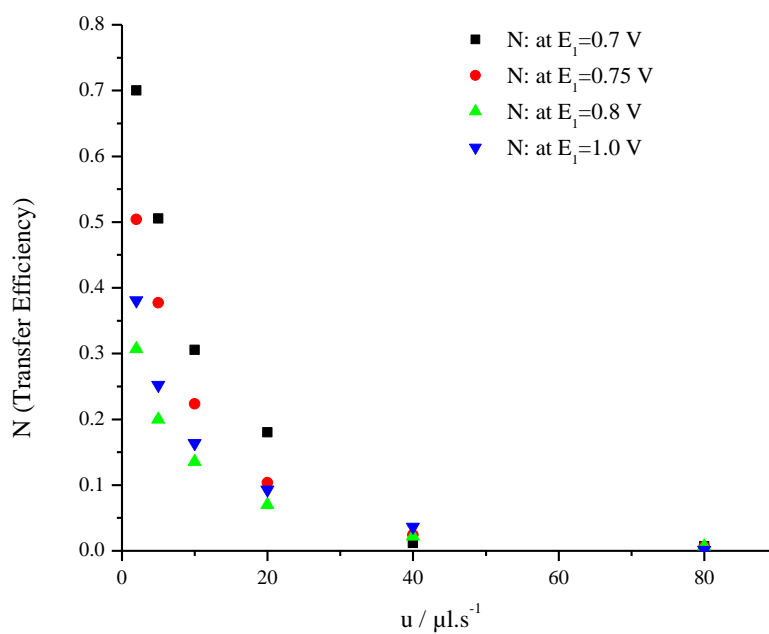


Figure 3-36 Transfer efficiencies depending on the flow rate for 10^{-3} M hydroquinone in 0.5 M H_2SO_4 measurement at 0.7 V, 0.75 V, 0.8 V and 1.0 V; $E_2=0.5$ V (const.); sweep rate: 5 mV/s

3.8 Correlation of shielding factor and flow rate

The shielding factors for hydroquinone measurements are all calculated using I_{F2} at $E_1=0.5$ V for the upper working electrode and a constant potential of $E_2=1.0$ V (const.) on the lower electrode (Figure 3-2 : $\frac{I_{F2}}{I_{F2}^0}$). On both electrodes, the oxidation of hydroquinone to quinone takes place. The current of the lower electrode is lower than the current of the upper electrode, since the concentration of hydroquinone is lower on the lower electrode than on the upper electrode.

The calculation of shielding factors for the Fe^{2+} / Fe^{3+} measurement is done using I_{F2} at $E_1=1.0$ V on the upper working electrode and a constant potential of $E_2 = 0.5$ V (const.) on the lower electrode so the same electrochemical reaction takes place on both electrodes (Figure 3-6 : $\frac{I_{F2}}{I_{F2}^0}$).

For Hydrogen measurements since no hydrogen was evolved in solution, an open circuit measurement for the shielding factors was necessary. Two different measurements were done for this: the first one with a cyclic potential applied to both electrodes (Figure 3-13 : I_{F2}) and the second one with a cyclic potential applied to the second electrode and the first electrode disconnected (open circuit) (Figure 3-12 : I_{F2}^0). In the case of both electrodes having a cyclic potential, the oxidation of hydrogen takes place on both electrode surfaces (at $E_1=0.45$ V and $E_2=0.45$ V). In the open circuit measurement, the second electrode is the only reaction area and the current flow through the second electrode should be at maximum ($E_2=0.45$ V). Dividing the limiting current of the lower working electrode at open circuit measurement through the limiting current of the upper working electrode at both electrodes cycling measurement gives the shielding factors S.

The calculated shielding factor in dependence on the flow rate is shown in Figure 3-37. An root-like increase in shielding factor is visible with the highest value at the highest flow rate.

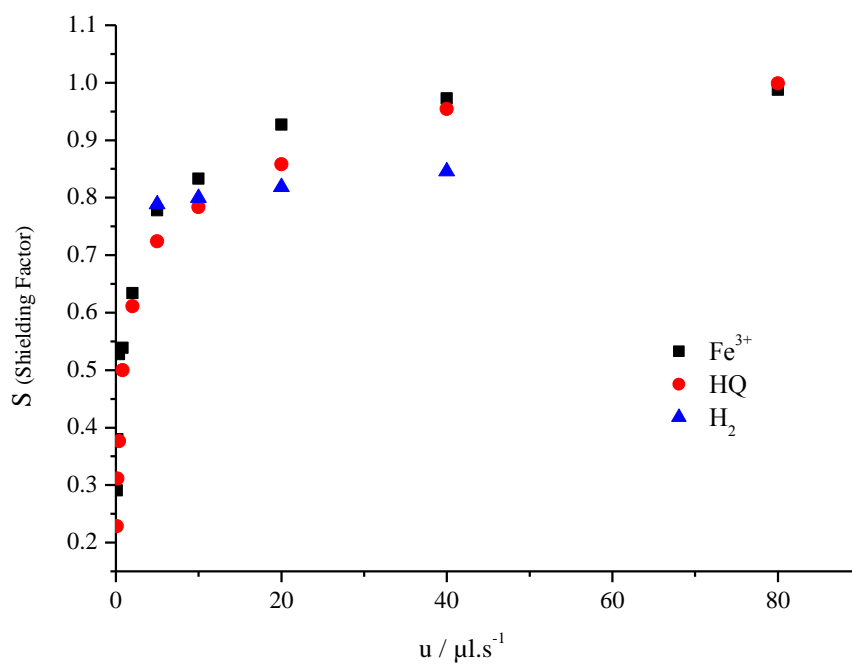


Figure 3-37 Correlation of shielding factors with electrolyte flow rate for 10^{-3} M hydroquinone in 0.5 M H_2SO_4 , 10^{-3} M $\text{Fe}_2(\text{SO}_4)_3$ in 0.5 M H_2SO_4 and H_2 saturated 0.5 M H_2SO_4 measurements; sweep rate: 5 mV/s

The behavior is as expected from eq. 3-11 and Figure 3-32; for similar collection efficiencies of the two working electrodes, $I_{F1} \approx I_{F2}^0$ and then $S \approx I-N$.

3.9 Effect of thin layer thickness

The number of Teflon-spacers used for both upper and lower compartments is important due to the effect on local electrolyte velocity.

The cyclic voltammograms of 10^{-3} M hydroquinone solution in 0.5 M sulphuric acid are shown in Figure 3-38 with flow rate of $u = 2 \mu\text{l}\cdot\text{s}^{-1}$ and where the cycling potential of $E_1 = 0.45 - 1.05$ V is applied to the upper working electrode (solid platinum) and a constant potential of $E_2 = 1.0$ V (const.) is applied to the lower working electrode (sputtered Teflon membrane).

In this experiment, the number of spacers is varied in both upper and lower compartment as following: 2, 4, 10; each Teflon spacer has an inner diameter of 6 mm and thickness of 65 μm . Due to the compressibility of Teflon spacers this thickness might be changed.

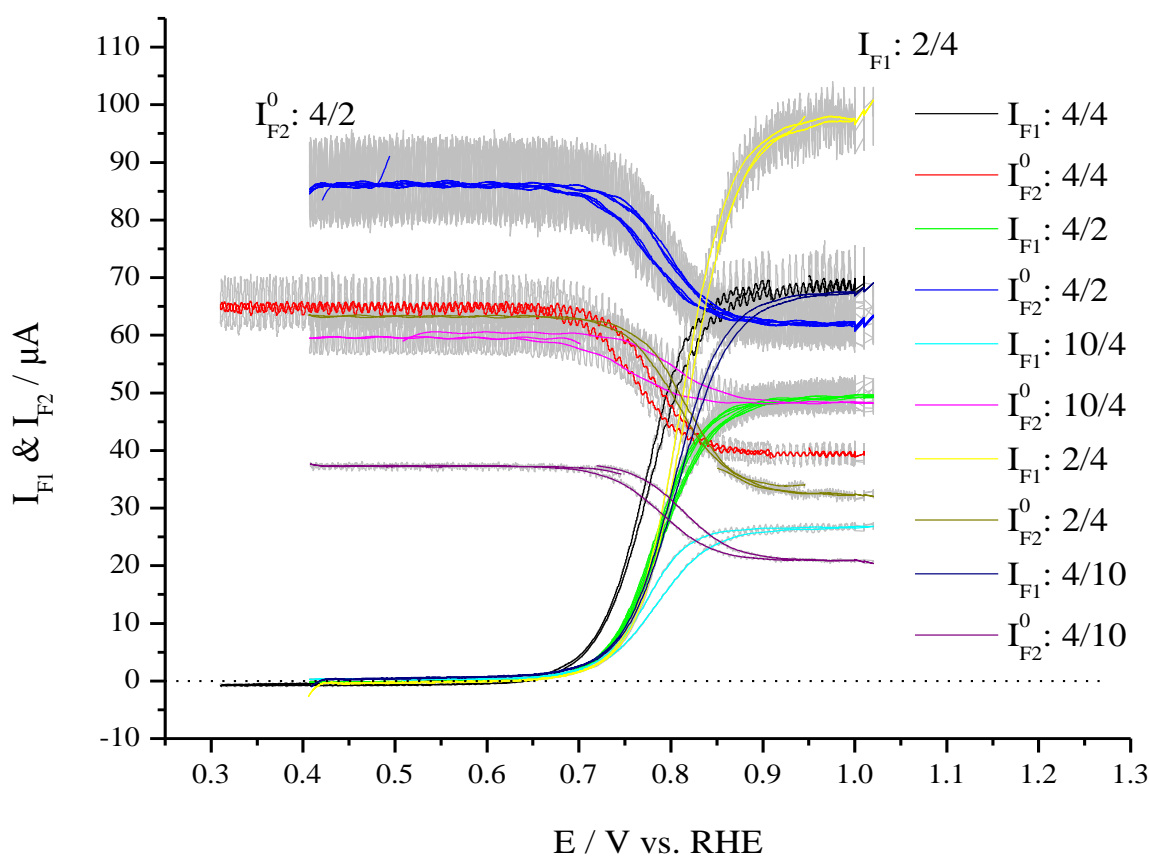


Figure 3-38 10^{-3} M hydroquinone in 0.5 M H_2SO_4 ; Sweep rate: 5 mV/s; $E_1 = 0.4 - 1.1$ V (solid Pt), $E_2 = 1.0$ V (const.) (porous Pt electrode); Electrolyte flow rates: $2 \mu\text{l}\cdot\text{s}^{-1}$; Number of spacers: 2, 4 and 10

Shielding factors (S) are calculated for 4 spacers in the upper compartment and different number of spacers in the lower compartment with electrolyte flow rate of $2\mu\text{l.s}^{-1}$. The values of 0.72, 0.60 and 0.56 are obtained for 2, 4 and 10 spacers, respectively (Figure 3-38). It shows that increasing the number of spacers leads to decrease of shielding factor (S).

Figure 3-39 represents the linear correlation between the limiting currents of upper and lower working electrodes and cubic root of electrolyte flow rates ($u^{1/3}$) for 2, 10 and 40 $\mu\text{l.s}^{-1}$ and varying the number of Teflon spacers in both upper and lower compartments.

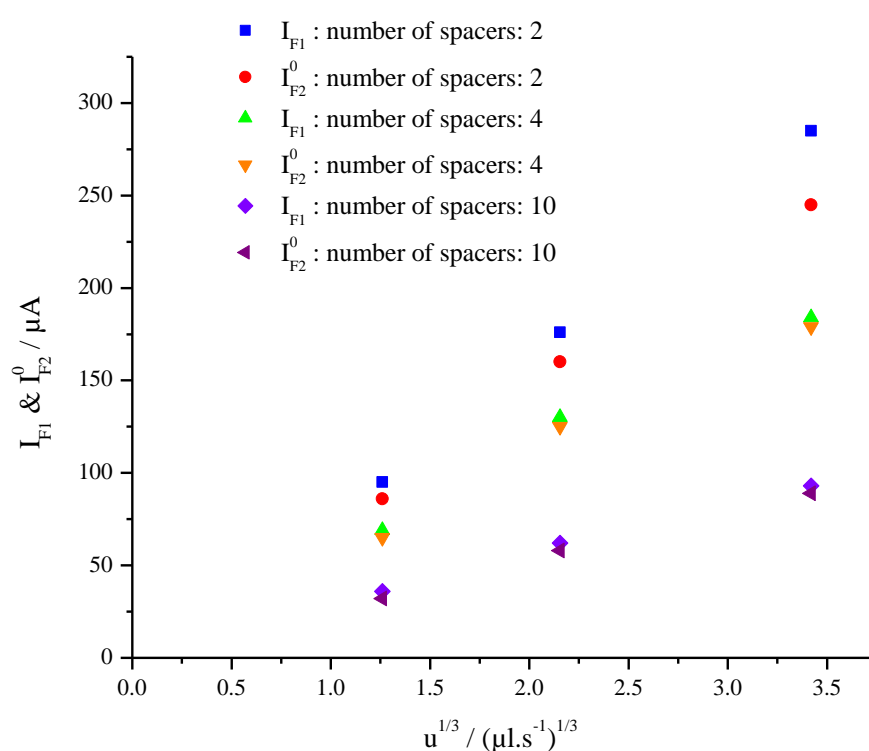


Figure 3-39 Correlation of diffusion limited current of the upper and lower working electrodes with cubic root of electrolyte flow rate ($u^{1/3}$) for 10^{-3} M hydroquinone in 0.5 M H_2SO_4 ; sweep rate: 5 mV/s; $E_1 = 0.4 - 1.1$ V (solid Pt), $E_2 = 1.0$ V (const.) (porous Pt electrode); Electrolyte flow rates: 2, 10 and $40\mu\text{l.s}^{-1}$; Number of spacers: 2, 4 and 10

Figure 3-40 shows the relationship between the diffusion limited faradaic currents of both upper and lower working electrodes and the normalized flow rate which is obtained by dividing the flow rate by reaction volume (u/V) which is proportional to the average electrolyte velocity in the cell. Decreasing the number of spacers (decrease of reaction volume) means increase of normalized flow rate; thus, as shown, causes the increase of both diffusion limited current of upper and lower compartments.

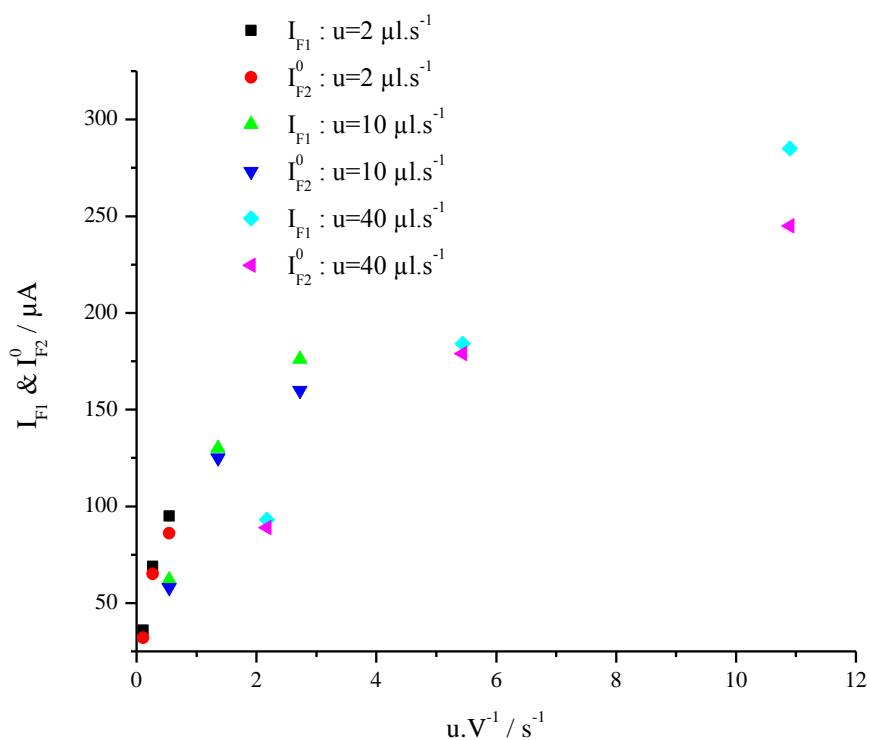


Figure 3-40 Relation between diffusion limited faradaic currents and normalized flow rates ($u.V^{-1}$); $10^{-3} \text{ M C}_6\text{H}_6\text{O}_2 + 0.5\text{M H}_2\text{SO}_4$; sweep rate: 5 mV s^{-1} ; $E_1 = 0.4 - 1.1 \text{ V}$ (solid Pt), $E_2 = 1.0 \text{ V}$ (const.) (porous Pt electrode); Electrolyte flow rates: 2, 10 and $40 \mu\text{l.s}^{-1}$; Number of spacers: 2, 4 and 10

Figure 3-41 shows the correlation of diffusion limited currents of upper and lower working electrodes with the cubic root of normalized flow rate $(u.V^{-1})^{1/3}$.

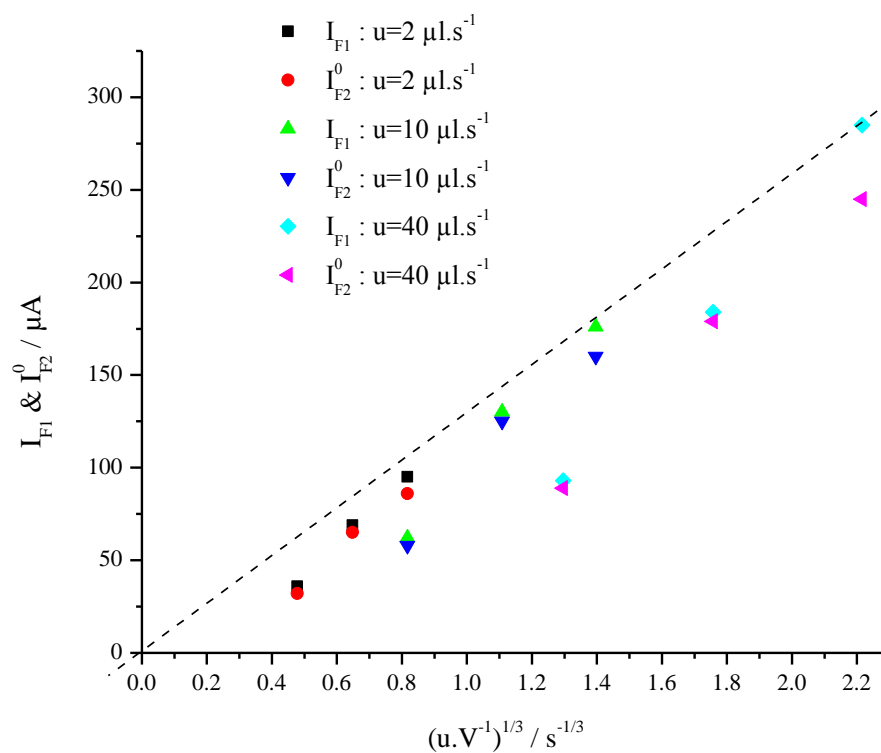


Figure 3-41 Relation between diffusion limited faradaic currents and cubic root of normalized flow rates $(u.V^{-1})^{1/3}$; $10^{-3} \text{ M C}_6\text{H}_6\text{O}_2 + 0.5 \text{ M H}_2\text{SO}_4$; sweep rate: 5 mV s^{-1} ; $E_1 = 0.4 - 1.1 \text{ V}$ (solid Pt), $E_2 = 1.0 \text{ V}$ (const.) (porous Pt electrode); Electrolyte flow rates: 2, 10 and $40 \mu\text{l.s}^{-1}$; Number of spacers: 2, 4 and 10

Interestingly, the values for high velocities (low thickness) approach a straight line through the origin.

With “laminar channel flow” behavior of the cell, the limiting current follows the eq. 3-12. Therefore, when plotting normalized currents $I_F / (zFcD^{2/3})$ versus the cubic root of the flow rate ($u^{1/3}$), the slopes give the geometry factors g for both upper and lower compartments with different number of Teflon spacers. The value $D=8.5\times 10^{-6} \text{ cm}^2.\text{s}^{-1}$ is used from sources [31, 32]. Figure 3-42 clearly shows the obtained geometry factors for varying number of Teflon spacers. As shown, increasing the number of spacers leads to decrease of geometry factor g .

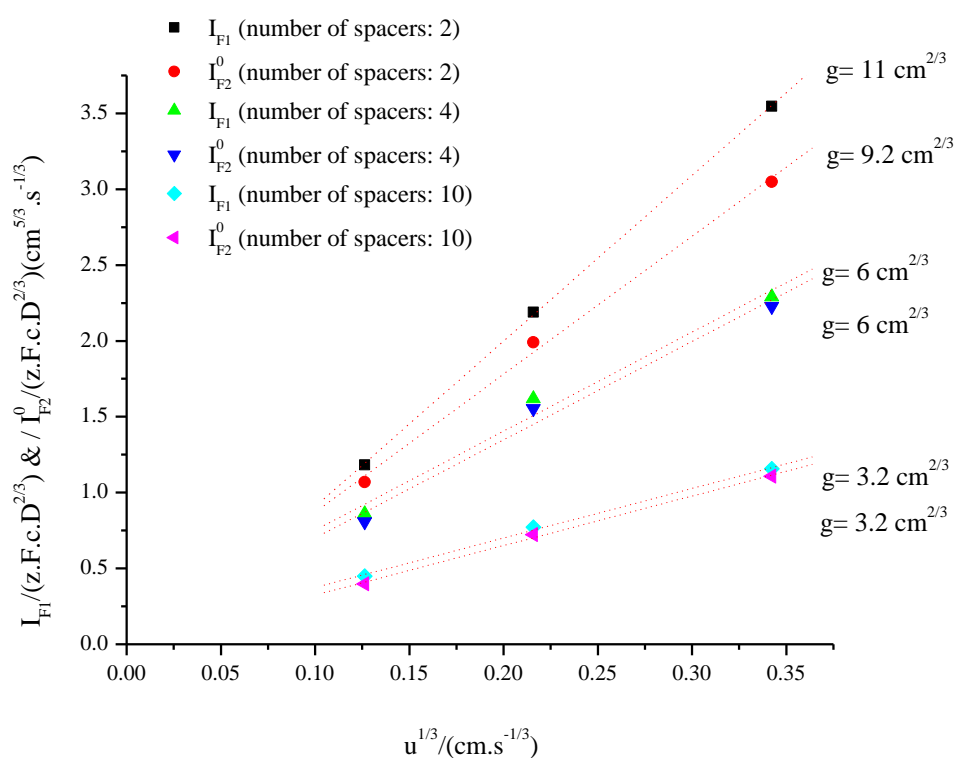


Figure 3-42 Normalized limiting currents of the upper (solid Pt) and lower (porous Pt) working electrodes vs. $u^{1/3}$, using data for D and c from [31, 32]. Slopes correspond to the geometry factor g

On the other hand, the values obtained for g confirm the correlation between g and b in eq. 1-11 ($g \propto b^{-2/3}$). Increasing b (thin layer thickness) leads to decrease of g .

3.10 ^{13}CO bulk oxidation

To determine the hydrodynamic conditions, bulk CO oxidation measurements on a polycrystalline Pt electrode are performed in a thin layer cell under continuous mass-transport of CO-saturated 0.5 M H_2SO_4 electrolyte at 7 different solution flow rates range between 0.4 - 42 $\mu\text{l}\cdot\text{s}^{-1}$ and a potential sweep rate of 5 $\text{mV}\cdot\text{s}^{-1}$. CO ($m/z=28$) has the same fragmentation of N_2 ($m/z=28$). Thus, to prevent misleading caused by this similarity, ^{13}CO ($m/z=29$) is used in this measurement.

Figure 3-43 shows an example of the cyclic voltammogram for 10 $\mu\text{l}\cdot\text{s}^{-1}$ flow rate.

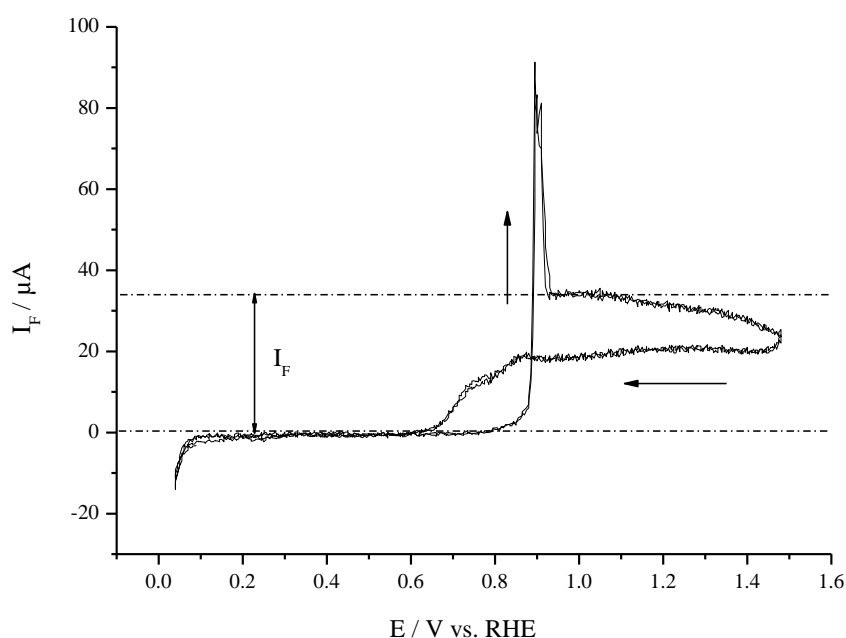


Figure 3-43 Cyclic voltammogram of oxidation of dissolved CO on polycrystalline platinum at 10 $\mu\text{l}/\text{s}$ flow rate; ^{13}CO -saturated 0.5 M sulfuric acid; Sweep rate 5 $\text{mV}\cdot\text{s}^{-1}$

All characteristic features for polycrystalline Pt electrode are fully suppressed in presence of CO up to 0.7 V in the positive-going potential scan due to a surface blocking by adsorbed CO, which is oxidized at potentials positive of 0.85 V, resulting in a sharp current peak. Within the potential scan to more positive values, the CO bulk oxidation current decreases due to the increase of PtO thickness, and stabilizes at ca. 20 μA in the negative-going scan. With PtO reduction negative of 0.8 V in the negative-going potential scan, the bulk CO oxidation current goes down to zero at ca. 0.6 V.

Figure 3-44 shows the corresponding mass spectrometric cyclic voltammogram for 10 $\mu\text{l/s}$ flow rate during bulk CO oxidation.

It shows no distinct features in the positive-going potential scan up to ca. 0.85 V, where a sharp mass increase peak resembles the corresponding current peak for CO_{ad} oxidation.

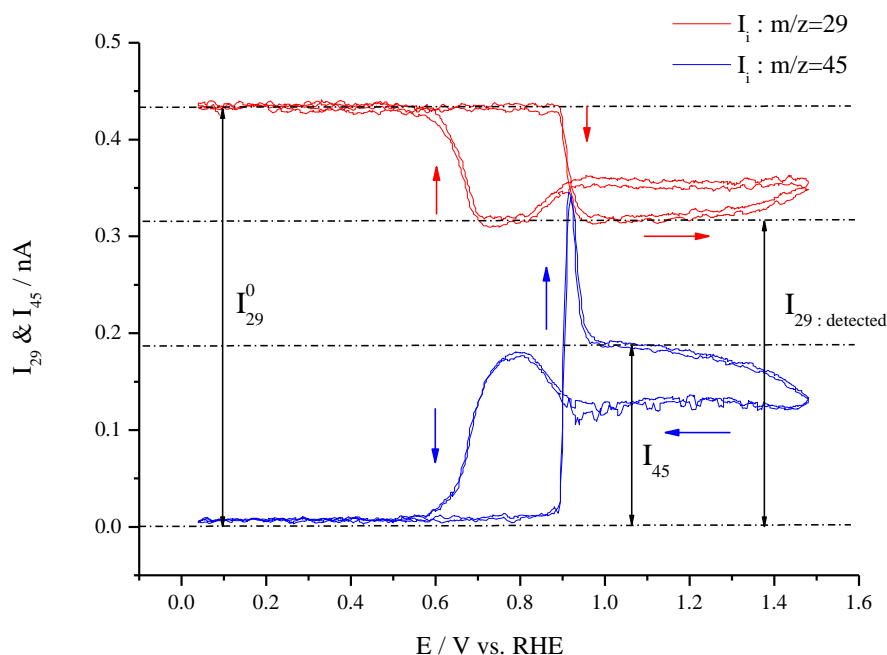


Figure 3-44 Mass spectrometric cyclic voltammogram of oxidation of dissolved CO on polycrystalline platinum at 10 $\mu\text{l/s}$ flow rate; ^{13}CO -saturated 0.5 M sulfuric acid; sweep rate 5 $\text{mV}\cdot\text{s}^{-1}$

The electrode mass change rate in the CO-saturated electrolyte shows a distinct decrease peak in the negative-going potential scan centered at the potential ca. 0.7 V (Figure 3-44 - blue curve: $m/z=45$), corresponding to PtO reduction, which is retarding further bulk CO oxidation followed by readsorption of CO (Figure 3-43).

In the further negative-going potential scan, the mass change rate (Figure 3-44) and the CV (Figure 3-43) are nearly featureless in CO-saturated solution.

Due to fragmentation of the evolved CO_2 , the result obtained using the Mass Spectrometry (Figure 3-45), the mass-to-charge ratio $m/z=28$ of CO overlaps with the same fragment formed during ionization of CO_2 . For CO the abundance of $m/z=28$ signal amounts to 100. According to the mass scan recorded for CO_2 -saturated 0.5 M H_2SO_4 , the relative ionic current of $m/z=44$ and $m/z=28$ signals in the mass spectrum of CO_2 are $8.9 \cdot 10^{-8}$ and $8.6 \cdot 10^{-9}$,

respectively. The interpretation of the $m/z=28$ signal for mixtures of CO and CO₂ can be thus misleading if the contribution of the CO₂ fragments is not taken into account.

Quantifying fragmentation of saturated CO₂ allows the determination of the ratio between $m/z=28$ and 44 ionic currents which gives the contribution of ca. 0.1 (ratio in NIST). It thus can be used for the correction of the intensity of ¹³CO ($m/z=29$) due to ¹³CO₂ ($m/z=45$) fragmentation and the real ionic current for $m/z=29$ will be calculated through eq. 3-13.

$$(3-13) \quad I_{29\text{-real}}(\text{at } 1.1 \text{ V}) = I_{29\text{-detected}}(\text{at } 1.1 \text{ V}) + [\% \text{contribution} \times I_{45}(\text{at } 1.1 \text{ V})]$$

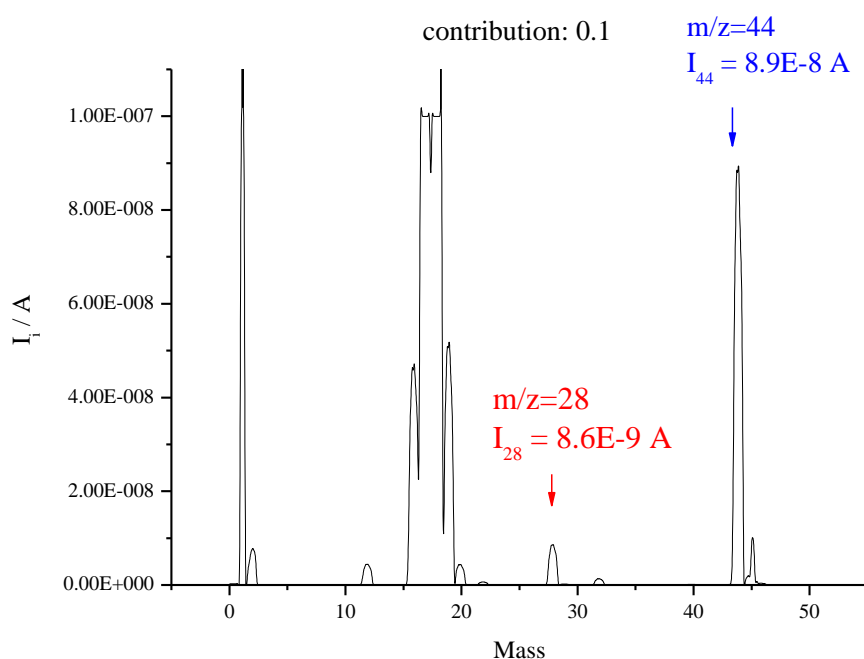


Figure 3-45 Mass scan (0-50); CO₂-saturated H₂SO₄ ; flow rate 5 $\mu\text{l/s}$; scan speed 10 s/u; time constant 0.25 s

Figures 3-46 and 3-48 show the relationship between diffusion limited faradaic (I_F) and the ion ($I_{29\text{-real}}$ & I_{45}) currents and the flow rates for the bulk oxidation of ^{13}CO -saturated 0.5 M H_2SO_4 . Parabolic dependency is obtained for the dependence of the current at the potential just after the peak (at about 0.95 V).

Logarithmic plots (Figures 3-47 and 3-49) show that faradaic current I_F is proportional to $u^{0.30}$ and the ion current (I_{29} and I_{45}) are proportional to $u^{0.39}$ and $u^{0.20}$ respectively.

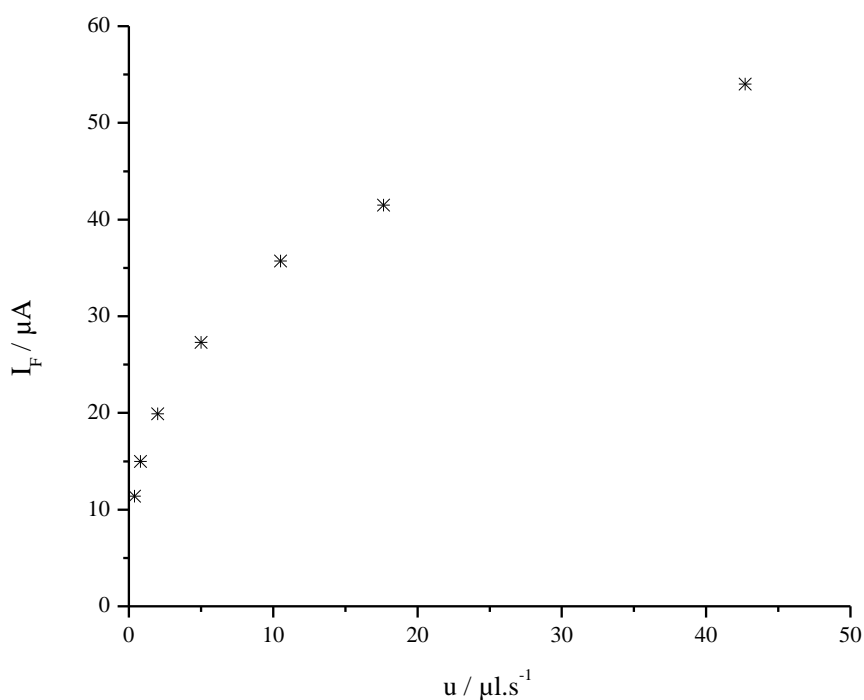


Figure 3-46 Flow rate dependence of the faradaic current for ^{13}CO -saturated 0.5 M H_2SO_4 ;
Sweep rate: 5 mV.s^{-1}

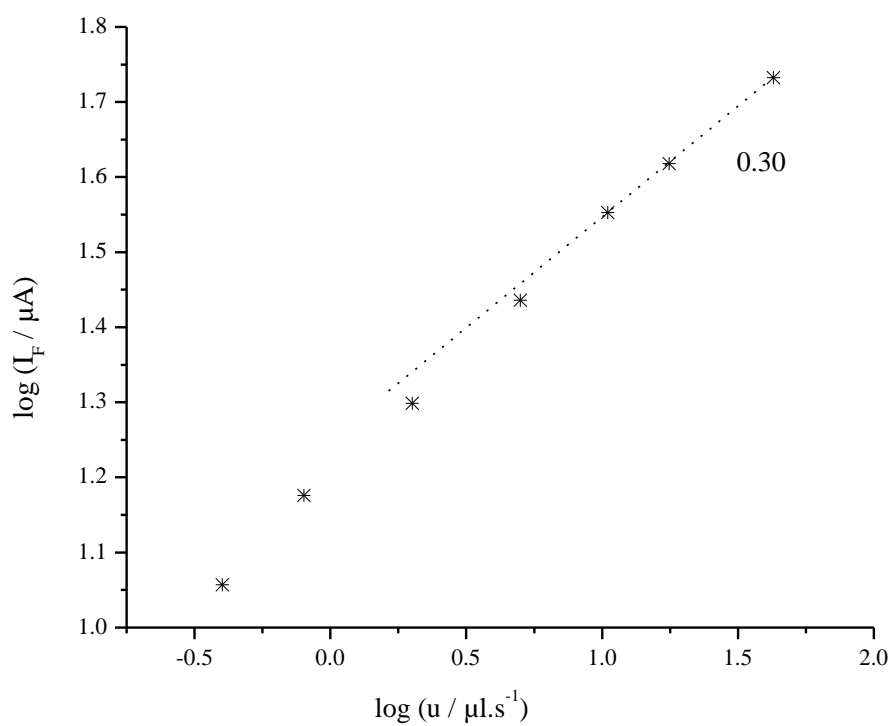


Figure 3-47 Logarithmic diagram of limiting faradaic current with flow rate for ^{13}CO -saturated 0.5 M H_2SO_4 ; sweep rate: $5 \text{ mV}\cdot\text{s}^{-1}$

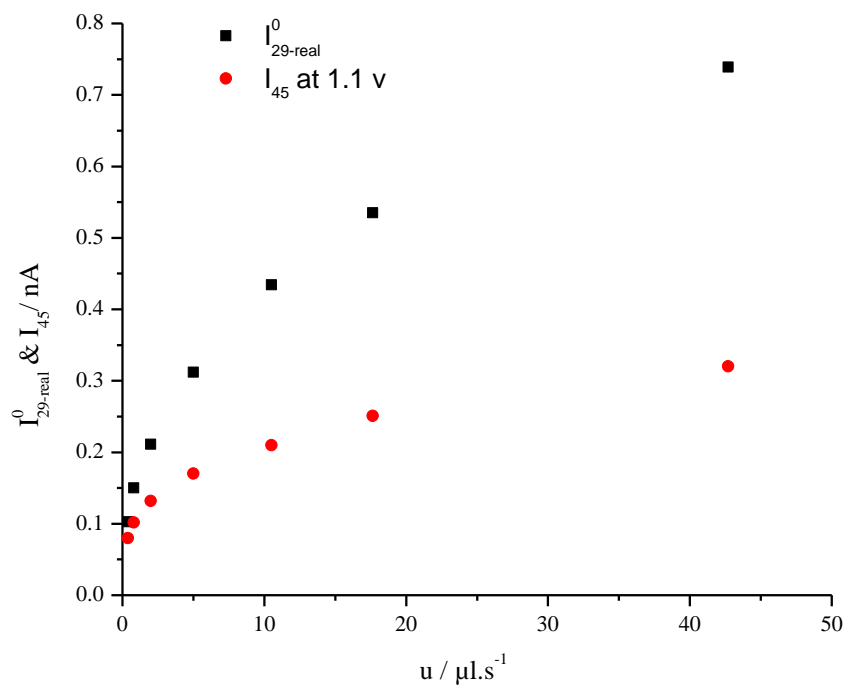


Figure 3-48 Flow rate dependence of the ion currents ($m/z=29$ & 45) for ^{13}CO -saturated $0.5 \text{ M H}_2\text{SO}_4$ ($m/z=29$)

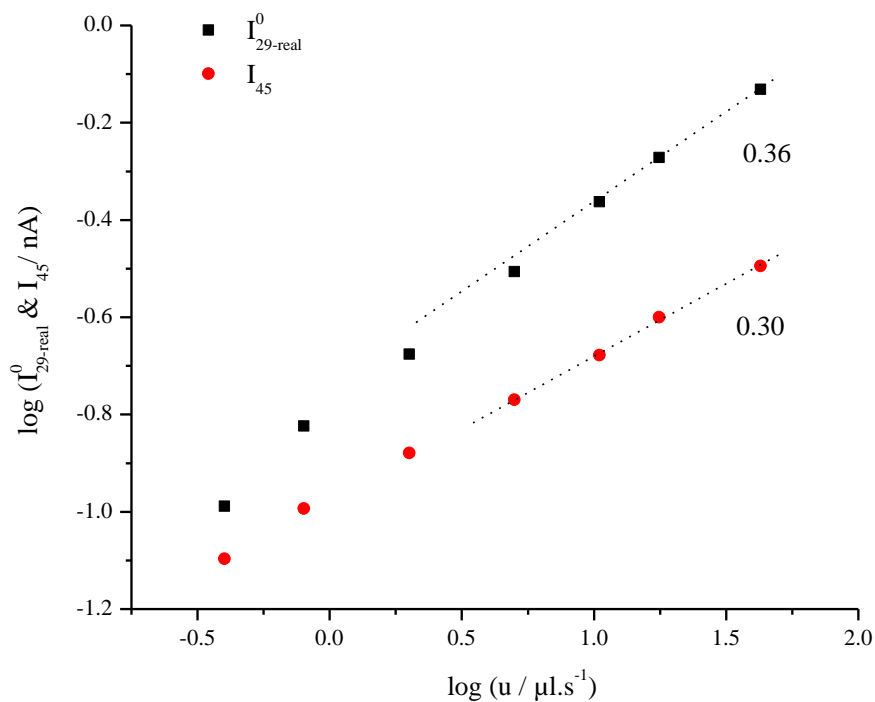


Figure 3-49 Log-log plot of the ion current ($m/z=29$ & 45) vs. flow rates for ^{13}CO -saturated $0.5 \text{ M H}_2\text{SO}_4$

The collection efficiencies are obtained by eq. 3-1 with I_F (at about 0.95 V) and using solubility of CO in 0.5 H_2SO_4 equals to 10^{-3} M. Figure 3-50 shows the collection efficiency of the electrochemical reaction for ^{13}CO bulk oxidation under diffusion limiting condition plotted vs. the flow rates of electrolyte. With the decrease of the flow rate the collection efficiency increases.

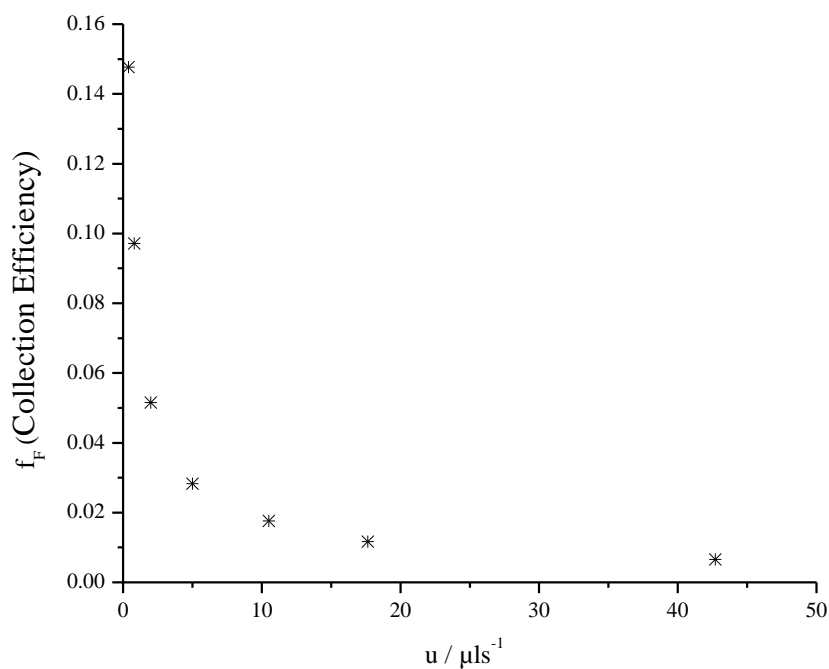


Figure 3-50 The collection efficiency of electrochemical reaction vs. flow rates of electrolyte for ^{13}CO -saturated 0.5 M H_2SO_4

3.11 Mass spectrometric characterization

To find the characteristic behavior of our cell, the ion current was detected for different substances at various flow rates in the range of $2\text{-}40\ \mu\text{l}\cdot\text{s}^{-1}$. Different electrolytes are passed through the dual thin-layer flow through cell, while the mass spectrometric current is recorded for approximately 30 seconds at each flow rate (Figure 3-51).

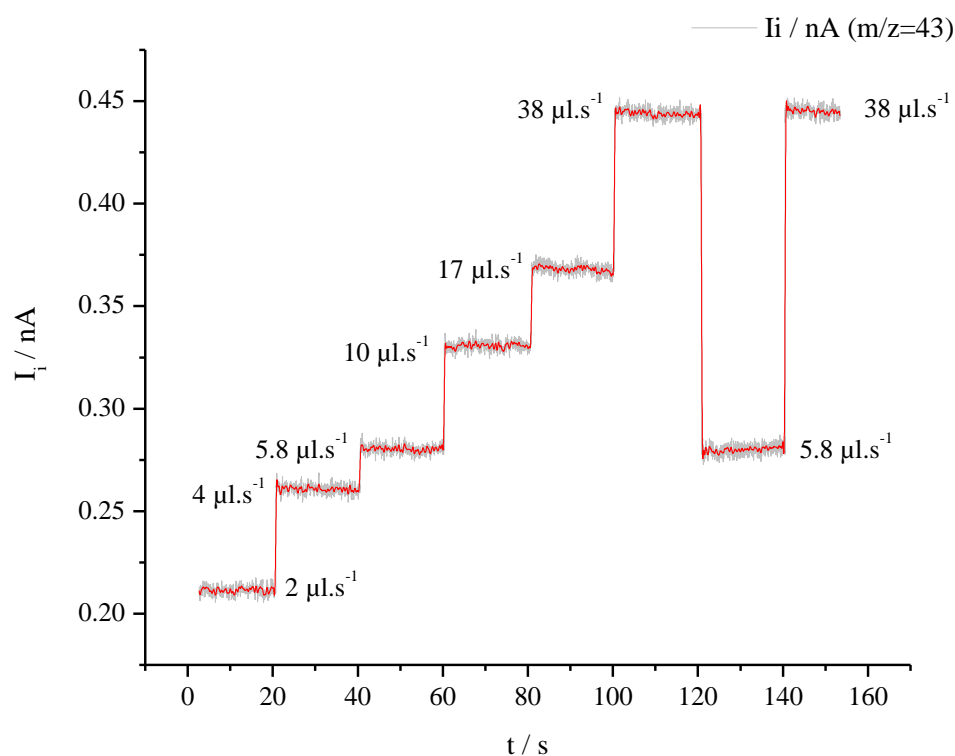


Figure 3-51 The ion current of 10^{-2} M Acetone in $0.5\ \text{M}\ \text{H}_2\text{SO}_4$ electrolyte ($m/z=43$) at various flow rates ($2\text{-}38\ \mu\text{l}\cdot\text{s}^{-1}$)

Figure 3-52 shows the correlation of the ionic current with electrolyte flow rate (u) for O_2 saturated 0.5 M H_2SO_4 ($m/z=32$); 0.1 M Methanol in 0.5 M H_2SO_4 ($m/z=31$ as largest fragment); 0.01 M Ethanol in 0.5 M H_2SO_4 ($m/z=31$ as largest fragment); 0.005 M Methylformate in 0.5 M H_2SO_4 ($m/z=31$ as largest fragment); 0.1 M Acetone mixed in 0.5 M H_2SO_4 ($m/z=43$ as the most abundant fragment).

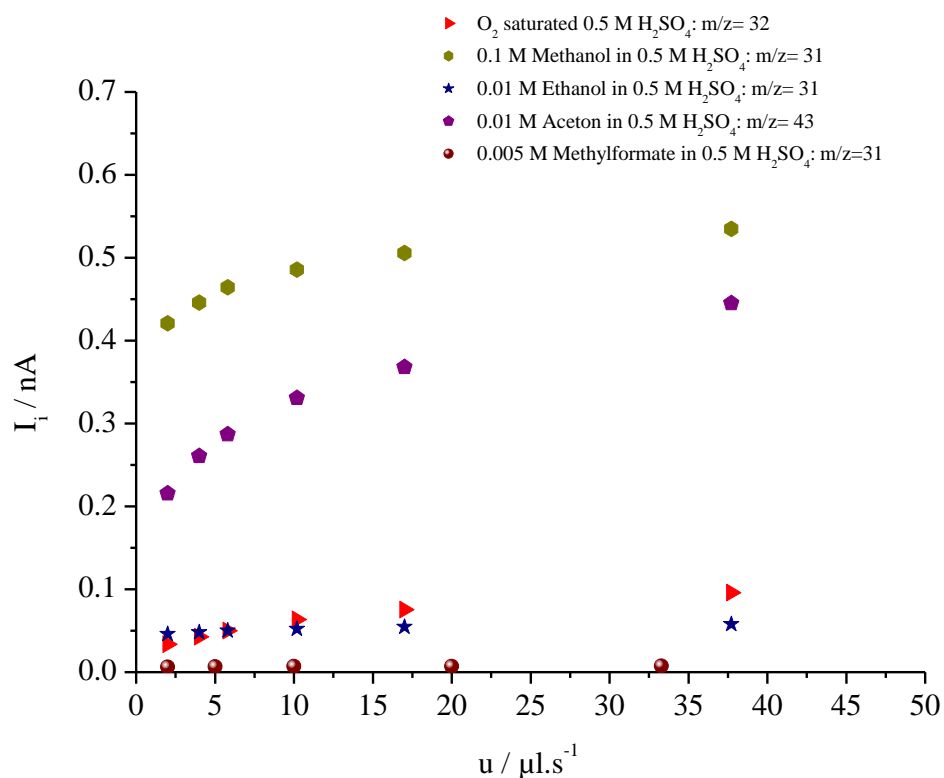


Figure 3-52 Flow rate dependence of the ion current for different electrolytes: O_2 saturated 0.5 M H_2SO_4 ($m/z=32$); 0.1 M Methanol in 0.5 M H_2SO_4 ($m/z=31$); 0.01 M Ethanol in 0.5 M H_2SO_4 ($m/z=31$); 0.005 M Methylformate in 0.5 M H_2SO_4 ($m/z=31$); 0.1 M Acetone mixed in 0.5 M H_2SO_4 ($m/z=43$)

The proportionality of the ionic current of oxygen with flow rate can be achieved by creating log-log plots (Figure 3-53).

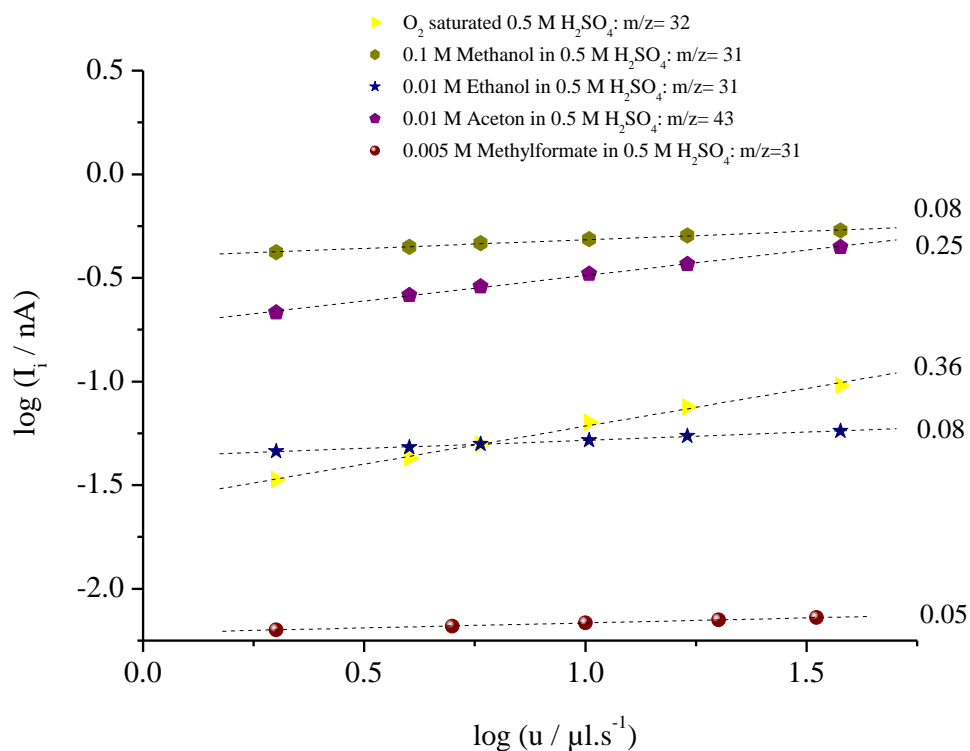


Figure 3-53 Log-log plot of the ion current vs. flow rates for different electrolytes: O₂ saturated 0.5 M H₂SO₄ (m/z=32); 0.1 M Methanol in 0.5 M H₂SO₄ (m/z=31); 0.01 M Ethanol in 0.5 M H₂SO₄ (m/z=31); 0.005 M Methylformate in 0.5 M H₂SO₄ (m/z=31); 0.1 M Acetone mixed in 0.5 M H₂SO₄ (m/z=43)

For O₂-saturated 0.5 M H₂SO₄, the proportionality of the mass spectrometric current (m/z=32) with flow rate is 0.36 which is close to the cubic root of the electrolyte flow rate ($u^{1/3}$) and for solution of acetone in 0.5 M H₂SO₄, the proportionality of ionic current (m/z=43) and flow rate is about 0.25.

The mass spectrometric current for methylformate is less dependent on electrolyte flow rate. The evaporation rate (species entering the mass spectrometer) is largely dependent on the vapor pressure of the species and thus Henry constant [28]:

$$(3-14) \quad \frac{dn}{dt} = k_p \cdot p_i^{surface}$$
$$p_i^{surface} = K_H \cdot c$$

k_p : the rate constant

K_H : Henry constant

With low vapor pressure of methylformate above the solution ($p_i^{surface}$), its diffusion is less important as indicated in Figure 3-53.

Alternately, dn/dt is given by the rate of transfer (k_{tr}) of a molecule from the liquid to the gas phase:

$$(3-15) \quad \frac{dn}{dt} = k_{tr} \cdot c$$

Methanol and ethanol are both polar molecules and are less volatile; their diffusion through the membrane is very slow. Therefore, their mass spectrometric currents are independent of the electrolyte flow rate.

3.12 Literature review

Wang [26] has performed measurements of Fe^{3+} reduction, ^{13}CO oxidation and H_2 oxidation to characterize the dual thin-layer flow through cell through finding the correlation of faradaic current with the flow rate (Figure 3-54). In the electrochemical compartment of the cell, the faradaic current is proportional to u^x with $x=1/3$ for diffusion limited process, as long as the flow rate u is not so small.

There is a close agreement between the literature values and the values obtained in this work. As shown in Figure 3-19, for Fe^{3+} measurement $x=0.34$, for ^{13}CO oxidation $x=0.30$ (Figure 3-47), and for H_2 oxidation $x=0.34$ (Figure 3-19).

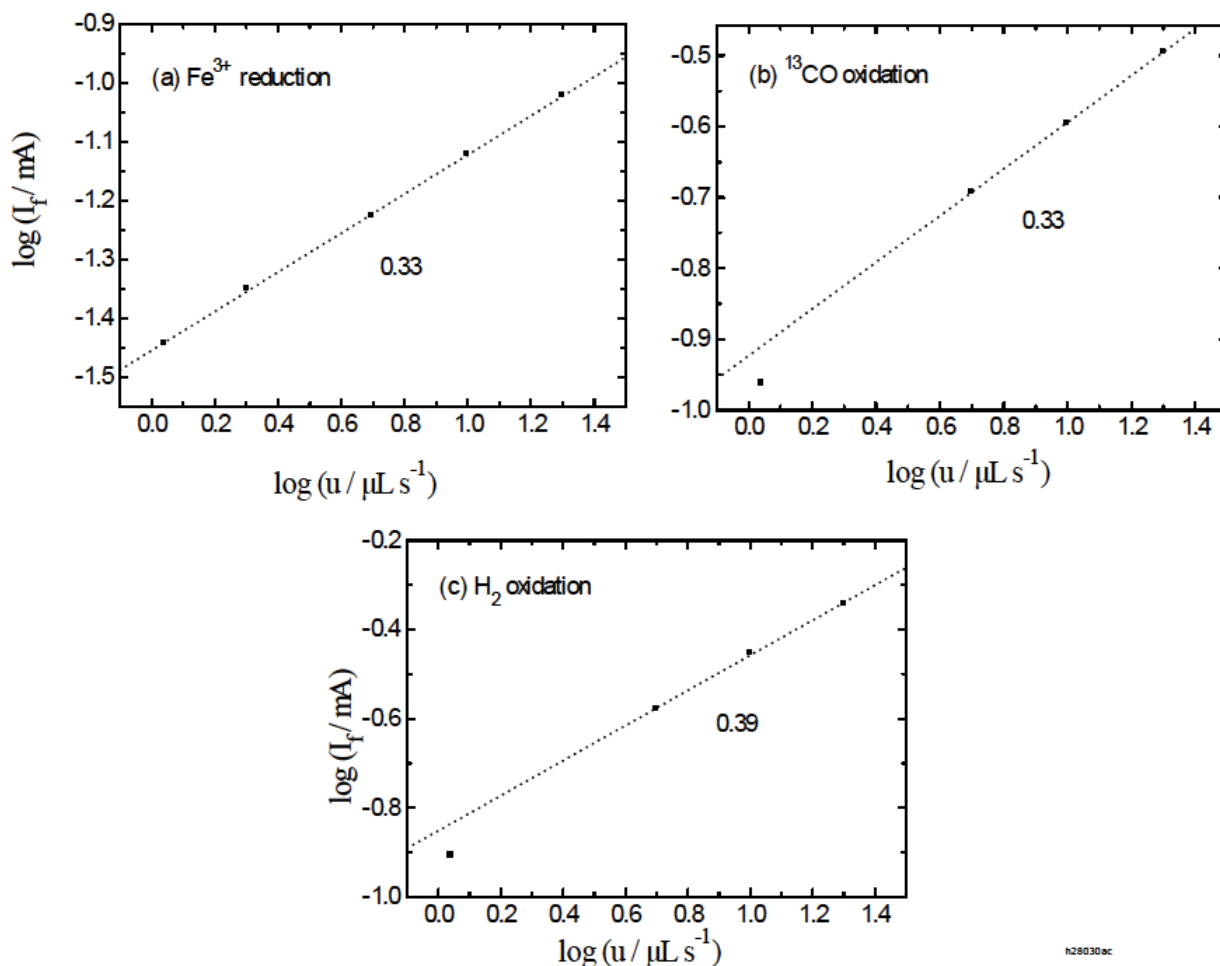


Figure 3-54 Correlation of faradaic current with the flow rate. (a) Fe^{3+} reduction at 0.5V in 0.001M Fe^{3+} + 0.5M H_2SO_4 solution, (b) ^{13}CO oxidation at 1.0V in saturated CO solution with 0.5M H_2SO_4 , (c) H_2 oxidation at 0.3V in saturated H_2 solution with 0.5M H_2SO_4 [26]

Löffler [24] performed mass spectrometric experiments for various substances. Figure 3-55 shows the logarithmic plots of ionic current versus flow rate. From the log-log plot of the ion current versus the flow rate, the exponent of u can be calculated through the obtained slopes. Overall, the gases have the greatest exponents. The values of the exponents for the ether and the ester are lower. The alcohols have the lowest values of the exponent of u (Table 3-1). The value of exponent obtained for Ester differs from the value obtained in this work. As shown in Figure 3-53, the exponent of u for Methylformate is 0.05 while in Löffler's work, it is 0.31. This might be due to decomposition of the Methylformate in our work.

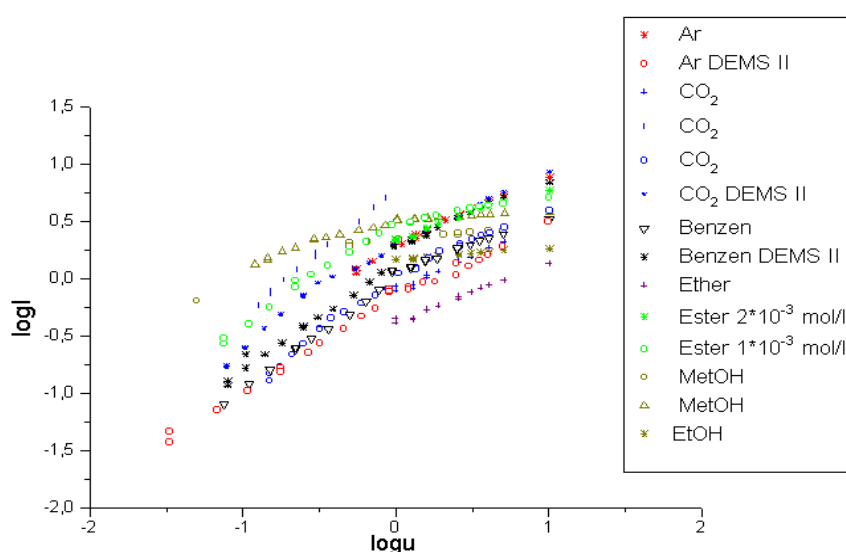


Figure 3-55 Logarithmic plots of the ionic current versus flow rates for various substances [24]

Substance	x for $u < 0.8 \mu\text{l/s}$	x for $u > 0.8 \mu\text{l/s}$
Argon		0.61
Argon DEMS II	0.94	0.65
CO ₂		0.58
CO ₂	1	
CO ₂	1.05 - 0.83	0.55
CO ₂ DEMS II	0.96	0.66
Benzen	1	0.45
Benzen DEMS II	0.95	0.6
Ester ($c = 2 \cdot 10^{-3} \text{ mol/l}$)		0.48 - 0.33
Ester ($c = 1 \cdot 10^{-3} \text{ mol/l}$)	1 - 0.82	0.31
Ether		0.51
Ethanol		0.11
Methanol		0.12
Methanol	0.74 - 0.41	0.09

Table 3-1 values of the exponent of u for various substances at low and high flow rates [24]

Fuhrmann et al. [21, 22] have introduced a numerical method which models the coupled fluid flow and reactant transport. This method is used to interpret the limiting current measurements in the flow cell. As test reaction, H_2 oxidation at overpotential 370 mV on a thin-layer carbon supported Pt catalyst electrode is used. Plot of limiting current in dependence of $u^{1/3}$ for experimental and numerical output is given for different temperatures in Figure 3-56.

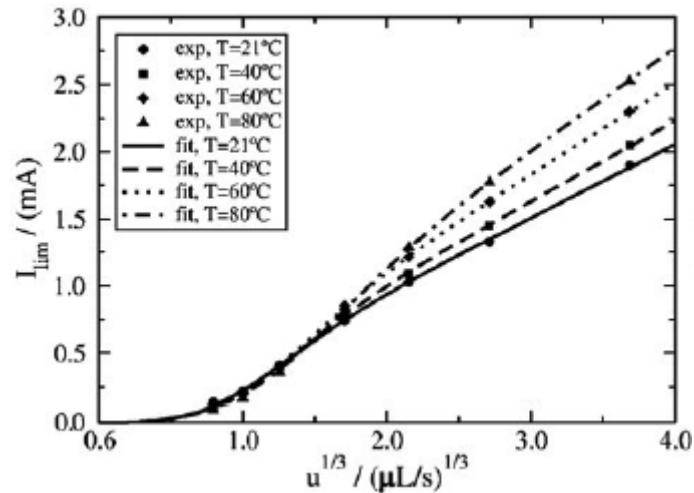


Figure 3-56 Fits of the calculated limiting currents to measured values as a function of flow rate; Individual fit for different temperature curves [22]

In the cylindrical flow cell, two kinds of boundary layer regimes are observed, one somehow similar to a wall jet (close to the inlet), and another one, behaves more channel-like (in the region between inlet and outlet).

In the case of wall-jet, the limiting current is proportional to $u^{3/4}$ and for channel cell this proportionality is $u^{1/3}$.

3.13 Conclusion

In this work, the hydrodynamic electrochemical and mass spectrometric features of the dual thin-layer flow through cell have been characterized. The combination of two working electrodes in this cell is analogous to the rotating ring-disk electrode in voltammetry. The cell represents “laminar flow” behaviour for the studied range of electrolyte flow rate. The faradaic and mass spectrometric currents are proportional to cubic root of electrolyte flow rate in high flow rates (between 2 and 80 $\mu\text{l/s}$) and are in a linear dependency in low flow rates (>2 $\mu\text{l/s}$). The obtained values show a decay of the transfer efficiency and increase of the shielding factor with increasing the electrolyte flow rate. The highest value for collection efficiency happens in the lowest electrolyte flow rate.

For species with low vapor pressure (e.g., methylformate), and polar molecules (e.g., methanol and ethanol), evaporation through the membrane is slow. Therefore, the ionic current is less dependent on the electrolyte flow rate.

Chapter 4

Results and discussion

4 Oxygen solubility and diffusion coefficient

In this chapter, we present a new technique to determine the solubility and diffusivity of oxygen in aqueous and non-aqueous electrolytes by on-line differential electrochemical mass spectrometry (DEMS), using a dual thin-layer flow through cell. The aqueous electrolytes are pure, K^+ -containing, and Li^+ -containing H_2O ; and the non-aqueous electrolytes are pure, Li^+ -containing, and Mg^{2+} -containing Propylene Carbonate (PC), Dimethyl Sulfoxide (DMSO), Tetraglyme (TEGDME), and N-Methyl-2-pyrrolidone (NMP).

The current which can be drawn from the batteries or also fuel cells, is limited by diffusion of the gases reacting through the electrolyte to the electrode surface. On the other hand, following the Fick's law, this limiting current directly depends on the solubility and diffusivity of the gas in the bulk electrolyte.

Some techniques are used to find the solubility and diffusivity of oxygen in aqueous and non-aqueous solutions. For aqueous solutions Gubbins and Walker have used gas chromatography to determine the solubility and diffusion coefficient of oxygen in potassium hydroxide [33]. Zhang et al. also determined the maximum concentration C_{O_2} and the diffusion coefficient D_{O_2} in a wide concentration range of KOH solutions using hydrodynamic chronocoulometry with rotating disk electrodes [34]. Davis et al. have measured the above quantities in aqueous KOH solutions by using the rotating disk electrode through evaluation of limiting current of oxygen [35]. For determination of oxygen solubility in aqueous lithium hydroxide, Elliot et al. have applied radiolytic decomposition of water [36]. For non-aqueous solutions, Achord and Hussey have reported analytical procedure based on gas chromatography to find the solubility of oxygen in propylene carbonate (PC), dimethylsulfoxide (DMSO) and some other non-aqueous electrolytes [37]. Herranz et al. also have studied the solubility and diffusivity of oxygen in PC using rotating ring disk electrode voltammetry (RRDE) [38]. Tsushima et al. have developed hydrodynamic chronocoulometry to determine the maximum concentration

C_{O_2} and the diffusion coefficient D_{O_2} in DMSO [39]. Laoire et al. have reported values for the oxygen diffusion coefficient in Li^+ -containing electrolytes [40].

The problem when using electrochemical methods for the determination of solubility and diffusivity is that the stoichiometry of the electrochemical reaction has to be known and the current efficiencies have to be exactly 100 %. Whereas this may be achieved in aqueous electrolytes, particularly the oxygen reduction in non-aqueous electrolytes is not that well established. Therefore, in this work we use mass spectrometry for the detection of the molecules diffusing towards a surface, which is a porous Teflon membrane.

Data presented in the following studies refer exclusively to the correlation of ionic current detected by differential electrochemical mass spectrometry (DEMS) with flow rate of electrolytes passing through "dual thin-layer flow through cell".

We use the same setup and cell as typically in DEMS, although electrochemistry is not involved in these measurements. In principle, the technique used here therefore is membrane introduction mass spectrometry (MIMS) [41], but with a porous membrane which guarantees short detection times.

4.1 Theoretical aspects

After recognizing the flow condition of the cell in chapter 3 (laminar channel flow; eq. 1-11), the relevant equations will be used for determination of oxygen dissolved in aqueous and non-aqueous electrolytes as they are known as the most important and useful in metal-air batteries. Due to the complex geometry of our cell, the exact dependence on the flow rate is not known a priori. We therefore use a more general expression:

$$(4-1) \quad I_F = g \cdot z \cdot F \cdot c \cdot D^{2/3} \cdot u^x$$

g : the cell constant

x : flow rate proportionality ($x=1/3$; obtained in chapter 3)

Here, in this work, we replace the usual electrochemical detection by the mass spectrometric detection and therefore:

$$(4-2) \quad \frac{dn}{dt} = g \cdot c \cdot D^{2/3} \cdot u^x$$

Or

$$(4-3) \quad I_i = g \cdot K^\circ \cdot c \cdot D^{2/3} \cdot u^x$$

Here, we neglect a possible dependence on the viscosity. A justification is given below.

All these equations hold under the condition that each molecule sitting in contact with the electrode surface or the membrane, immediately reacts or is evaporating into the vacuum of the mass spectrometer (diffusion limitation).

The efficiency f_i is defined as the ratio of the amount of species entering the mass spectrometer ($n_i = I_i/K^\circ$) and the total amount of substance entering the cell ($n_{total} = c \cdot u$).

$$(4-4) \quad f_i = n_i / n_{total}$$

n_i : amount of species detected by mass spectrometer ($n_i = I_i/K^\circ$)

n_{total} : the total amount of substance entering the cell ($n_{total} = c \cdot u$)

The flow dependence of the efficiency is based on the use of general formulas, which is represented by simplified flow rate dependencies of the current. This simplification is necessary because there is no indication that can be made about which flow conditions ("flow channel" or "wall jet" behavior) are present. The considerations will be presented with case studies.

In the case of very low flow rates ($u \rightarrow 0$), the residence time of species in the cell is large enough that each molecule reaches the membrane and passes into the vacuum system. This leads to an efficiency of $f_i = 100\%$; thus, the ion current is linearly dependent on the flow rate:

$$(4-5) \quad f_i = 1 = \frac{I_i / K^\circ}{c \cdot u} \Rightarrow I_i = K^\circ \cdot c \cdot u$$

At high flow rates and therefore short residence times the efficiency is less than 100%; thus, equation 4-3 will be used in this case as the dependence of ion current on flow rate. Later on, the equation 4-5 will be used to determine the value of c ; and equation 4-3, with the experimental found exponent for u ($x=1/3$), will be applied to find the value of D .

4.2 Flow rate dependence of the ionic current

The ion current of oxygen at various flow rates in the range of $0.1\text{--}80\ \mu\text{l}\cdot\text{s}^{-1}$ was detected for different substances. O_2 -saturated aqueous and non-aqueous electrolytes are passed through the dual thin-layer flow through cell, while the mass spectrometric current is recorded for approximately 30 seconds at each flow rate. Figures 4-1 and 4-2 show an example for O_2 saturated pure water.

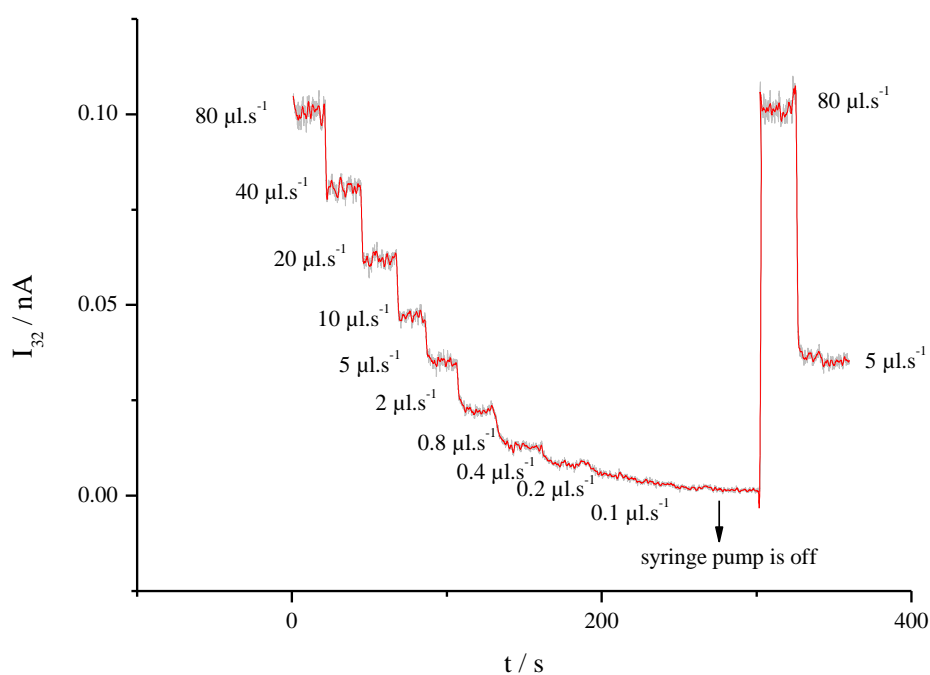


Figure 4-1 The ion current of oxygen ($m/z=32$) at various flow rates ($0.1\text{--}80\ \mu\text{l}\cdot\text{s}^{-1}$) for O_2 -saturated pure H_2O

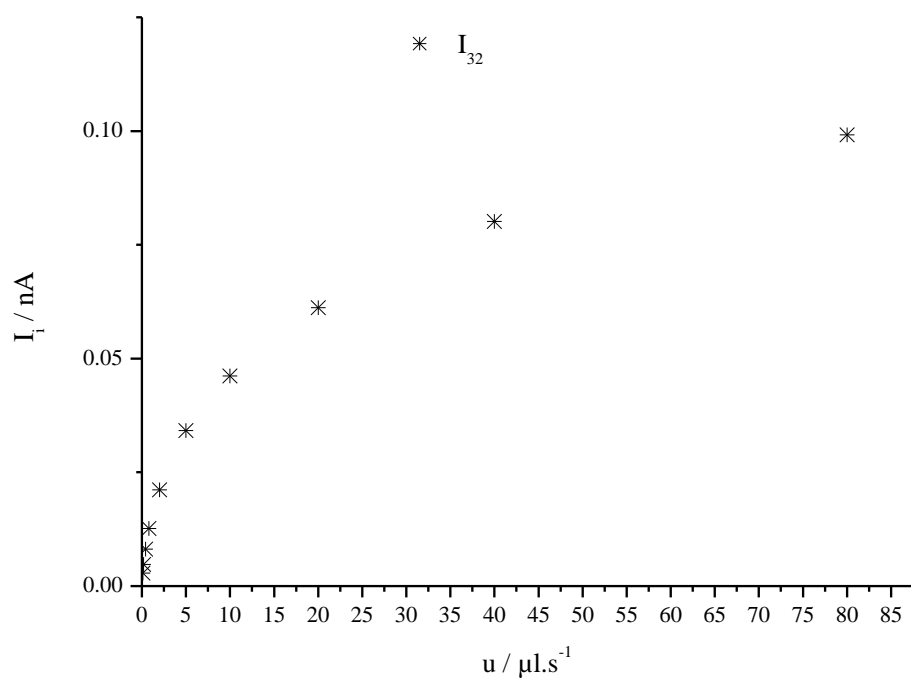


Figure 4-2 Flow rate dependence of ion current ($m/z=32$) at various flow rates ($0.1 - 80 \mu\text{l.s}^{-1}$) for O_2 saturated pure water

Furthermore, the flow rates must be corrected in the case of aqueous electrolytes. A distortion of the flow rates occurs by water evaporation of the aqueous electrolytes through the pores of the hydrophobic Teflon membrane. This correction is only possible for very volatile species and gases, i.e. when evaporation is completely diffusion limited. The correction is obtained by extrapolation of the data in very low flow rates. Subjoining the evaporation flow to the set of flow rates, gives the real flow rates. Figure 4-3 demonstrates an example of extrapolation of data for O₂ saturated pure water to find the evaporation rate. The water evaporation rates for the various O₂ saturated aqueous electrolytes are as following: 0.0526 $\mu\text{l}\cdot\text{s}^{-1}$ for pure water, 0.012 $\mu\text{l}\cdot\text{s}^{-1}$ for 0.1 M LiOH, 0.0496 $\mu\text{l}\cdot\text{s}^{-1}$ for 0.1 M KOH, 0.026 $\mu\text{l}\cdot\text{s}^{-1}$ for 1 M KOH and 0.021 $\mu\text{l}\cdot\text{s}^{-1}$ for 2.5 M KOH.

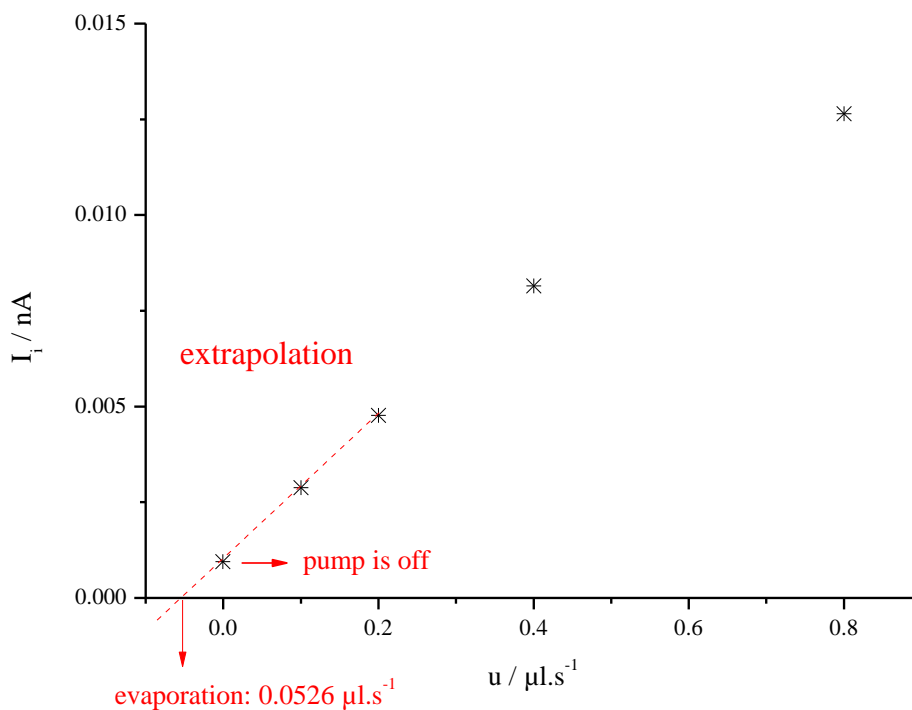


Figure 4-3 Extrapolation of the data in very low flow rates to obtain the corrected flow rate values: O₂ saturated pure water; water evaporation rate: 0.0526 $\mu\text{l}\cdot\text{s}^{-1}$

Figures 4-4 and 4-5 show the corrected flow rate dependence of the normalized ionic currents (I_i/K°) of aqueous and non-aqueous electrolytes, respectively. The ionic currents are divided by K° to normalize and plot the values which only depend on g , c , D and of course u , but not on the state of the mass spectrometer.

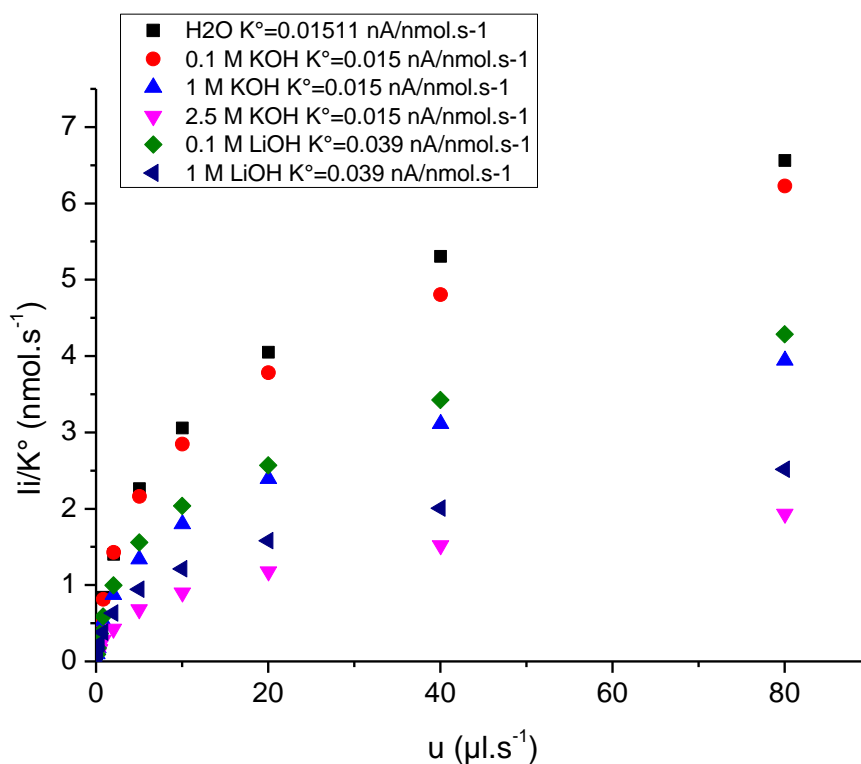


Figure 4-4 Flow rate dependence of normalized ion current ($m/z=32$) for O_2 saturated aqueous electrolytes: pure water; 0.1 M and 1 M LiOH; 0.1 M, 1 M and 2.5 M KOH

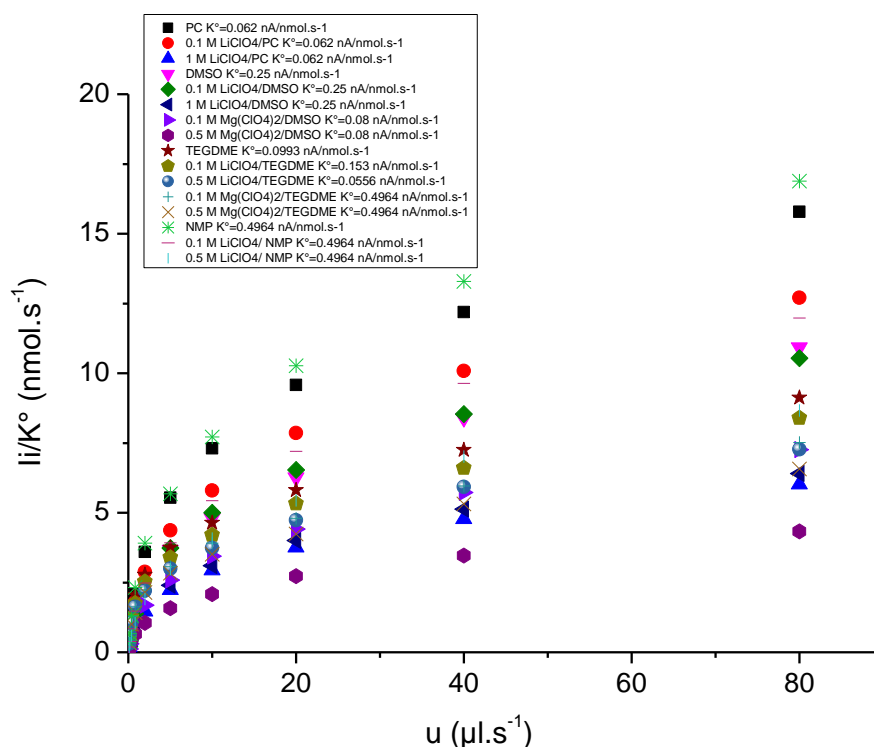


Figure 4-5 Flow rate dependence of normalized ion current ($m/z=32$) for O_2 saturated non-aqueous electrolytes: pure Propylene Carbonate (PC); 0.1 M and 1 M $LiClO_4/PC$; pure Dimethyl sulfoxide (DMSO); 0.1 M and M $LiClO_4/DMSO$; 0.1 M and 0.5 M $Mg(ClO_4)_2/DMSO$; pure Tetraethylene glycol dimethyl ether (TEGDME); 0.1 M and 0.5 M $LiClO_4/TEGDME$; 0.1 M and 0.5 M $Mg(ClO_4)_2/TEGDME$; pure N-Methyl-2-pyrrolidone (NMP); 0.1 M and 0.5 M $LiClO_4/NMP$

As seen in figures 4-2 and 4-3, the ionic current recorded for oxygen ($m/z=32$) dissolved in both aqueous and non-aqueous electrolytes decreases with increasing the concentration of salt. In other words, the recorded ionic current for oxygen in pure solvents such as H_2O , PC, DMSO, TEGDME, and NMP is higher than the values for salt containing electrolytes.

The dependence of the ionic current of oxygen on flow rate can be obtained by creating log-log plots. Figures 4-6, 4-7 and 4-8 show this proportionality in both aqueous and non-aqueous electrolytes, respectively. For low flow rates the slope equals to 1, and for high flow rates the slope is about 0.33.

With these values of proportionality, equation 4-5 would be confirmed again for low flow rates, and the value of 0.33 will be used in equation 4-3 for the exponent of u ($x=0.33$).

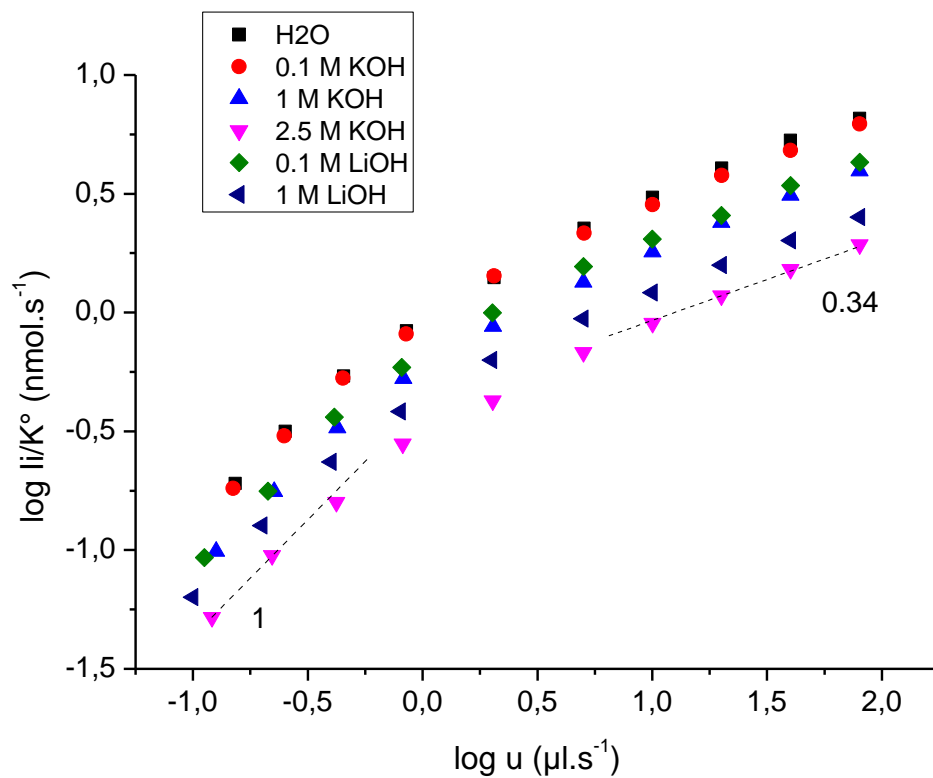


Figure 4-6 Log-log plot of the ion current ($m/z=32$) vs. flow rates for aqueous electrolytes: pure water; 0.1 M and 1 M LiOH; 0.1 M, 1 M and 2.5 M KOH

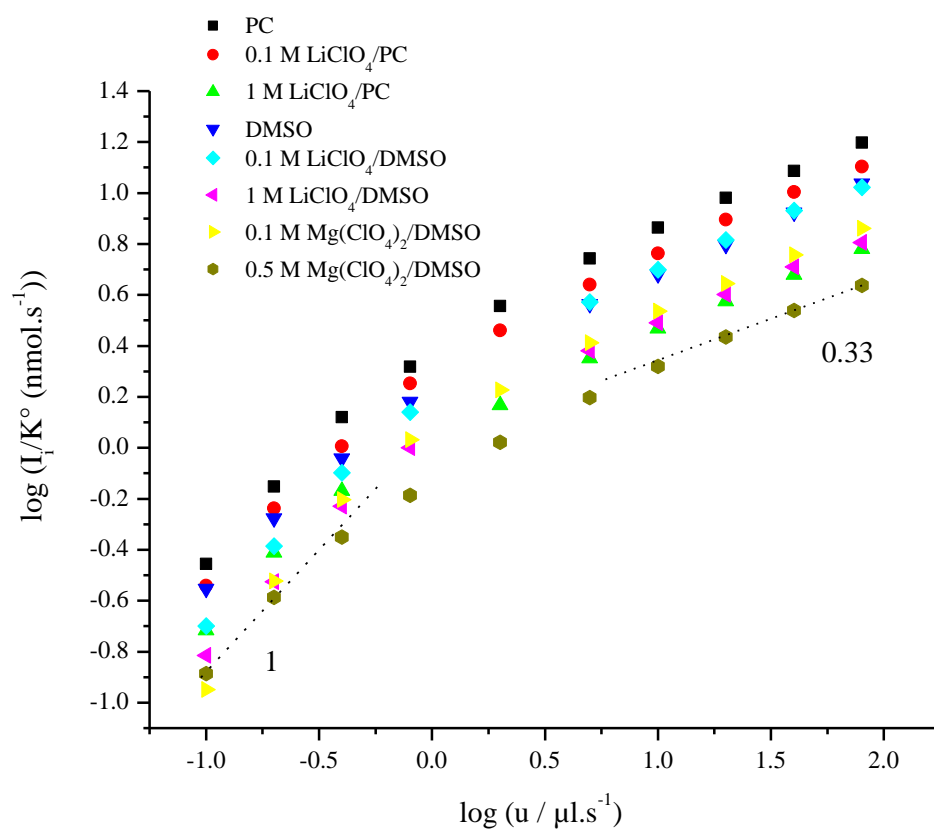


Figure 4-7 Log-log plot of the ion current ($m/z=32$) vs. flow rates for non-aqueous electrolytes: pure Propylene Carbonate (PC); 0.1 M and 1 M LiClO₄/PC; pure Dimethyl sulfoxide (DMSO); 0.1 M and 1 M LiClO₄/DMSO; 0.1 M and 0.5 M Mg(ClO₄)₂/DMSO

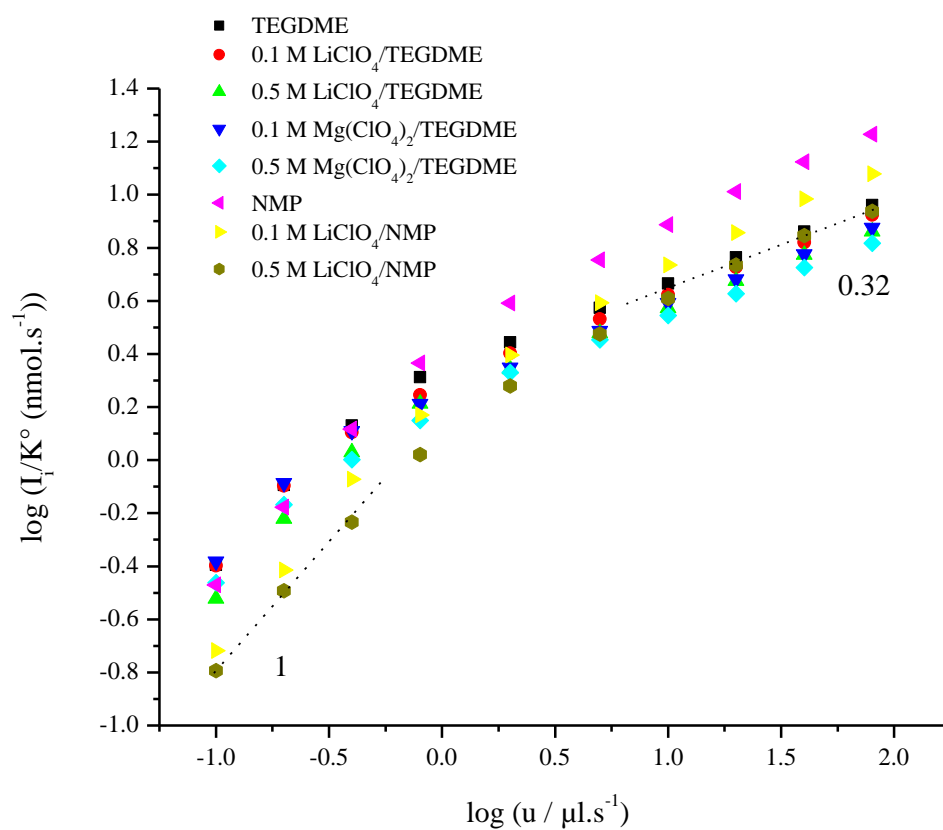


Figure 4-8 Log-log plot of the ion current ($m/z=32$) vs. flow rates for non-aqueous electrolytes: pure Tetraethylene glycol dimethyl ether (TEGDME); 0.1 M and 0.5 M LiClO₄/TEGDME; 0.1 M and 0.5 M Mg(ClO₄)₂/TEGDME; pure N-Methyl-2-pyrrolidone (NMP); 0.1 M and 0.5 M LiClO₄/NMP

4.3 O₂ solubility and diffusion coefficient in aqueous and non-aqueous electrolytes

With the value of 1 for the exponent of u at very low flow rate, the solubility of oxygen (c) can be calculated via equation 4-5 based on the slopes achieved by plotting the ionic current versus flow rate for both the aqueous and non-aqueous electrolytes with different concentrations of salts at low flow rates of electrolytes (Figures 4-9 and 4-10). The c values decrease with increasing the salt concentration of the electrolytes.

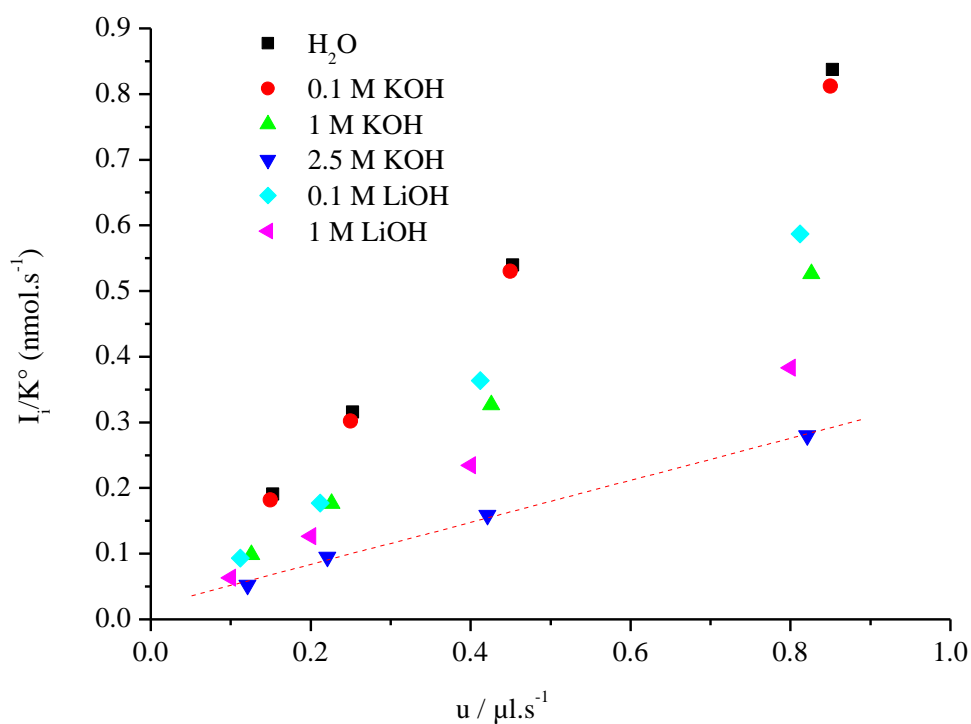


Figure 4-9 Flow rate dependence of normalized ion current ($m/z=32$) at low flow rates for aqueous electrolytes: pure water; 0.1 M and 1 M LiOH; 0.1 M, 1 M and 2.5 M KOH

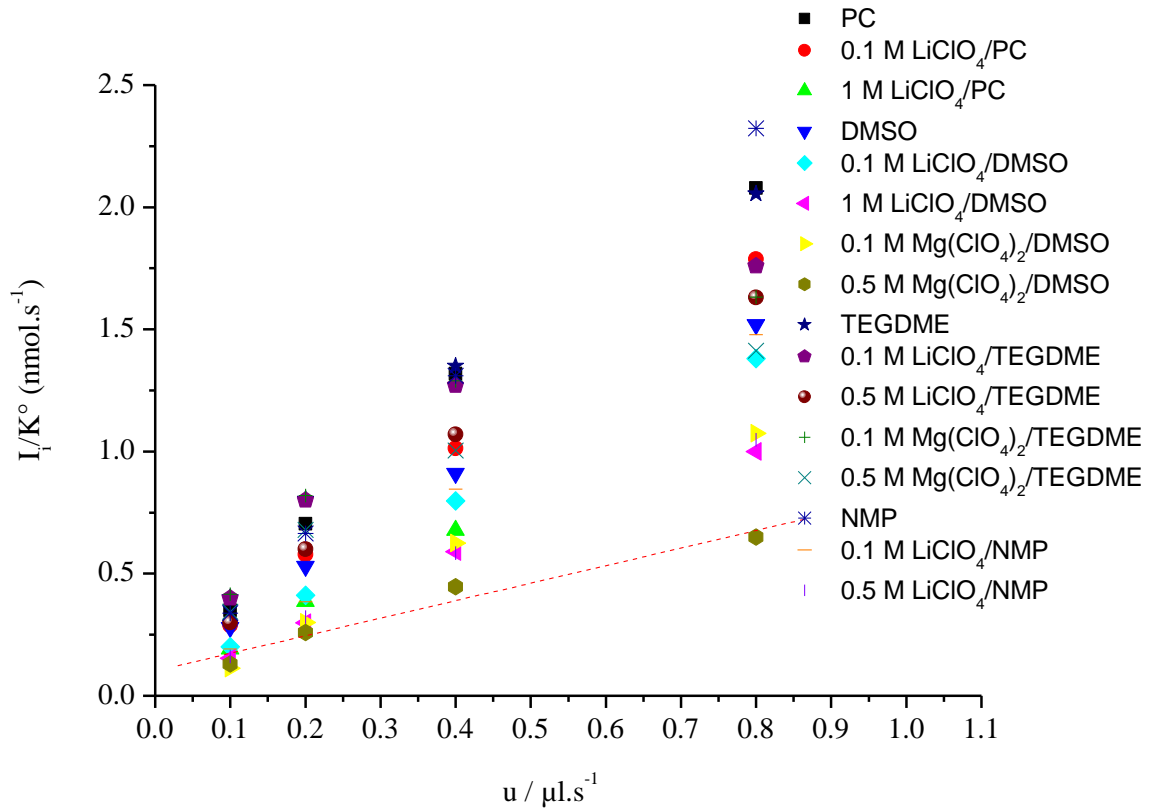


Figure 4-10 Flow rate dependence of normalized ion current ($m/z=32$) at low flow rates for non-aqueous electrolytes: pure Propylene Carbonate (PC); 0.1 M and 1 M LiClO_4/PC ; pure Dimethyl sulfoxide (DMSO); 0.1 M and 1 M $\text{LiClO}_4/\text{DMSO}$; 0.1 M and 0.5 M $\text{Mg}(\text{ClO}_4)_2/\text{DMSO}$; pure Tetraethylene glycol dimethyl ether (TEGDME); 0.1 M and 0.5 M $\text{LiClO}_4/\text{TEGDME}$; 0.1 M and 0.5 M $\text{Mg}(\text{ClO}_4)_2/\text{TEGDME}$; pure N-Methyl-2-pyrrolidone (NMP); 0.1 M and 0.5 M $\text{LiClO}_4/\text{NMP}$

On the other hand, with the value of 0.33 for the exponent of u for high flow rates, the behavior is similar to that of "flow channel". This also justifies neglecting the viscosity (cf. eq. 1-11). In this case, equation 4-6 can be considered through equation 4-3 with $x=1/3$:

$$(4-6) \quad I_i = g \cdot K^o \cdot c \cdot D^{2/3} \cdot u^{1/3}$$

g represents the proportionality factor and also contains all the geometric factors of the cell. The geometry factor of the cell is obtained from a measurement in an aqueous solution of oxygen in pure water (with well-known oxygen solubility and diffusivity).

Figures 4-11 and 4-12 show the normalized ionic current versus $u^{1/3}$ at high flow rates for aqueous and non-aqueous electrolytes.

The slope of ionic current vs. $u^{1/3}$ for pure water (Figure 4-11; black square data), beside the known common values of oxygen concentration and diffusion coefficient in literature [33], are used in equation 4-6 for calculation of g . With three independent measurements, the values of $16.2 \text{ cm}^{2/3}$, $17.05 \text{ cm}^{2/3}$ and $14.2 \text{ cm}^{2/3}$ are obtained for geometry factor (g) which will be used subsequently in calculations of diffusivity of oxygen in all aqueous and non-aqueous electrolytes, measured through the same dual thin-layer through cell construction and same number of spacers. The value of $16.2 \text{ cm}^{2/3}$ is used for g in all measurements. Two Teflon spacers (purchased from Gortex) are used in this work. Each spacer has an inner diameter of 6 mm and a thickness of $65 \text{ }\mu\text{m}$.

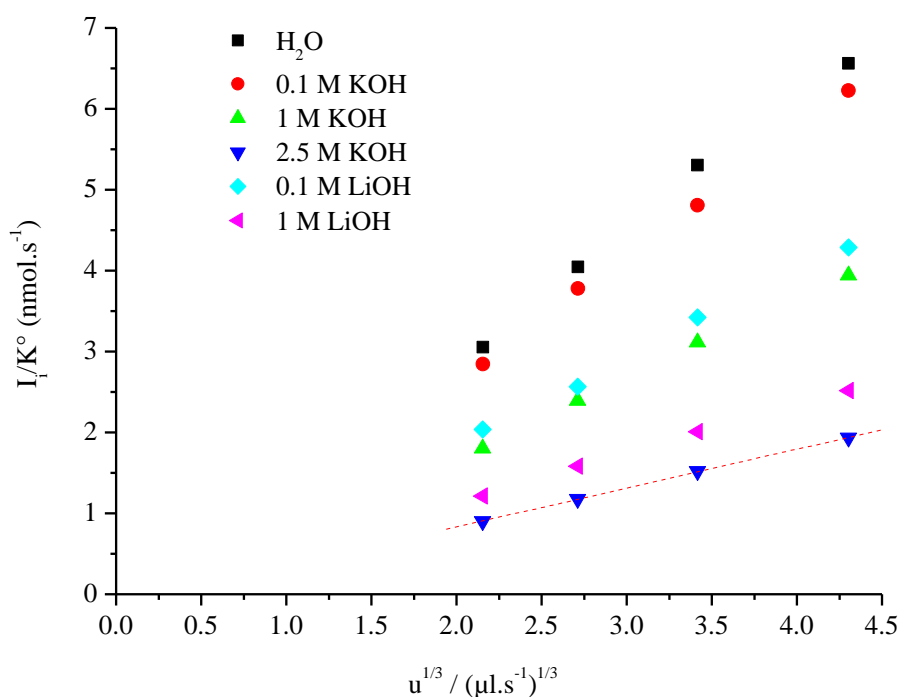


Figure 4-11 Ionic current I_i ($m/z=32$) vs. flow rate $u^{1/3}$ at high flow rates for aqueous electrolytes: pure water; 0.1 M and 1 M LiOH; 0.1 M, 1 M and 2.5 M KOH

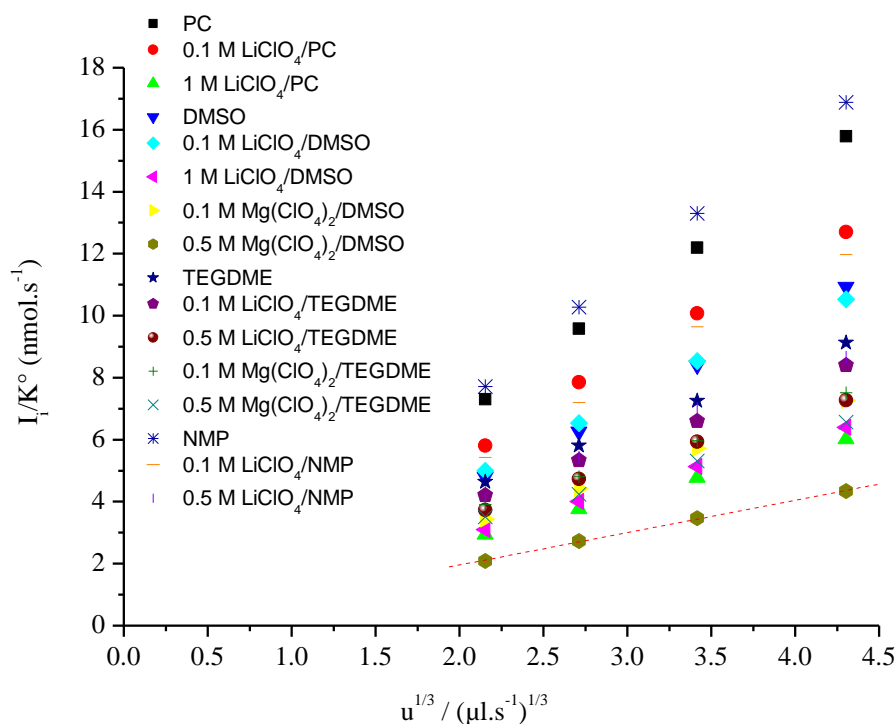


Figure 4-12 Ionic current I_i ($m/z=32$) vs. flow rate $u^{1/3}$ at high flow rates for non-aqueous electrolytes: pure Propylene Carbonate (PC); 0.1 M and 1 M LiClO_4/PC ; pure Dimethyl sulfoxide (DMSO); 0.1 M and 1 M $\text{LiClO}_4/\text{DMSO}$; 0.1 M and 0.5 M $\text{Mg}(\text{ClO}_4)_2/\text{DMSO}$; pure Tetraethylene glycol dimethyl ether (TEGDME); 0.1 M and 0.5 M $\text{LiClO}_4/\text{TEGDME}$; 0.1 M and 0.5 M $\text{Mg}(\text{ClO}_4)_2/\text{TEGDME}$; pure N-Methyl-2-pyrrolidone (NMP); 0.1 M and 0.5 M $\text{LiClO}_4/\text{NMP}$

Based on experimentally determined geometry g and the slopes obtained by plotting the ionic current ($m/z=32$) versus $u^{1/3}$ (Figures 4-11 and 4-12), the values of diffusivity of oxygen in aqueous and non-aqueous solutions with different concentrations of various salts are easily calculated by using equation 4-6. D values obtained for pure solvents of H_2O , PC, DMSO, TEGDME, and NMP are higher than salt-containing electrolytes and they decrease with increasing the concentration of salts.

Table 4-1 shows the values calculated for solubility and diffusivity of oxygen in different electrolytes compared with the literature data.

The saturation concentration (1.25 mM) obtained for H_2O solution is in fair agreement with those (1.15-1.26 mM) often cited in literature using gas chromatography technique [33, 35, 36, 42]. The values for PC (3.53 mM), DMSO (2.5 mM), TEGDME (4.03 mM), and NMP (3.26 mM) solvents are close to the literature values obtained by gas chromatography [37, 43-

46]. No D value is found in literature for pure non-aqueous solvents. The D value obtained in this work for PC ($19.4 \times 10^{-6} \text{ cm}^2 \cdot \text{s}^{-1}$) is in the range ($25 \pm 8 \times 10^{-6} \text{ cm}^2 \cdot \text{s}^{-1}$) reported in literature using rotating ring disk electrode voltammetry [38] for 0.2 M TBATFSI/PC. The value obtained for DMSO ($17.5 \times 10^{-6} \text{ cm}^2 \cdot \text{s}^{-1}$) is in the range of values reported in literature obtained by hydrodynamic chronocoulometry for salt-containing electrolytes [39, 40], but those in TEGDME ($5.29 \times 10^{-6} \text{ cm}^2 \cdot \text{s}^{-1}$) and NMP ($21.1 \times 10^{-6} \text{ cm}^2 \cdot \text{s}^{-1}$) are different from the previously reported values [40, 46].

Table 4-1 Solubility and diffusivity of oxygen in aqueous and non-aqueous electrolytes at $25 \pm 2^\circ\text{C}$ and 1 atm. The numbers in the brackets are the numbers of the references from which the values are taken

Electrolyte	Value obtained in this work ($25 \pm 2^\circ\text{C}$ / 1 atm)		Literature values (25°C / 1 atm)	
	c/mM	10^6 D/cm 2 .s $^{-1}$	c/mM	10^6 D/cm 2 .s $^{-1}$
H ₂ O	1.25	Lit. value of 19 used for g determination	1.25 [33] 1.26 [35, 36, 42] 1.15 [36]	19 [33, 47] 21.2 [48]
0.1 M KOH	1.2	18.2	1.23 [33] 1.20 [35] 1.03±0.12 [34]	18.3 [33] 19 [35] 19.5±0.40 [34]
1 M KOH	0.78	16.75	0.81 [33] 0.80 [35] 0.82±0.10 [34]	16.1 [33] 14.5 [35] 14.4±0.30 [34]
2.5 M KOH	0.43	16	0.44 [33] 0.42 [35] 0.45±0.02 [34]	12.7 [33] 10.7 [35] 12.5±0.01 [34]
0.1 M LiOH	0.84	19	-	-
1 M LiOH	0.63	13.3	0.73 (1.1 M LiOH) [36]	-
PC	3.53	19.4	3.6±0.2 [37] 3.2 [43] 4.8 (0.2 M TBATFSI/PC) [38]	25±8 (0.2 M TBATFSI/PC) [38]
0.1 M LiClO ₄ /PC	2.9	16.2	-	-
1 M LiClO ₄ /PC	1.95	9.6	-	-
DMSO	2.5	17.5	2.1±1 [37] 2.1 [44]	-
0.1 M LiClO ₄ /DMSO	2.04	17	2.24 (0.1 M TEAP/DMSO) [39] 2.1 (0.1 M TEAP/DMSO) [49]	16.7 (0.1 M LiPF ₆ /DMSO) [40] 9.75 (0.1 M TBAPF6/DMSO) [40] 20.8±0.27 (0.1 M TEAP/DMSO) [39]

1 M LiClO ₄ /DMSO	1.6	13.3	-	-
0.1 M Mg(ClO ₄) ₂ /DMSO	1.8	14	-	-
0.5 M Mg(ClO ₄) ₂ /DMSO	1.3	10.6	-	-
<hr/>				
TEGDME	4.03	5.8	4.3 [45]	-
			4.37 [43]	
0.1 M LiClO ₄ /TEGDME	3.99	5.29	-	2.17 (0.1 M LiPF ₆ /TEGDME) [40]
0.5 M LiClO ₄ /TEGDME	2.97	5.04	-	-
0.1 M Mg(ClO ₄) ₂ /TEGDME	4.05	4.48	-	-
0.5 M Mg(ClO ₄) ₂ /TEGDME	3.34	4.34	-	-
<hr/>				
NMP	3.26	21.1	3.2 [46]	-
0.1 M LiClO ₄ /NMP	2.2	20	-	10.9 (0.1 M TBAClO ₄ /NMP) [46]
0.5 M LiClO ₄ /NMP	1.6	19.1	-	-

As seen in table 4-1, for the same cation concentration, the oxygen solubility in K⁺-containing electrolyte is larger than in Li⁺-containing electrolyte. The origin is larger solvation shell around Li⁺. Similar effect exists while comparing O₂ solubility in Li⁺-containing and Mg⁺-containing DMSO: larger solvation shell around Mg⁺ leads to smaller amount of O₂ solubility in Mg⁺-containing DMSO.

4.4 Conclusion

In this chapter, "flow channel" behavior is again confirmed for the cell where the ionic current of dissolved oxygen ($m/z=32$) is proportional to u in low flow rates of electrolyte and $u^{1/3}$ for high flow rates, and shows that the Levich equation developed by Matsuda [19] is eligible for calculation of diffusion coefficient of oxygen. The values obtained with this technique compared with the values previously reported in literature performed by other techniques, represents applicability of dual thin-layer cell bonded to DEMS for determination of oxygen solubility and diffusivity. The accuracy of this method appears to be quite good as can be seen by comparison of the results obtained in the present work with literature data where available. Both values of solubility and diffusion coefficient decrease with increasing the concentration of salt in the electrolyte due to "salting out" effect.

Chapter 5

5 Summary / Conclusion

In this work, the hydrodynamic electrochemical and mass spectrometric features of the dual thin-layer flow through cell have been characterized. The cell represents “laminar flow” behaviour for the studied range of electrolyte flow rate. The faradaic and mass spectrometric currents are proportional to cubic root of electrolyte flow rate in high flow rates (between 2 and 80 $\mu\text{l/s}$) and are in a linear dependency in low flow rates ($>2 \mu\text{l/s}$). The obtained values show an exponential-like decay of the transfer efficiency and parabolic-like increase of the shielding factor with increasing the electrolyte flow rate for Fe^{3+} , Hydroquinone, dissolved H_2 , and ^{13}CO bulk solutions. The highest value for collection efficiency occurs for the lowest electrolyte flow rate.

These results were the basis of a new technique which is presented here to determine the solubility and diffusivity of oxygen in aqueous and non-aqueous electrolytes by on-line differential electrochemical mass spectrometry (DEMS), using the same dual thin-layer flow through cell. The aqueous electrolytes are pure, K^+ -containing, and Li^+ -containing H_2O ; and the non-aqueous electrolytes are pure, Li^+ -containing, and Mg^{2+} -containing Propylene Carbonate (PC), Dimethyl Sulfoxide (DMSO), Tetraglyme (TEGDME), and N-Methyl-2-pyrrolidone (NMP).

In this chapter, “flow channel” behavior is again confirmed for the cell where the ionic current of dissolved oxygen ($m/z=32$) is proportional to u in low flow rates of electrolyte and $u^{1/3}$ for high flow rates, and shows that the Levich equation developed by Matsuda [19] is eligible for calculation of diffusion coefficient of oxygen. The values obtained with this technique compared with the values previously reported in literature performed by other techniques, represents applicability of dual thin-layer cell bonded to DEMS for determination of oxygen solubility and diffusivity. The accuracy of this method appears to be quite good as can be seen by comparison of the results obtained in the present work with literature data where available. Both values of solubility and diffusion coefficient decrease with increasing the concentration of salt in the electrolyte due to “salting out” effect.

References

1. Rohstoffe, B.f.G.u., *Reserven, Ressourcen und Verfügbarkeit von Energie Rohstoffen*. 2004.
2. **Bundesgesetzblatt, 2002. Bonn(Teil II Nr. 16): p. 966.**
3. Umweltbundesamt, *Nationale Trendtabellen für die deutsche Berichterstattung atmosphärischer Emissionen CO₂ 1990 - 2004*. 2004.
4. BMBF, *Bundesbericht Forschung*. 2006.
5. Carrette, L., K.A. Friedrich, and U. Stimming, *Fuel Cells - Fundamentals and Applications*. Fuel Cells, 2001. **1**(1): p. 5-39.
6. Kinoshita, K., *Analysis of power and energy for fuel cell systems*. Journal of power sources, 1993. **47**: p. 159-175.
7. Carrette, L., et al., *Fuel Cells, an overview*. Bunsen-Magazin, 2000. **2**: p. 27-3.
8. Straßer, K., *PEM-Fuel Cells: State of the art and development possibilities*. Ber. Bunsenges. Phys. Chem., 1990. **94**: p. 1000-1005.
9. Zhang, J., *PEM Fuel Cell Electrocatalysts and Catalyst Layers: Fundamentals and Applications*. 2008, London: Springer.
10. Carrette, L., K.A. Friedrich, and U. Stimming, *Fuel cells: Principles, types, fuels and applications*. ChemPhysChem, 2000. **1**(4): p. 162-193.
11. Girishkumar, G., et al., *Lithium-Air Battery: Promise and Challenges*. The Journal of Physical Chemistry Letters, 2010. **1**(14): p. 2193-2203.
12. Scrosati, B. and J. Garche, *Lithium batteries: Status, prospects and future*. Journal of Power Sources, 2010. **195**(9): p. 2419-2430.
13. Yuasa, M., et al., *Bi-Functional Oxygen Electrodes Using LaMnO₃/LaNiO₃ for Rechargeable Metal-Air Batteries*. Journal of The Electrochemical Society, 2011. **158**(5): p. A605-A610.
14. Wolter, O. and J. Heitbaum, *Differential Electrochemical Mass Spectroscopy (DEMS) - a new method for the study of electrode processes*. Ber. Bunsenges. Phys. Chem., 1984. **88**: p. 2-6.
15. Hartung, T. and H. Baltruschat, *Differential Electrochemical Mass Spectrometry using smooth electrodes: Adsorption and H/D-exchange reactions of benzene on Pt*. Langmuir, 1990. **6**(No.5): p. 953-957.
16. Jusys, Z., H. Massong, and H. Baltruschat, *A New Approach for Simultaneous DEMS and EQCM: Electro-oxidation of Adsorbed CO on Pt and Pt-Ru*. Journal of the Electrochemical Society, 1999. **146**: p. 1093.
17. Matsuda, H., *Zur Theorie der stationären Strom-Spannungskurven von Redoxelektrodenreaktionen in hydrodynamischer Voltammetrie. II. Laminare Rohr- und Kanalströmungen*. Journal of Electroanalytical Chemistry, 1967. **15**: p. 325-336.
18. Brett, C.M.A. and A.M.O. Brett, *Electrochemistry: Principles, Methods and Applications*. 1993, Oxford: Oxford University Press.
19. Levich, B.G., *Physicochemical Hydrodynamics*. 1962, Englewood Cliffs, N.J., USA: Prentice-Hall, Inc.
20. Yamada, J. and H. Matsuda, *Limiting Diffusions Currents in Hydrodynamic Voltammetry*. Journal of Electroanalytical Chemistry, 1973. **44**: p. 189-198.
21. Fuhrmann, J., et al., *Numerical calculation of the limiting current for a cylindrical thin layer flow cell* Electrochimica Acta, 2009. **55**: p. 430-438.
22. Fuhrmann, J., et al., *Experimental and numerical model study of the limiting current in a channel flow cell with a circular electrode*. Physical Chemistry Chemical Physics, 2008. **10**(25): p. 3784-3795.
23. Löffler, T., 2003.

24. Löffler, T., *Charakterisierung und Anwendung einer neuen Dünnschichtzelle für die elektrochemische Massenspektrometrie*, in *Institut für Physikalische und Theoretische Chemie* 1997, Universität Bonn: Bonn. p. 93.
25. Müller, U., *DEMS-Studie zum elektrochemischen Reaktionsverhalten ungesättigter Kohlenwasserstoffe an Platin-Einkristalloberflächen sowie an polykristallinen Platin- und Palladium-Elektroden*, in *Institut für Physikalische Chemie* 1996, Witten-Herdecke: Witten-Herdecke. p. 144.
26. Wang, H., *Electrocatalytic oxidation of adsorbed CO and methanol on Mo, Ru and Sn modified polycrystalline and mono-crystalline platinum electrodes: A quantitative DEMS study*, 2001, Beijing Normal University: Beijing.
27. Bard, A. and L. Faulkner, *Electrochemical Methods: Fundamentals and Applications*. 1980, New York: John Wiley & Sons.
28. Baltruschat, H., *Differential Electrochemical Mass Spectrometry*. Journal of the American Society for Mass Spectrometry, 2004. **15**: p. 1693-1706.
29. Tegtmeier, U., *Diplomarbeit*, 1986, Witten-Herdecke.
30. Baltruschat, H., *Differential Electrochemical Mass Spectrometry as a Tool for Interfacial Studies*, in *Interfacial Electrochemistry*, A. Wieckowski, Editor. 1999, Marcel Dekker, Inc.: New York, Basel. p. 577 - 597.
31. Kokkinidis, G., *Underpotential deposition and electrocatalysis*. Journal of Electroanalytical Chemistry, 1986. **201**: p. 217-236.
32. Kokkinidis, G. and G. Papanastasiou, *Some specific features of the catalytic role of UPD foreign metal adatoms and water on the anodic oxidation of absolute methanol on Pt*. Journal of Electroanalytical Chemistry, 1987. **221**: p. 175-186.
33. Gubbins, K.E. and J.R.D. Walker, *The Solubility and Diffusivity of Oxygen in Electrolytic Solutions*. Journal of The Electrochemical Society, 1965. **112**(5): p. 469-471.
34. Zhang, D., et al., *Hydrodynamic chronocoulometric estimation of diffusion coefficients and saturated concentrations of dioxygen in KOH solutions*. Indian Journal of Chemistry Section a-Inorganic Bio-Inorganic Physical Theoretical & Analytical Chemistry, 2003. **42**(4): p. 801-806.
35. Davis, R.E., G.L. Horvath, and C.W. Tobias, *Solubility and Diffusion Coefficient of Oxygen in Potassium Hydroxide Solutions*. Electrochimica Acta, 1967. **12**(3): p. 287.
36. Elliot, A.J., M.P. Chenier, and D.C. Ouellette, *Solubilities of hydrogen and oxygen in concentrated lithium salt solutions* Fusion Engineering and Design, 1990. **13**(1): p. 29-31.
37. Achord, J.M. and C.L. Hussey, *DETERMINATION OF DISSOLVED-OXYGEN IN NON-AQUEOUS ELECTROCHEMICAL SOLVENTS*. Analytical Chemistry, 1980. **52**(3): p. 601-602.
38. Herranz, J., A. Garsuch, and H.A. Gasteiger, *Using Rotating Ring Disc Electrode Voltammetry to Quantify the Superoxide Radical Stability of Aprotic Li-Air Battery Electrolytes*. Journal of Physical Chemistry C, 2012. **116**(36): p. 19084-19094.
39. Tsushima, M., K. Tokuda, and T. Ohsaka, *Use of Hydrodynamic Chronocoulometry for Simultaneous Determination of Diffusion Coefficients and Concentrations of Dioxygen in Various Media*. Analytical Chemistry, 1994. **66**(24): p. 4551-4556.
40. Laoire, C.O., et al., *Influence of Nonaqueous Solvents on the Electrochemistry of Oxygen in the Rechargeable Lithium-Air Battery*. Journal of Physical Chemistry C, 2010. **114**(19): p. 9178-9186.
41. Kotiaho, T., et al., *Membrane Introduction Mass Spectrometry*. Analytical Chemistry, 1991. **63**(18): p. 875 A - 883 A.
42. Douglas, E., *Solubilities of Oxygen, Argon, and Nitrogen in Distilled Water*. Journal of Physical Chemistry, 1964. **68**(1): p. 169-174.

43. Read, J., et al., *Oxygen transport properties of organic electrolytes and performance of lithium/oxygen battery*. Journal of the Electrochemical Society, 2003. **150**(10): p. A1351-A1356.
44. Johnson, E.L., K.H. Pool, and R.E. Hamm, *POLAROGRAPHIC REDUCTION OF OXYGEN IN DIMETHYLSULFOXIDE*. Analytical Chemistry, 1966. **38**(2): p. 183-&.
45. Hartmann, P., et al., *Pressure Dynamics in Metal-Oxygen (Metal-Air) Batteries: A Case Study on Sodium Superoxide Cells*. The Journal of Physical Chemistry C, 2014. **118**(3): p. 1461-1471.
46. Wang, H., et al., *N-methyl-2-pyrrolidone as a solvent for the non-aqueous electrolyte of rechargeable Li-air batteries*. Journal of Power Sources, 2012. **219**: p. 263-271.
47. Kreuzer, F., *ÜBER DIE DIFFUSION VON SAUERSTOFF IN SERUMEIWEISSLÖSUNGEN VERSCHIEDENER KONZENTRATION*. Helvetica Physiologica Et Pharmacologica Acta, 1950. **8**(4): p. 505-516.
48. Jordan, J., E. Ackerman, and R.L. Berger, *Polarographic Diffusion Coefficients of Oxygen Defined by Activity Gradients in Viscous Media*. Journal of the American Chemical Society, 1956. **78**(13): p. 2979-2983.
49. Sawyer, D.T., et al., *Effects of Media and Electrode Materials on the Electrochemical Reduction of Dioxygen*. Analytical Chemistry, 1982. **54**(11): p. 1720-1724.

Acknowledgment

The work presented here results from collaboration and support of many people. First of all, I would like to thank my thesis supervisor Prof. Dr. Helmut Baltruschat for having accepted me as a PhD student in his group, and for introducing me to the fascinating field of electrochemistry. His continuous support, encouragement, and suggestions have helped me a lot in my work. I truly appreciate all the discussions that often opened my eyes and directed my research.

Thanks to all the members of the jury: Prof. Dr. Thomas Bredow, Prof. Dr. Werner Mader, and Prof. Dr. Karl Maier for reading and evaluating my thesis as well as assisting in my exam. My special thanks go to my friends, colleagues and students, who assisted, advised and supported my research and writing efforts over the past years: Dr. Ernst, Nicky, Ehab, Shahid, Hatem, Nikolay, Ana, Sevda, Christoph M., Christoph B., Jan, Elke, Zan, Philip, Martina, Claudia, Volker, and Akos.

The help of Mrs. Rossignol, Mr. Hintzen and Mrs. Kleine are gratefully appreciated.

Especially, I need to express my gratitude and deep appreciation to Abd El Aziz whose friendship, hospitality, knowledge and wisdom has supported, enlightened and entertained me over the years of our friendship.

Thanks are also given to the members of fine mechanics, electronics and glass blowing workshops, namely Mr. Böhmer, Mr. Königshoven, Mr. Langen as well as Mr. Paulig, for their friendly and professional support during the repair of our measurement devices and in planning and constructing of new elements.

Heartly and special thanks to my family for never ending support. Words cannot express how grateful I am to my mother and father for all of the sacrifices that you've made on my behalf. Your prayer for me was what sustained me thus far.

I would also like to thank to DAAD – Deutscher Akademischer Austauschdienst for their financial support granted through doctoral scholarship: special thanks to Mrs. Pietsch, Mrs. Hosseini-Razi, and Mrs. Seeler.

I also thank Ministry of Science, Research and Technology of Iran to give the permission to continue my studies for PhD abroad. I never forget the help of Mr. Ghasemi and Mr. Padashi.

